Synthesis and characterization of multiferroic BiFeO₃ (BFO) and BFO-based heterostructures for photocatalysis application

A Thesis submitted to

University of Hyderabad

In partial fulfilment of the award of the degree of

DOCTOR OF PHILOSOPHY IN PHYSICS

BY

BANOTH PRAVALLIKA

[Reg. No.: 18PHPH17]



Under the Supervision of

Research Guide

Dr. PRATAP KOLLU

School of Physics

University of Hyderabad

Hyderabad, 500046

Telangana, India

August, 2022





DECLARATION

I, Banoth Pravallika, hereby declare that this entitled "Synthesis and Characterization of multiferroic BiFeO₃ (BFO) and BFO based heterostructures for photocatalysis application" submitted in partial fulfilment of the requirement for the award of Doctor of Philosophy in Physics contains the original research work carried out by me in the School of Physics, University of Hyderabad, Hyderabad, India under the supervision of Dr. Pratap Kollu. I further declare that to the best of my knowledge, the thesis or any part of it has not been submitted for the award of any degree or diploma either in this University or any other University.

Place: Hyderabad

Date: 23 08/2022

B. Pravallika

Banoth Pravallika

Reg. No. 18PHPH17



CERTIFICATE

This is to certify that the thesis entitled "Synthesis and Characterization of multiferroic BiFeO₃ (BFO) and BFO based heterostructures for photocatalysis application" submitted by Banoth Pravallika bearing the registration number: 18PHPH17 in partial fulfilment of the requirements for the award of Doctor of Philosophy in Physics at the School of Physics is a bonafide work carried out by her under my direct supervision.

This thesis is free from plagiarism and has not been submitted previously in part or in full to any other University or institution for the award of any degree or diploma.

Further, the student has the following publications and conference proceedings before the submission of the thesis for adjudication.

Papers in Refereed Journals

 Pravallika Banoth., Sohan, A., Kandula, C., Kanaka, R.K. and Kollu, P., 2022. Microwave-Assisted Solvothermal Route for One-Step Synthesis of Pure Phase Bismuth Ferrite Micro flowers with Improved Magnetic and Dielectric Properties. ACS omega, 7(15), pp.12910-12921.

- **2. Pravallika Banoth.,** Arya Sohan., Chinna Kandula., Pratap Kollu, Structural, dielectric, magnetic, and ferroelectric properties of Bismuth ferrite (BiFeO₃) synthesized by a solvothermal process using Hexamethylenetetramine (HMTA) as precipitating agent, 31 July 2022, (https://doi.org/10.1016/j.ceramint.2022.07.208).
- **3.** Palajonnala Narasaiah, B¶., **Pravallika Banoth**¶., Bustamante Dominguez, A.G., Mandal, B.K., Kumar, C.K., Barnes, C.H., De Los Santos Valladares, L. and Kollu, P., July 20 2022. Biogenic Photo-Catalyst TiO₂ Nanoparticles for Remediation of Environment Pollutants. ACS omega, **7(30)**, p.26174.
 - \P = equally contributing authors
- **4.** Narasaiah, B. P¶., **Pravallika Banoth**¶., Sohan, A¶., Mandal, B.K., Bustamante Dominguez, A.G., De Los Santos Valladares, L. and Kollu, P., 2022. Green Biosynthesis of Tin Oxide Nanomaterials Mediated by Agro-Waste Cotton Boll Peel Extracts for the Remediation of Environmental Pollutant Dyes. *ACS omega*, **7(18)**, 2022 Apr 26, 15423-38.
 - \P = equally contributing authors
- **5.** Sohan, A., **Pravallika Banoth**., Aleksandrova, M., Nirmala Grace, A. and Kollu, P., 2021. Review on MXene synthesis, properties, and recent research exploring electrode architecture for supercapacitor applications. *International Journal of Energy Research*, **45**(**14**), pp.19746-19771.

6. The effect of graphene-Ni/NiFe₂O₄ composite on bacterial inhibition mediated by protein degradation

Acharyulu, Narayanam Phani; Sohan, Arya; Pravallika Banoth; China

Alapati, Srinivasu; Doshi, Sejal; Reddy, Venu; Santhosh, Chella;

Grace, Andrews Nirmala; De Los Santos Valladares, Luis; Kollu,

Pratap. ACS Omega, https://doi.org/10.1021/acsomega.2c02064.

Manuscript accepted with minor revision

Book chapter accepted with major revision

1. Book: Noble Metal-Free Electrocatalysts: Materials for Energy Applications

Manuscript ID: bk-2022-00295m

Title: "Introduction to Electrocatalysts"

Author(s): **Pravallika Banoth**; Kandula, Chinna; Kollu, Pratap.

Manuscripts under preparation

1. Single phase BiFeO₃ and (1-x) BiFeO₃+xFe₂O₃ heterostructure photocatalysts for photodegradation of organic dye pollutants **Pravallika Banoth** and Pratap Kollu.

2. Structural, magnetic and optical properties of BiFeO₃ and (1-x) BiFeO₃+xBTO heterostructure photocatalysts for photodegradation of organic dye pollutants

Pravallika Banoth and Pratap Kollu.

Conferences attended

1. 1st International conference on technologies for smart green connected societies 2021

Organizer: Yamagata University, Yonezawa, Japan. November 29-30, 2021.

<u>Poster presentation</u> "Microwave-assisted-solvothermal method for one-step synthesis of Bismuth Ferrite (BFO)".

2. 29th National Conference on Condensed Matter Physics

Organizer: Department of Physics, Central University of Jharkhand, Ranchi, Jharkhand. December, 10/12/2021.

<u>Poster presentation</u> "One step fabrication of Bismuth Ferrite thin films by microwave assisted solvothermal method".

Further, the student has completed the fallowing courses towards the fulfilment of course-work required for Ph.D.

S. No.	Course	Title of the Course	Credits	Pass/Fail
1	PY801	Research Methodology	4	Pass
2	PY803	Advanced Quantum Mechanics	4	Pass
3	PY804	Advanced Condensed Matter Physics	4	Pass

Dr. Pratap Kollu

Thesis Supervisor

School of Physics

Dr. PRATAP KOLLU Assistant Professor CASEST, School of Physics, University of Hyderabad, Hyderabad-500 046, India.

M. Manashyaun Head

CASEST

HEAD, CASEST
(Centre for Advanced Studies in Electronics Science & Technology)
School of Physics
University of Hyderabad-500 046.

Dean

School of Physics

DEAN School of Physics University of Hyderabad HYDERABAD - 500 046.

ACKNOWLEDGMENTS

At last, here comes the time to say thanks to respected professors, families, beloved colleagues and friends, in case I got words to say so. But first let me say simply thank you all very much.

I am pleased to express my deepest gratitude and sincere thanks to my mentor and supervisor **Dr. Pratap Kollu** for giving me an opportunity to join his research group and for supporting me in carrying out different experiments to accomplish my dream. My work was benefited greatly from his immense knowledge and commitment while I learned so much through our numerous discussions. Moreover, I would like to thank him for his caring attitude and concern. I never felt under pressure, which was not only important for me in terms of my research, but also for me personally, especially during the hard times that I had to endure.

I would also like to thank the doctoral committee of my research work, **Prof.**M. Ghanashyam Krishna, and Dr. Rajani Kanth for their valuable suggestions and useful questions.

I am thankful to the present Dean, **Prof. K. C. James Raju** and former Deans, **Prof. Ashok Chatterjee**, **Prof. V. Seshubai**, **Prof. Bindu A. Bambah**.

I would also like to extend my heartfelt thanks to **Prof. S. Srinath** for allowing me to use ferroelectric test system in their laboratory.

A big thanks also go to the lab members Ms. Arya Sohan, Mr. Chinna Kandula, Ms. U. Nireeshma, Mr. S. Rajesh and others for their love and timely help made me to enjoy in the lab. I express my gratitude to my friends and research scholars at the School of Physics. Friends who were very close to my work and encouraging me in all ups and downs of my strive in completing this

research are always be remembered and I cannot thank you enough dear colleagues.

I would like to express my heartfelt thanks to my beloved parents Late **B.**Simla and my mother **B.** Laxmi for their enormous love, kindness and faith on me. I am extremely thankful to my beloved husband **J.** Chitti Babu for his enormous love, support and affection. I also thank my brothers **B.** Ramesh and **B.** Hathi Ram for their unfailing co-operation. I also thank my father-in-law and mother-in-law for support during my Ph.D.

A big thanks non-Net fellowship provided by University of Hyderabad, NFST (No.19012/03/2018-Sch) for JRF and SRF provided by Ministry of Tribal Affairs.

Banoth Pravallika.....



DEDICATION THIS RESEARCH IS DEDICATED TO MY FAMILY



SYNOPSIS

Comprehensive details of multiferroic oxide materials and a brief review of bismuth ferrites (BiFeO₃) in particular have been presented in the first introductory chapter. The multiferroic materials are those that contain two or more orders, viz. Ferroelectricity, ferromagnetism, and Ferro elasticity exist simultaneously in one phase. The general classes of magnetism, types of multiferroics, a brief introduction to BiFeO₃ multiferroic, the origin of ferroelectricity and anti-ferromagnetism in BiFeO₃, application of multiferroic BiFeO₃, photocatalytic properties of BiFeO₃, BFO based heterostructures are some of the core topics addressed in this same chapter. In addition, A brief survey of the literature highlighting the interest in pure and BFO-based heterostructures is made. This chapter concludes with the aim and scope of the thesis.

In chapter two, a discussion about the experimental methods for synthesis of the multiferroic powder and heterostructures has been highlighted. The synthesis techniques elaborated in this chapter are the wet chemical methods, hydrothermal, solvothermal, microwave-assisted solvothermal, etc. Characterization techniques have also been described in more detail in this chapter. In addition to listing all the necessary chemicals and reagents for carrying out the experiments in this present research work, experimental procedures for preparing powders and pellets are also described.

Various experimental techniques such as X-ray powder diffraction, Field emission scanning electron microscopy (FESEM) with Energy dispersive X-ray absorption spectroscopy (EDAX/EDS), Transmission electron microscope (TEM), Raman spectroscopy, Fourier transform infrared spectroscopy (FTIR), X-ray photoelectron spectroscopy (XPS), Dynamic light scattering (DLS), Vibrating sample magnetometer (VSM), Dielectric, ferroelectric measurements and U.V.- visible spectrometer that forms the basis of the studies are incorporated in this thesis and are explained in detail.

The third chapter deals with synthesising BFO through the solvothermal technique in a short reaction time of 4hrs at low-temperature 180°C using a strong organic Hexamethylenetetramine (HMTA) as a surfactant. We have optimized the HMTA concentrations (0.5, 2, 4, and 6M).

A detailed analysis of structural, magnetic, dielectric, ferroelectric and optical properties is carried out to determine the effect of HMTA in the system. The XRD patterns, FTIR, and Raman analysis on powder BFO samples have revealed the formation of pure phase BFO

with 6M HMTA, and BFO samples synthesized with 0.5, 2, and 4M revealed the formation of unreacted phases. This XRD analysis shows that the organic surfactant strongly affects the nucleation and dissolution of the precursors. The FESEM analysis observed that the BFO powder comprises many uniform nanostructures of several nanometres embedded in several grains. Dielectric measurements have also been considered in the frequency ranges of 100 Hz – 20 MHz at room temperature. Among the four BFO samples synthesized with different HMTA concentrations (0.5, 2, 4 M), BFO with 6M HMTA exhibited a high dielectric constant value and moderate dielectric loss. The room temperature magnetic properties of these samples have been studied by the vibrating sample magnetometer, and the high saturation magnetization was calculated for the sample, which was synthesized with 6M HMTA (0.72 emu/g), which was high magnetization values compared to the previous works related to the solvothermal synthesis of BFO. From the ferroelectric studies, it has been observed that the ferroelectric properties of this sample are very weak; this may be due to the formation of oxygen vacancies in this system. Pure phase BFO has shown excellent optical properties in the visible range. However, the photocatalytic activity is very poor compared to the other photocatalysts.

Chapter four deals with the synthesis of BFO using a simple and cost-effective technique, i.e., microwave-assisted solvothermal synthesis. This method used a simple domestic microwave oven and acid digestion vessel to produce pure phase BFO rapidly. We have optimized the microwave power level, duration and concentration of the mineralizer (KOH) to study its effect on the structural, magnetic, dielectric, ferroelectric and optical properties. For our experiments, we used a domestic microwave oven (Panasonic, 23L) and a customized microwave acid digestion vessel (model: 4782, Parr). To compare the microwave technique utilized in our experiments with the commercially available microwave hydrothermal system (Model: Anton Paar Rotor 16), we have also synthesized BFO at 650W for 15 min using four vessels (maximum capacity of the system is 16 vessels) of the commercial system after optimizing the conditions. Later, the XRD, FTIR and Raman results of the samples obtained from these techniques were compared to check for versatility in obtaining pure phase BFO. After these optimal studies, we conducted a systematic structural analysis for all these samples. From XRD, FTIR and Raman analysis, it has been observed that the highest microwave power of 800 W, shorter microwave heating time of 3 minutes and 8M KOH were the most favourable experimental conditions to obtain a pure phase BFO. FE-SEM images revealed that BFO powder synthesized

through this route is composed of spherical-shaped micro flowers. The dielectric analysis suggested that the BFO micro flowers synthesized at 800 W with 8M KOH showed a high dielectric constant. The pure phase BFO has shown weak ferromagnetic behaviour with high net magnetization values than those synthesized by the solvothermal method. Pure phase BFO exhibited poor ferroelectric properties due to the high leakage current. BFO synthesized with this method at microwave power 800 W displayed a suitable absorption property in the visible range with the bandgap of 2.25eV, respectively, which indicates that this sample could be a potential candidate in semiconductor multiferroic applications such as photocatalysis. Pure BFO have shown 33% degradation in the MB solution under sunlight.

In the chapter-5, we synthesized a (1-x) BiFeO₃ + xFe₂O₃ (x = 0.10, 0.20, 0.30) heterostructures to improve photocatalytic activity of pristine BFO synthesized by microwave-assisted solvothermal method, whose bandgap is narrow, i.e., 2.25 eV. We have studied the detailed analysis of heterostructure's structural, morphological, magnetic, and photocatalytic activity.

A BFO heterostructure formed by n-type ferromagnetic Fe₂O₃ is lower than pristine BFO and is expected to reduce recombination rates of photogenerated electrons and holes; therefore, electrons and holes move from one semiconductor to another and reduce the recombination rate.

Reusability and stability are the essential factors determining the practical applicability of any photocatalyst. The XRD and FE-SEM analysis of the heterostructures (1-x) BFO + x Fe₂O₃ have revealed the formation of BFO+Fe₂O₃ heterostructures without forming any secondary phases. The magnetic properties of synthesized BFO, α - Fe₂O₃, BFOF10, BFOF20 and BFOF30 have shown improved magnetic properties than pure BFO. The enhancement in these structures' magnetic properties is expected to improve the pristine BFO's reusability significantly. All synthesised samples' optical absorption spectra are measured using UV-visible-NIR spectra. Our results have shown that all the samples BFO, α - Fe₂O₃, BFOF1, BFOF2 and BFOF3 showed a broad optical absorption in the visible spectrum ranging from 300 -800 nm identical to UV-vis-spectra reported for single-phase and its heterostructures. The formation of BFO heterostructure by loading different ratios of 10, 20 and 30% of Fe₂O₃ onto pristine BFO significantly decreased its bandgap. We have studied the photocatalytic activity of synthesized (1-x) BFO + x Fe₂O₃ (x=0.10, 0.20, 0.30) heterostructures against methylene blue (MB). All the heterostructures have shown improved photocatalytic efficiency against MB than pure BFO.

In this chapter six, we have synthesized another BFO based (1-x) BiFeO₃ + x BTO (x = 0.10, 0.20, 0.30) heterostructure by adding black TiO₂ (1.68 eV) onto the BFO to improve the photocatalytic activity and reusability of pristine BFO. We have studied the detailed analysis of heterostructure's structural, morphological and photocatalytic activity against MB. There are few reports available on the enhancement of the photocatalytic activity of pristine BFO by adding white TiO₂ to the BFO (UV active photocatalyst), whose bandgap (3.3 eV) is wider than the bandgap (2.5 eV) of pristine BFO; however, significant enhancement in the photocatalytic activity of pristine BFO was not seen after the formation of BFO+ White TiO₂ heterostructure, this might be due to the wider bandgap of the heterostructures. Here in our work, for the first time, we have synthesized BFO-based heterostructure by loading black TiO₂ (BTO, visible, active photocatalyst) whose bandgap (1.68 eV) is lower than the bandgap of BFO (2.25 eV). The heterostructure formation by loading BTO onto pristine BFO is expected to enhance its photocatalytic activity by decreasing the high charge carrier recombination rate in pristine BFO.

The XRD patterns of the heterostructures BFOT10, BFOT20 and BFOT30, where 10 and 20 and 30% BTO was added to the BFO, respectively, were well indexed to all the characteristic peaks of the pure rhombohedral phase BFO and less intense peaks of hexagonal anatase and rutile phases of BTO. The microstructure of these pristine BFO, BTO and heterostructures were done to the effect of microstructure on photocatalytic activity of the prepared samples.

The optical absorption spectra of all the synthesized samples are measured using UV-visible-NIR spectra. Our results have shown that all the samples BFO, BTO, BFOT10, BFOT20 and BFOT30 showed a broad optical absorption in the visible spectrum ranging from 400 -800 nm. From the photocatalytic activity test, it has been observed that all the BFOT10, BFOT20 and BFOT30 have shown excellent photocatalytic activity compared to the pure phase BFO. From these studies, it has been observed that BFOT30 is the most efficient catalyst with the highest degradation efficiency of 97% degradation in MB. However, BFOT30 have shown poor stability and recyclability compared to BFO+Fe₂O₃ heterostructures.

The seventh chapter, which serves as the last chapter, summarizes several significant findings from this study. Future work goals include synthesizing BFO thin films using microwave aided solvothermal, carrying out additional characterization procedures, and researching the potential of the materials for use in photovoltaic and photocatalytic applications, among other things.



List of Abbreviations

AFM Antiferromagnetic

BFO BiFeO₃

BTO Black TiO₂

HMTA Hexamethylenetetramine

T_C Curie temperature

 T_N Neel temperature

FE Ferroelectric

M-H Magnetization versus Magnetic field

P-E Polarization versus Electric field

RT Room Temperature

MW Microwave

MWAST Microwave-assisted solvothermal

MB Methylene Blue

SEI Secondary Electron Image

BEI Backscattered electron image

PVA Polyvinyl alcohol

XRD X-Ray Diffraction

ICDD International centre for diffraction data

FESEM Field emission scanning electron microscope

EDAX Energy dispersive electron microscope

TEM Transmission electron microscope

XPS X-ray photoelectron spectroscope

VSM Vibrating sample magnetometer

Table of Contents

DECL	ARATIOI	N			ii
CERT	IFICATE				iv
ACKN	IOWLED	GEMENTS			X
SYNC	PSIS				xiv
СНА	PTER	1			1
Intr	oductio	on and Liter	rature	Review	1
1.1	Introd	uction to mult	iferroics	3	1
1.2	Impor	tance and App	lication		1
1.3	Backg	round and His	torical (Overview	2
1.4	Micro	scopic Origin			4
	1.4.1.	Magnetism			4
		1.4.1.1. Type	es of ma	gnetism	5
	1.4.2.	Ferroelectricit	у		9
1.5	Types	of Multiferroi	c mater	ials	9
	1.5.1.	Multiferroics	of type	e I	10
		1.5.1.1.	ABO	3 Perovskite	10
		1.5.1	1.1.	BiFeO ₃	10
	1.5.2.	Type-II. Mul	tiferroic	es	15
1.6.	Multif	erroic Heteros	tructure	es	15
1.7.	Litera	ture Review			18
	1.7.1.	Synthesis of	BiFeO ₃	using Different Techniques	18
		1.7.1.1.	Soli-S	State technique	18
		1.7.1.2.	Wet c	chemical methods	19
		1.7.1	2.1.	Co-Precipitation method	19
		1.7.1	.2.2.	Sol-gel method	20
		1.7.1	23	Microwave-assisted solvothermal method	20

1.8.	Motiv	ation and Ob	ion and Objectives of the present thesis work					
REFE	ERENCE	ES		23				
СНА	PTER .	2		27				
Ехре	erimen	tal and ch	aracterization technique	27				
2.1.	Introd	uction		27				
2.2.	Synthe	esis techniqu	es employed	28				
	2.2.1.	Solvotherm	nal method	28				
	2.2.2.	Microwave	-assisted solvothermal method	28				
		2.2.2.1. Fac	etors that affect the rate of reaction in microwave syst	em				
				29				
	2.2.3.	Coprecipita	ntion method	31				
	2.2.4.	Pellet prepa	aration	31				
2.3	Mater	ial Character	ization	32				
	2.3.1.	Physical an	d Structural Characterization	32				
		2.3.1.1.	X-ray diffraction	32				
		2.3.1.2.	Field Emission Scanning Electron Microscopy	33				
		2.3.	1.2.1. Energy Dispersive X-ray Spectroscopy	34				
		2.3.1.3.	Fourier Transform Infrared Spectroscopy	34				
		2.3.1.4.	Raman Spectroscopy	35				
		2.3.1.5.	Transmission Electron Microscopy	36				
		2.3.1.6.	X-ray photoelectron microscopy	38				
		2.3.1.7.	UV-Vis spectroscopy	38				
	2.3.2.	Electrical p	roperties	40				
		2.3.2.1.	Dielectric properties	40				
		2.3.2.2.	Ferroelectric properties	42				
	2.3.3.	Magnetic p	roperties	42				
REFE	ERENCE	ES		44				

CHAPTER 3 47

by a	solvo	and Characterization of Bismuth ferrite (BiFeO ₃) sthermal process using Hexamethylenetetramine (and agent	•		
Objec	ctives		47		
3.1.	Introd	uction	47		
3.2.	Exper	imental Section	49		
	3.2.1.	Materials used in the synthesis	49		
	3.2.2.	Synthesis of BFO by Solvothermal technique	49		
3.3.	Charae	cterization Techniques utilized	50		
3.4.	Results and Discussions				
	3.4.1.	X-ray diffraction analysis of BFO Powders	51		
	3.4.2.	FE-SEM Micrographs of BFO powders	54		
	3.4.3.	Fourier transform infrared spectroscopy analysis	55		
	3.4.4.	Raman analysis	56		
	3.4.5.	Dielectric properties of BFO samples	59		
	3.4.6.	Room temperature Magnetic behaviour of BFO	61		
	3.4.7.	Room temperature Ferroelectric behaviour of BFO	62		
	3.4.8.	Optical properties of pure phase BFO	64		
	3.4.9.	Photocatalytic activity of pure phase BFO	66		
3.5.	Concl	usion	67		
REFI	ERENCE	ES	69		

75

Micro	wave-assis	sted solv	otherm	al route	for o	one-step	syn	thesis	of j	pure
phase	Bismuth	Ferrite	micro	flowers	with	improv	ed	magne	tic	and
dielect	ric propei	rties							75	

Objec	etives	75
4.1.	Introduction	75
4.2.	Experimental Section	77
	4.2.1. Materials	77
	4.2.2. Synthesis of BFO	77
4.3.	Characterization Techniques	79
4.4.	Results and Discussions	79
	4.4.1. Structural analysis	79
	4.4.2. Microstructural analysis	84
	4.4.3. Transmission electron microscopy analysis	86
	4.4.4. Fourier Transform Infrared Spectroscopy analysis	87
	4.4.5. Raman analysis	88
	4.4.6. X-ray Photoelectron Spectroscopy analysis	89
	4.4.7. Dielectric analysis	91
	4.4.8. Magnetic Properties	93
	4.4.8.1. Influence of KOH concentration on magnetic properties of BFO	95
	4.4.9. Ferroelectric properties	96
	4.4.10. Optical properties of pure phase BFO	97
	4.4.11. Photocatalytic activity of pure phase BFO	98
4.5.	Conclusion	99
REFE	ERENCES	101

CHAPTER 5	109
-----------	-----

Structural,	magnetic	and	optical	properties	of	BFO-based	(1-x)
BiFeO ₃ +xFe	2O3 heteros	struct	ure phot	ocatalysts fo	r pl	hotodegradat	ion of
organic dye	pollutant						109

Objec	ctives	109
5.1.	Introduction	109
5.2.	Experimental Section	111
	5.2.1. Materials	111
	5.2.2. Preparation of BiFeO ₃ micro flowers	111
	5.2.3. Preparation of hollow Fe ₂ O ₃ microspheres	111
	5.2.4. Synthesis of (1-x) BFO+xFe ₂ O ₃ (x = 0.10, 0.20, 0.30)	111
5.3.	Characterizations	112
5.4.	Photocatalysis	112
5.5.	Result and Discussions	112
	5.5.1. XRD analysis of the heterostructures	112
	5.5.2. FE-SEM images of heterostructures	114
	5.5.3. Optical properties of BFO+Fe ₂ O ₃ heterostructures	115
	5.5.4. Photocatalytic activity of BFO+Fe ₂ O ₃ heterostructures	116
	5.5.5. Effect of Photocatalyst concentration on efficiency	118
	5.5.6. Stability and Magnetic recovery of Photocatalysts	119
5.6.	Conclusion	122
REFE	ERENCES	123

CHA	PTER (6	129
	•	ght active $(1-x)$ BiFeO ₃ + x BTO photocatalyst for vtic degradation of Methylene Blue	129
Object	tives		129
6.1.	Introd	uction	129
6.2.	Experi	mental Section	131
	6.2.1.	Materials used for BFO+BTO heterostructures	131
	6.2.2.	Preparation of BiFeO ₃ micro flowers	131
	6.2.3.	Preparation of black TiO ₂ (BTO) nanoparticles	131
	6.2.4.	Synthesis of (1-x) BFO+TiO ₂ ($x = 0.10, 0.20, 0.30$)	131
6.3.	Charac	cterizations	131
6.4.	Photo	eatalysis	132
6.5.	Result	and Discussions	132
	6.5.1.	XRD analysis of BFO+BTO heterostructures	132
	6.5.2.	FE-SEM analysis of BFO+BTO heterostructures	133
	6.5.3.	Optical properties of BFO+BTO heterostructures	134
	6.5.4.	Photocatalytic activity of BFO+BTO heterostructures	136
	6.5.5.	Effect of Photocatalyst concentration on photocatalytic efficiency	137
	6.5.6.	Reusability and magnetic recovery test for BFO+BTO photocataly	sts 139
6.6.	Conclu	usion	141
REFE	RENCE	ES	142

CHA	PTER 7		145
Overa	all Summar	y and Future Work	145
7.1.	Overall	l Summary	145
	7.1.1.	Synthesis of BFO through the solvothermal method	147
	7.1.2.	Synthesis of BFO through microwave solvothermal method	od 148
	7.1.3.	Photocatalytic activity of BFO+Fe ₂ O ₃ heterostructures	149
	7.1.4.	Photocatalytic efficiency of BFO+BTO heterostructures	150
7.2.	Future	Work Plan	151
SUPPI	LYMENTARY	DATA	i
A.	XRD data of	BFO synthesized by commercial microwave oven	i
B.	XRD pattern	of BFO synthesized by domestic microwave oven at diffe	erent MW
	duration at di	fferent MW power	ii

CHAPTER-1

Introduction and Literature Review

1.1. Introduction to multiferroics

Materials known as multiferroics display multiple types of ordering simultaneously, including magnetic, electric, and elastic orders. Employing exchange interactions among magnetic dipoles, which develop from empty electron atomic orbitals, magnetic ordering is typically generated. Electric dipoles generate electrical order through their arrangement. The elastic order that results from atomic displacements caused by strain is what we refer to as atomic displacements. Magnetic and electric order coexist because they combine properties that can be used to process, store, and transmit information. It enables interaction between the electric and magnetic orders and the electric and magnetic fields. Local polarisation is usually prevented by partial d-atomic orbitals, which are associated with magnetic moments and vacant d-shells or electron pairs. As a result, this feature is extremely rare (figure 1.1).

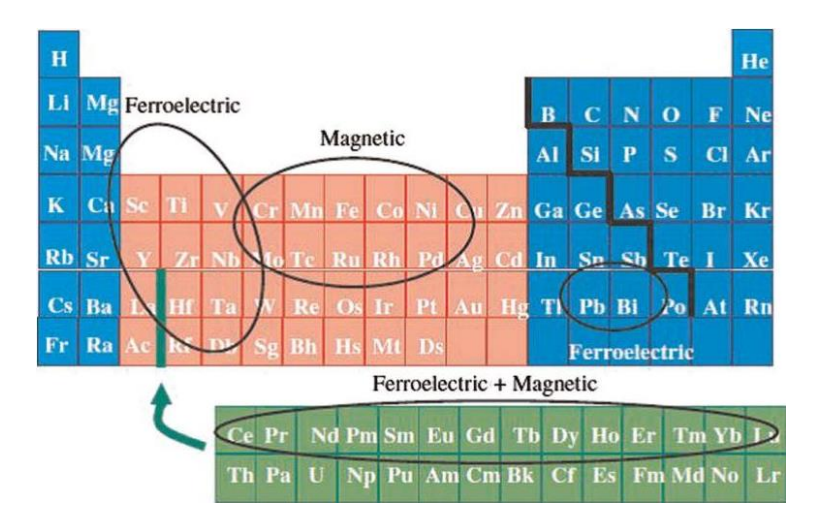


Figure 1.1. elemental periodic table emphasising the constituents responsible for magnetic and ferroelectric properties [1].

1.2. Importance and Applications

Among the most popular non-volatile storage mediums are tapes, hard drives, and so forth; ferromagnetic materials are often used. In addition to storing information, they are used for processing electric current, light, and magnetic order. Ferroelectric materials are widely used due to their significant piezoelectric coupling constants when an electric field is

combined with strain. This effect highlights the elements that produce magnetic and ferroelectric behaviour in the periodic table of the elements, as shown in **figure 1.1**. Devices such as microphones, transducers, and capacitors, which are constructed of multiferroic materials, are places where voltage can cause strain. Ferroelectric materials have memory properties in addition to piezoelectric coupling, typical of most materials without inversion symmetry. After removing an imposed electric field, the electric polarization is still finite. Electric polarization can be used in non-volatile memory systems, once the power has been turned off, data is retained in the polarization. Presently, the market is witnessing the introduction of such products. Multiferroics are a topic of great interest because magnetic and electric orders are simultaneous, switching electric polarization can be accomplished by applying an electric field and a magnetic field, or vice versa, or by delivering magnetic and electric fields. This characteristic makes it possible to create entirely new device architectures. Moreover, understanding chemical bonding enables materials scientists to build bulk compounds and thin films that avoid electrons. The most promising application for multiferroics is electrically written memory devices that are non-destructive, minimally power-consuming, and can be read by magnetic fields [2]. To achieve this, the materials used in microelectronic devices must be highly insulating, have polarization that can be switched, and have a strong coupling between the electric and magnetic fields at room temperature.

1.3. Background and Historical Overview

According to Curie, an electric field can induce magnetism and electric polarisation to produce the magnetoelectric effect. Later on, it was asserted that no such impact could exist due to symmetry issues. It was discovered and used in the 1940s that ferroelectric materials such as BaTiO₃ had features that made them attractive to multiferroic material researchers during the 1960s. Based on the 1982 review article by Smolenski and Chupis on multiferroics, about 50 different multiferroic materials are listed [3]. New multiferroics have been created due to the identification of additional ferroelectricity-causing mechanisms in recent years, both experimentally and theoretically. As a result of Kimura et al.'s discovery of ferroelectricity within TbMnO₃, a significant amount of progress has been made in this field [4]. Spin order differs from electric order in this case for the Mn ions. Furthermore, the concept of multiferroics has become much clearer as the theory progressed of ferroelectricity and the chemical bonds that underlie it.

Recently times have seen a surge in interest in materials that may be ordered in two ways: magnetically and electrically. If magnetic and electric characteristics can be jointly regulated, new gadgets may be possible. Maxwell's equations, which link electric and magnetic fields, charge density, and current density, demonstrate the coupling between magnetic and electric interactions. According to the theory of ferroelectric and ferromagnetic materials, there are many parallels between their response in external fields and domain structures, which their formal equivalence may explain. The fact that ferroelectricity and magnetism in solids come from distinct places explains these surprising parallels. Materials with incomplete ionic shells exhibit magnetism and ferroelectricity, whereas multiferroics materials have two or more main ferroic characteristics in the same stage in **figure 1.2**.

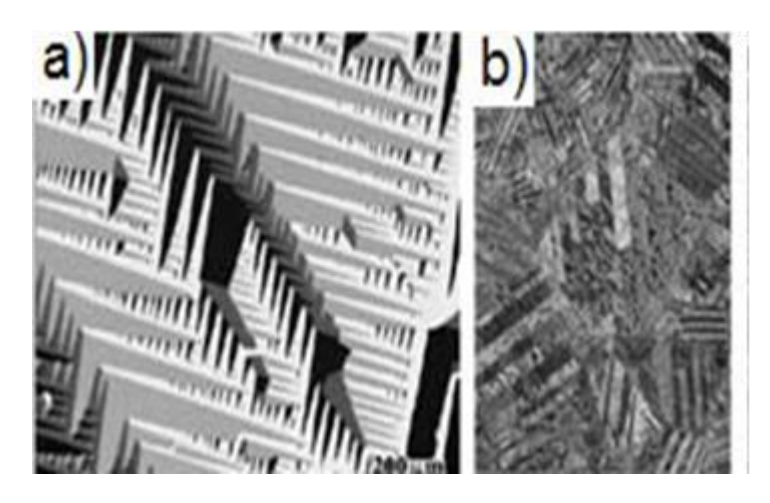


Figure 1. 2. Magnetic domains of Ferroelectric [5].

Anti-ferromagnetism, for example, has been added to the list of long-range orders included in the multiferroics description (**figure 1.3**). Thus, multiferroics materials combine more than one of these characteristics. Nowadays, "multiferroics" describes a material that exhibits ferroelectricity and magnetism (ferromagnetism and anti-ferromagnetism). If the magnetization and polarization are tightly correlated in multiferroics, then magneto-electric switching is possible. This is a very rare event. Theoretical work in 1959 suggested that a single material may have magnetic and electric degrees of freedom coupled together [6]. In these materials, the magnetization and polarization are directly proportional to the applied electric field and magnetic field. This form of interaction was later found and is now referred to as the linear magneto-electric effect. A new material with at least two forms of ordering ferromagnetism and ferroelectricity was then created in the following phase. Soviet scientists were the ones who made this happen. Despite this, multiferroics research was mostly abandoned shortly after this event. Multiferroics are not all linear

magnetoelectric because of rigorous crystal symmetry requirements; instead, higher-order coupling factors dominate. Around 2013, there was a resurgence in interest in multiferroics. This is due to several factors: The discovery of magnetically induced ferroelectricity. Here, spin frustration often causes spiral antiferromagnetic ordering that induces ferroelectricity.

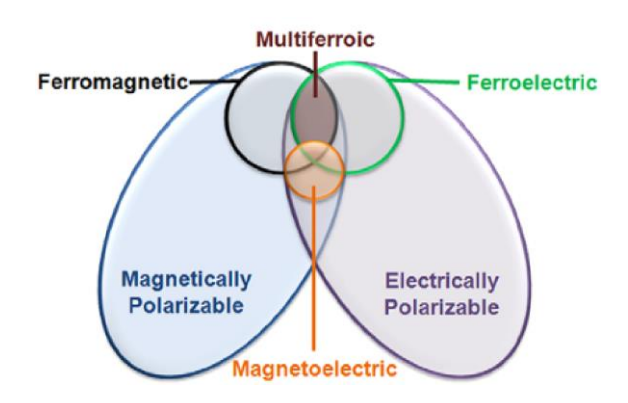


Figure 1. 3: Ferroelectricity and magnetism are combined in multiferroics [6].

Materials with strong magnetic and electrical properties are used extensively in everyday life and modern technology. In addition to being electrically and magnetically active, multiferroic materials can perform multiple functions in a single structure due to the miniaturization of devices. The magnetoelectric effect allows data to be stored in magnetic memory controlled by an electric field. In addition to having the properties of both magnetic and ferroelectric materials, multiferroics also have magnetoelectric properties makes them attractive. It's still a significant concern whether these materials can be used since the magnetoelectric coupling is too weak; additionally, the polarization or magnetization is frequently too tiny, and the temperatures at which these orders occur are too low. Because of this, the development of novel materials is a must.

1.4. Origin at the microscopic level

1.4.1. Magnetism

For magnetic order to exist, magnetic moments and their exchange must exist. Magnetism is mainly restricted to partially filled d- and f-shells in materials at ambient temperatures. The actinides and rare earth are f-shell elements. In gases below 50 K, the valence electrons protect f-electrons from the surrounding atoms, resulting in weak interactions between the f-electrons. Consequently, magnetism for d-shell materials, including transition metals, is limited primarily to 3d-elements because of the low electron spin in 4d- and 5d- elements. Fe, Ni, Mn and Co show net magnetic moment without a magnetic field. At these

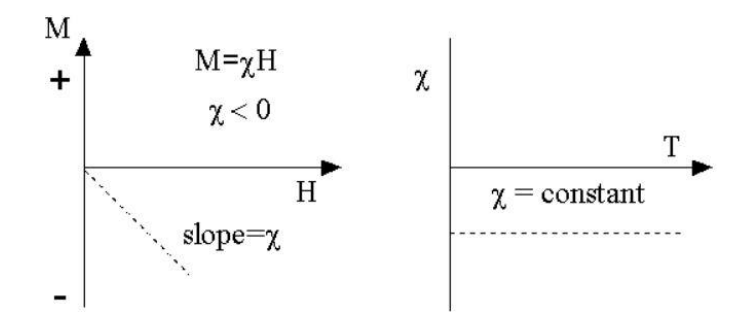
temperatures, magnetic order can develop due to intense direct exchange interactions. The complete screening of any local electric dipole often results in metallic behaviour and prevents electric order. As a result, multiferroic activity is only found in materials having indirect exchange contacts, like oxides, where the ligands of the transition metal act as a medium for magnetic interactions. Despite the lower magnetic ordering temperatures, as a result, many oxides still show magnetic order when heated above room temperature. A double interaction frequently acts as the driving force behind ferromagnetic interaction in oxides. The resultant metallic state screens the production of electric dipoles, just as it does with direct interactions. The presence of Dzyaloshinskii-Moriya couplings or local anisotropy effects causes antiferromagnets to spin, which makes these sources likely to be involved in magnetic materials interaction for multiferroics [7].

1.4.1.1. Magnetism types

Everything in and around us is magnetic since all matter consists of atoms with flowing charged particles. That's because they're everywhere: in AC and DC motors that do a wide range of work, in power distribution systems built around power transformers that deliver electricity to both the home and industry, in massively scaled-up applications for video and audio, in super-fast telecommunication systems that link continents like light, in massively scaled data storage. Depending on how the spins are oriented, magnetism can be described as diamagnetic, paramagnetically oriented spins, ferromagnetic, antiferromagnetic, and ferrimagnetic. The different kinds of magnetism are briefly explained in the next section.

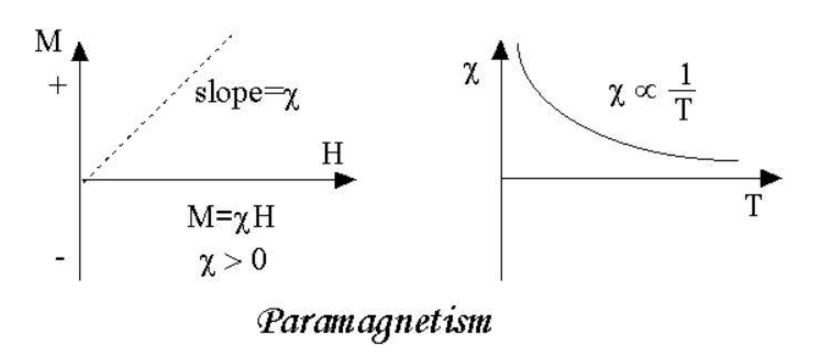
Diamagnetism

All matter has diamagnetism as a fundamental characteristic, though it is typically relatively weak. This happens because electrons in orbit cannot align themselves to the applied magnetic field. Diamagnetic materials are atoms without net magnetic moments (i.e., all electrons are paired and orbital shells are filled). As a result, the susceptibility is negative when subjected to a field that generates a negative magnetization. The following is what we observe if we plot M and H: Whenever there is no field, magnetization is absent. Another true thing about diamagnetic materials is that their susceptibility is not affected by temperature. The relationship between M-H is shown below;



Para magnetism

These materials have atoms or ions with partial orbitals filled with unpaired electrons, leading to a net magnetic moment. It is important to note that iron contains unpaired electrons and is one of its most essential atoms. Due to the non-interaction of the individual magnetic moments when the field is removed, the net magnetization is zero. A field causes the magnetic moments to partially align in the direction of the applied field, resulting in positive susceptibility and net positive magnetization. That field's effectiveness in aligning moments is also countered by allowing a more significant effect of temperature. As a result, temperature affects susceptibility following Curie's Law. When temperatures are normal, and fields are moderate, a small amount of paramagnetic susceptibility is present. The paramagnetic susceptibility is independent of the applied field except when the temperature is very low (<<100 K). This condition results in a proportional phenomenon between paramagnetic susceptibility and iron contents. The relationship between M-H is shown below;



Ferromagnetism

Ferromagnetism may be explained by the Curie-Weiss localized moment and the Stoner band theory [8], which have been proposed to explain various ferromagnetism features. In the hypothesis of electron localization put out by Weiss [figure 4], electrons are thought to be restricted to specific energy levels. The angular momentum of an electron is what gives

it its energy. Because of the molecular field, electrons are all lined up in a row. This molecular field originates from the energy exchanged between particles in quantum mechanics. There are no restrictions on electron movement in the Stoner model.

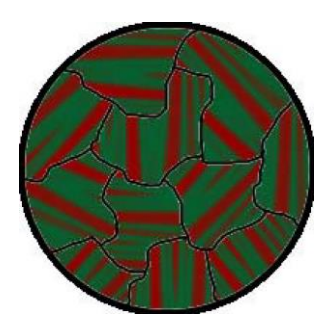
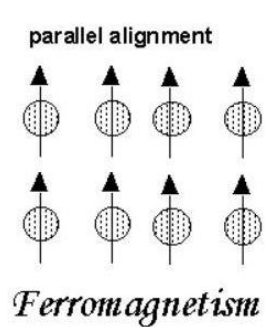


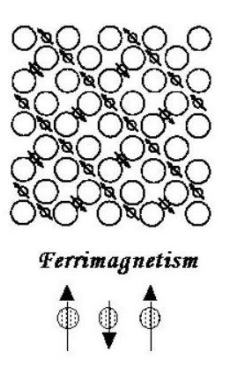
Figure 1. 4: Weiss domain structure [8].

If all electrons have the same spin, the exchange energy is reduced. In most people's minds, the first magnetic materials that come to mind are iron, magnetite, and nickel. These materials' atomic moments, as opposed to paramagnetic ones, show extraordinarily potent interactions. A parallel or antiparallel alignment of moments of atoms is the outcome of these interactions caused by electronic exchange forces. The transfer forces are enormous, around 100 million times stronger than the Earth's field, or equivalent to a field of 1000 T. Since the spins of two electrons are oriented differently, the interchange force is a quantum mechanical event. Even without a magnetic field, ferromagnetic materials have moments aligned parallelly, which results in significant net magnetization. The alignment of the magnetic dipoles is shown below;



Ferrimagnetism

Magnetic ordering can take a more complicated form in ionic compounds, such as oxides, due to their crystal structures. Magnetism has several types, including ferrimagnetism. The magnetic spins of ferrimagnetic oxide are depicted in the illustration below.



The dipole moments of the A and B sublattices aren't equal in ferrimagnets, leading to a net magnetic moment. Therefore, ferrimagnetism and ferromagnetism are comparable. It displays all the characteristics of ferromagnetic behaviour, including spontaneous magnetization, hysteresis, remanence and Curie temperatures. Ferro- and ferrimagnets, nevertheless, exhibit extremely distinct magnetic orderings.

Anti-ferromagnetism

There is no net moment if the sublattice moments of A and B are precisely equal, even if they are opposite. We can observe how susceptibility behaves above the Neel temperature (T_N), a critical temperature for anti-ferromagnetism. There is no macroscopic magnetism in antiferromagnetic materials because of electron spins. Antiferromagnetic ordering may be seen at low temperatures in certain materials, which transition from a paramagnetic state. Antiferromagnetic relations may produce multiple states with various energy.

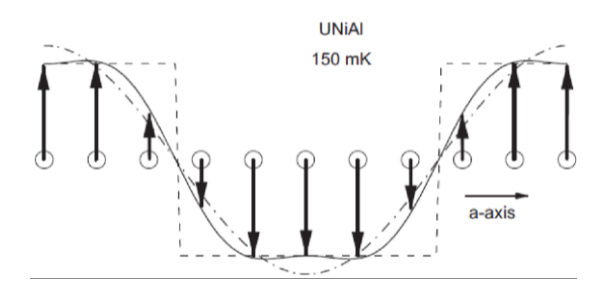


Figure 1. 5. The empirically determined modulation of the AF structure is shown in this diagram [9].

Antiferromagnetic ordering is a common property of transition metal complexes. With zero net moments, an antiferromagnetic material may have a wide variety of distinct spin structures, including regular patterns with adjacent spins pointing in the opposite direction (**figure 1.5**).

1.4.2. Ferroelectricity

There is widespread knowledge that ferroelectricity is caused by polarisation catastrophes or soft modes [10]. By symbolizing a cation with a point charge, it is possible to demonstrate that while it is in the middle of its anionic ligands, it cannot remain stable. Cationic transition metals locate their ligands with respect to each other based on the equilibrium between the Coulomb force and the electrical repulsion between their core electrons. Spinels are characterized by their faced cubic oxygen sub-lattice traditional ionic crystal formed by anions packed closely together. After that, the cations fill the interstitial sites. In most cases, such dense packing produces face-centred structures. Magnetism necessitates a partially complete d-shell for transition metals, and only very small ionic radius ions, such as lithium, exhibit off-centre positions. The d⁰ -elements Ti⁴⁺, Zr⁴⁺, and Nb⁵⁺ are thus determined to belong to the first group of ferroelectrics. Titanates, zirconates, and niobates are the names of these oxides. The second group of ferroelectrics is discovered when looking at materials that have a lone-pair arrangement. This arrangement is typical in heavy p-elements such as Bi³⁺ and Pb²⁺. In this case, the cation is not in the same place as the other cations. This is because the lone pair is interacting with the ligands. When both mechanisms are active simultaneously, as in Pb (Zr, TiO₃ (PZT), the ferroelectric polarisation is at its maximum. The cation in this instance is positioned off-centre from the other cations due to the interaction of the lone pair with the ligands. When both mechanisms are active at the same time, as in PZT, where d0 and the Ti⁴⁻ and Pb²⁺ions make a significant contribution to the ferroelectric polarisation, the result is maximum polarisation. The need for several accessible minima with finite polarisation in the entire energy landscape is caused by the requirement that ferroelectrics reverse their polarisation when an electric field is applied.

1.5. Types of multiferroic materials

There are two different kinds of multiferroics: type I multiferroics and type II multiferroics. Ferroic orders can arise in multiferroics of type I independently of one another, which gives these materials their name. Ferroic orders can arise in multiferroics of type I independently of one another, which gives these materials their name. The individual order parameters can be highly polarized and temperature-dependent. Magnetoelectric and ferroelectric interactions, however, are usually weak.

The second group, called Type II multiferroic materials, has ferroelectric polarisation caused by spin order.

1.5.1. Multiferroics of type I

1.5.1.1. ABO₃ perovskites

As shown in **figure 1.6**, many ferroelectric materials contain BO_6 octahedra with eight octahedra sharing corners. Further, transition metal lone-pair ions with the configuration of electron d^0 can contribute to the ferroelectric moment by sharing electrons with lone-pair ions, such as Pb^{2+} or Bi^{3+} . The B-site in rare-earth ions or transition metal ions can produce magnetism, as can the A-site in transition metal ions. Some compounds, including Pb (Fe $W_{1/3}$) $W_{1/3}$ $W_{1/3}$ W

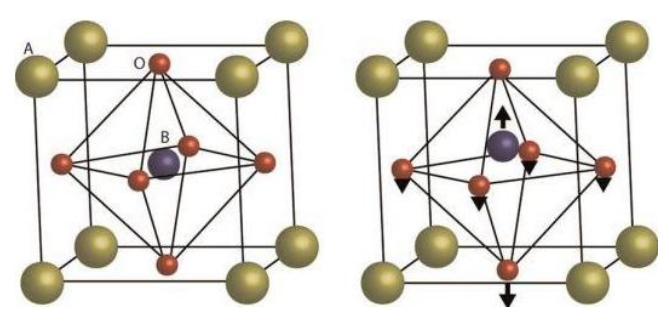


Figure 1. 6. ABO₃ perovskite tetragonal crystal structure with ferroelectric distortion [11].

1.5.1.1.1. BiFeO₃

Crystal structure and compositional phase diagram of BiFeO₃

The chemical formula for bismuth ferrite at room temperature, BiFeO₃ (abbreviated BFO), is a well-known perovskite (ABO₃) structured material. BFO is a rhombohedral deformed perovskite structure which belongs to the R_{3c} space group. Another way to look at the structure of BFO is to use the pseudo cubic symbol 111 to link two deformed perovskite unit cells with their body diagonals bent at an angle of 89.45° to produce a rhombohedral unit cell [12], as illustrated in **figure 1.7**.

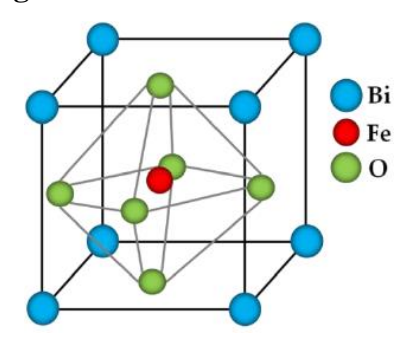


Figure 1. 7. A perovskite (ABO₃) structure of multiferroic BiFeO₃ [6].

The physics underpinning multiferroic materials' specific functionalities has been the subject of decades of BFO research. As a result of the stereochemistry of Bi 6s² lone pair electrons and the partly filled 3d orbital of Fe³⁺ ions, BFO exhibits ferroelectricity and antiferromagnetic, respectively. Considering a BFO crystal unit cell, the Fe ion magnetic moments are Ferro- and antiferromagnetically linked inside the pseudocubic (111) planes. Since established G-AFM spin propagates at an incommensurably long wavelength of 62nm, the macroscopic magnetization is cancelled, limiting the linear ME characteristic. Using Fe magnetic moments aligned perpendicular to the plane [111] axis of the BFO, it is possible to create "canted" AFM sub-lattices, which results in a weak magnetic field. Bismuth ferrite (BiFeO₃, BFO) is a popular choice for room-temperature multiferroics due to its rarity. After investigating BFO material in 1960, Smolensky [13] and colleagues were unable to develop single crystals and monophasic polycrystalline crystals. BFO singlephase polycrystalline BFO was first synthesized by Achenbach et al. back in 1967 [14]. Indeed, the finding of substantial residual polarization in BiFeO₃ thin films in 2003 and ferromagnetism, 15 times greater than that of the bulk, attracted much interest to BFO. Since then, various investigations on thin film and nanostructured BFO have been conducted to reignite interest in the field. The unusual mix of practical possibilities and interesting physics underpinning BFO's features has attracted materialists' interest. Its chemical formula is simple yet has a wide range of characteristics. Magnetic symmetry features and unique electronic configurations, which hold the key to the coexistence of magnetism and polarization, may never be utilised entirely. The development of a longrange magnetic cycloid that is out of phase with the lattice and canting of the spins makes antiferromagnetic ordering difficult. After it was discovered that thin films of BiFeO₃ have substantial ferroelectric polarisation (60 μ C/cm²), the study on the material exploded. Prior to the publication of this paper, ferroelectric experiments on bulk BiFeO₃ did not yield such substantial polarisation values due to the high conductivity caused by oxygen vacancies in the samples. Eventually, it was demonstrated that charged imperfections, such as oxygen vacancies, prevent domain walls from moving, generating non-saturated P-E hysteresis loops. Quenching at temperatures above the curie transition temperature, defects become random, resulting in well-intentioned loops, but still lacking the polarization value of thin films or single crystals. Low magnetoelectric coupling is anticipated since ferroelectricity and magnetism are independent. Recent studies have demonstrated [15] that switching the

direction of the magnetic field in two phases is possible using an electric field applied to BiFeO₃ thin films.

The Bi₂O₃-Fe₂O₃ system has different phases of equilibrium.

Midway through the 1960s, the first phase diagrams for the Bi₂O₃-Fe₂O₃ system were published [39]. Years later, different versions of these first diagrams [17-18] (**figure 1.8**) were published, but some differences existed. For example, in specific diagrams [17-19], the -Bi₂O₃ to -Bi₂O₃ phase shift is also enlarged to the similarity region between Bi₂₅FeO₃₉ and BiFeO₃ phases, which is seen by other authors [12] as a sign of a state that is not in equilibrium. In almost the same way, there are slight changes in the temperature where a liquid phase initially appears (from 745°C [20] to 792°C [21]), the temperature during which Bi₂Fe₄O₉ breaks down (from 934°C [21] to 961°C [22]), and the temperature at which the BiFeO₃ peritectic breaks down (from 852°C [33] to 934°C [21]), which is more Also, Palai et al. [22] say that peritectic decomposition of BiFeO₃ happens, but some other authors [23] did not think this phase is thermally stable. Attempts to demonstrate these differences have pointed to an uncontrolled level of impurities and flaws in the samples as they were prepared [23], as well as the fact that data were collected in conditions that were not stable [22]. Even though the phase visualisations agree that the BiFeO₃ phase is thermally stable at higher temperatures, there is still a lot of disagreement, and conflicting data have been published those calls both the diagram and the consistency of the BiFeO₃ phase in and out of the question.

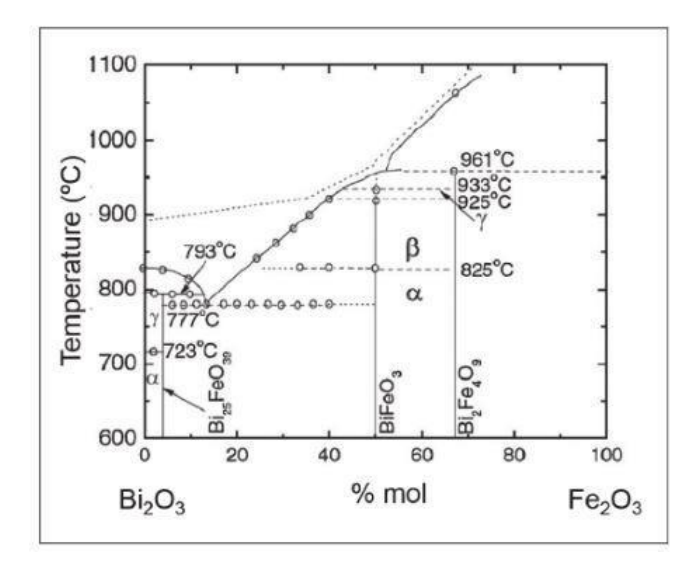


Figure 1. 8. Compositional phase diagram of BiFeO₃ [12].

Multiferroicity in BiFeO₃

R_{3c} symmetry is achieved in BiFeO₃ by displacing Bi, Fe, and O along the threefold axis, which results in an unassisted spontaneous polarization in the (111) direction. Bi³⁺ cations with a stereo chemically active 6s² lone electron pair have the most significant relative displacements from O. The orbital hybridization between the A-site cation (Bi) and oxygen is primarily responsible for the polarization. The centrosymmetric orientations of the Bi³⁺ and Fe³⁺ ions change when the phase is at room temperature. As a result, the ferroelectric permanent dipole moment is created. BFO's magnetism results from an antisymmetric Dzyaloshinskii-Moriya exchange between Fe-O-Fe and Fe-Fe-O, which localised electrons in the d-shells of B-site (Fe) ions. These six spin-down neighbours surround every spin-up neighbour in BFO's structure. A magnetic moment of Fe appears along the horizontal axis of (111), perpendicular to the plane of (111). The so-called G-type antiferromagnetic ordering is the result of ferromagnetic coupling inside the (111) planes and antiferromagnetic coupling between neighbouring (111) planes (**figure 1.9**).

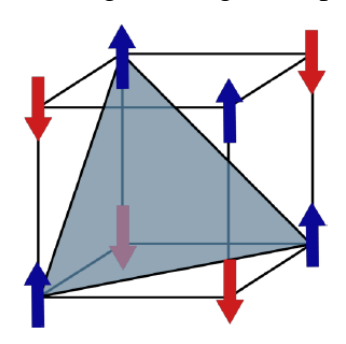


Figure 1. 9. G-type AFM [6].

The magnetic ordering here appears to be modulated incommensurate with long-range spin cycloid structures. Spins in this spiral arrangement rotate on the (110) h plane as the modulation wave vector moves in the (110) h direction. A combination of spin-orbit interactions and exchange induces spin canting away from perfect antiferromagnetic ordering to produce weak local ferromagnetism. Magnetic fields are superimposed on a spin cycloid structure of 62 nanometres in length, which leads to rotation of small moments of net magnetization, depicted in **figure 1.10**.

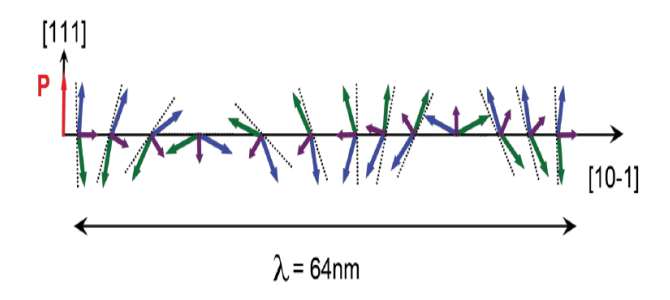


Figure 1.10. BiFeO₃'s incommensurate spiral spin structure is shown in the schematic form [9].

The antiferromagnetic sub lattices can be rotated in the (111) direction even though BiFeO₃ lacks magnetization due to the symmetry when the magnetic moments are perpendicular. Ederer and Spaldin extensively examined so-called weak ferromagnetism due to this macroscopic magnetization [13-14]. Oxygen octahedral rotates in BiFeO₃. Polar displacements in the (111) direction occur, as does polar displacement. However, only the rotation of the oxygen octahedral is associated with mild ferromagnetism. According to the theory, the direction of the DM (Dyzaloshinskii-Moriya) vector is not dictated by the direction of polarization but instead is governed by the sense of rotation in the octahedral surrounding the matching magnetic ions. Canting two antiferromagnetic sub lattices may produce a net magnetization in BiFeO₃ because the symmetry of the material permits modest ferromagnetism. **Figure 1.11** displays the antiferromagnetic spins in **figure 1.11** (a), whereas **figure 1.11** (b) shows the canting of magnetic spins revolving perpendicular to the (111) axis. Cyclic modulation is ignored in favour of only considering spin-orbit coupling.

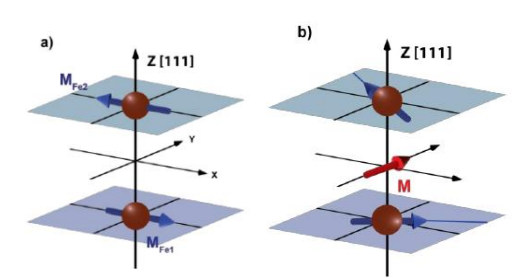


Figure 1. 11. a) Antiferromagnetic spin, and b) mild ferromagnetism [9].

Applications of BiFeO₃

Spintronic, data storage, microwave and satellite communication, actuators and switches, sensors, and optical filters may all be built with BFO at room temperature [15]. Since

Bismuth ferrite has a low band gap energy (around 2.3 eV) and exceptional chemical stability, it is an excellent photocatalyst. Photocatalytic activity may be enhanced by its ferroelectric and magnetic characteristics, as well. Developing effective photocatalytic materials is critical in light of current energy and environmental constraints. These concerns may be addressed by two unique properties of a photocatalyst, which can be explained as fallows; at the outset, the production of hydrogen gas by photo catalysis may be described as an excellent means of producing fuels without polluting the environment. As a second benefit, it may efficiently clean the environment by converting organic pollutants into water and carbon dioxide (H₂ and CO₂) without generating more pollutants [15]. As a result, knowing the photocatalytic behaviour of BFO and the optimal usage of its multiferroics characteristics will be intriguing in developing promising materials for photocatalytic applications.

1.5.2. Type II Multiferroics

Spin Order-Induced Improper Ferroelectricity

Magnetic order has a variety of ways that it might damage a material's inversion symmetry. We identify many microscopic leads to significant improvement in coupling mechanisms and go into depth on the strength of pertinent information. Based on three different magnetoelectric interaction mechanisms, materials exhibiting inappropriate ferroelectricity which result from spin sequence be classified into three groups. Materials having magnetic order belong to the first group, where symmetric exchange striction causes electrical polarisation. The second class of substances exhibits non-collinear magnetic order and permits electrical polarisation due to anti-symmetric exchanging restriction. Because the spin-orbit correlation interactions that cause the electrical polarisation are weaker than those in the original group, the resulting polarisation is weaker. Materials exhibiting spin-dependent p-d hybridization-induced electrical polarisation fall under the third class. Different coupling mechanisms may be active in some materials. We recommend Tokura et al. for a detailed assessment of multiferroics with the spin origin [24].

1.6. Multiferroic Heterostructures

Heterostructures Mechanism

The Flat band Schottky barrier is well-known in the semiconductor industry [figure 1.12 (c)]. Barriers are defined by the metal's work function and the semiconductor's electron affinity when they come into contact. Voltage does not affect the current until electrical

depletion is overcome and electrons can flow across junctions, and the likelihood of semiconductor depletion increases as the Schottky barrier alone increases. For small barriers, however, the relationship between current and voltage is linear and analogous to that of an ohmic contact. The Fermi level can be altered by doping, modifying the relationship between current-voltage behaviour. Increasing dopant concentration often increases the possibility of an ohmic contact (the Ohmic contact is a low resistance junction (non-rectifying) that provides current conduction from metal to semiconductor and vice versa). Therefore, its charge carriers to disperse by fully ionising the dopant. In the region below the conduction and valance bond, the density of states (DOS) is low. But the exact locations of the new states haven't been decided yet, so there's no way to give a new electronic band structure. No matter what the dopant is, the electronic structure of each substance is different. A metal or a semiconductor has a band gap, a range of energy levels where electrons can move when they are close to an interface.

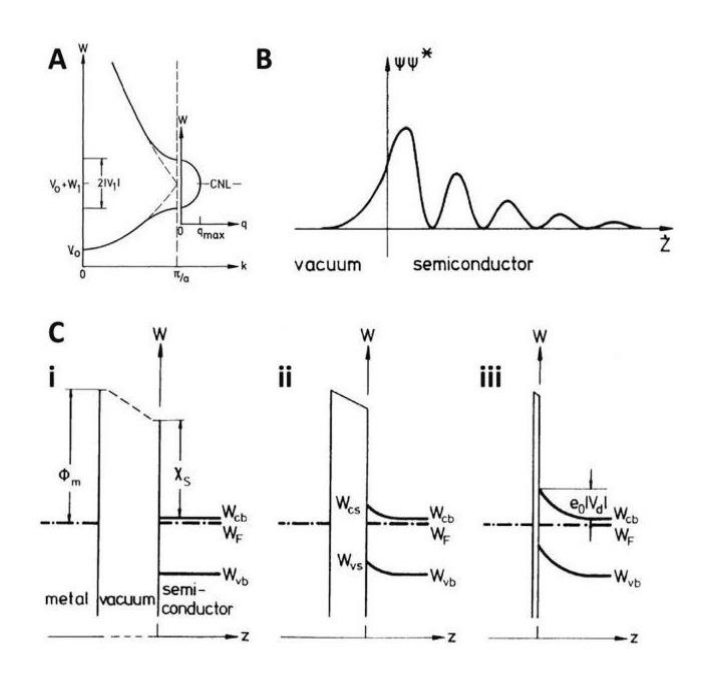


Figure 1. 12. A) shows a highly complex band structure, B) both the vacuum and the semiconductor are involved in the decay of surface states' wavefunctions, C) A study on the effect of Schottky barrier proximity to metal (i to iii) on semiconductor band bending [25].

The formation of heterojunction can be explained as fallowing: If we look at the wavefunction of an electron at its surface in a periodic setting, like an infinite one-dimensional lattice, it breaks down into its semiconductor and vacuum parts [figure 1.12]

(B)]. Figure 1.12 (C) shows how the bands look at the edge of its first Brillouin zone. In heterojunctions of semiconductors, where the electron affinity of the atoms in each semiconductor helps to line up the bands, wavefunctions can also decay into one semiconductor; also, it is very well known that the states of the semiconductor and the metal change in Schottky interaction. "Metal-induced gap states" is the name for this kind of thing. Fermi level pinning can happen if there are a lot of surface states. This means that the Fermi level will only change slightly when the electric field changes. Because of this, the band will keep getting bent. Surface-bound species like adsorbates can cause extrinsic surface states, and electronegativity of the surface-bound species is crucial.

Photovoltaic effect

Several photocatalytic processes require semiconductors with high reactivity, long durability, and easy recovery while harnessing a considerable percentage of visible light, including the reduction of carbon dioxide and photodegradation of pollutants. Similar to photoelectrochemical water splitting, essential factors include bandwidth, position, particle size, surface characteristics, and crystal phases on exposed surfaces. High charge carrier recombination rates, low visible-light activity, and poor selectivity are the major stumbling blocks.

A viable approach to exploiting the sun's plentiful natural energy has been the photovoltaic effect in the previous decades. Excitation of electron-hole pairs and separation of e-h pairs are the two primary mechanisms that lead to the photovoltaic effect. As a result of the depolarisation ferroelectric BFO field, light-induced e-h couples were separated in 2009 by Choi et al. works on single ferroelectric-domain bulk BFO [26]. Due to its ferroelectric polarisation, an applied field can reliably alter the photovoltaic properties of BFO. Photovoltaic systems can benefit significantly from the photovoltaic effect of BFOs [26] because of their small band gaps (2.2–2.8 eV), which are suitable for practical applications. In addition to the photovoltaic and switchable ferroelectric properties of BFO, magnetoelectric properties were studied for heterostructures as well as ferroelectric memory applications.

Photocatalysis

As BFO has a narrow band gap, it is commonly used in photocatalytic activity in powder form. However, heterostructures specifically based on BFO can also be used. Typically, BFO is visible sensitive to light and interacts with common semiconductor-based photocatalysts, such as TiO₂, metal-free graphitic C₃N₄, and magnetic spinel ZnFe₂O₄ to

improve the photocatalytic efficiency under visible light [27]. By maximising the composition of BFO at different molar ratios of BFO to C₃N₄, and the photocatalytic performance is measured by degradation of Rhodamine B in an aqueous solution while being exposed to visible light, the photocatalytic efficiency in the C₃N₄/ xBFO heterostructures is 1.4 times higher than that of pure C₃N₄ and pure phase BFO [28]. Additionally, due to the aligned ferroelectric polarisation, mechanical pressing and electrical poling can boost the photocatalytic activity of BFO-based heterostructures. BFO can act as the primary photocatalyst, and mixing it with other substances can increase its photocatalytic efficacy.

1.7. Literature review

1.7.1. Synthesis of BiFeO₃ using different techniques

BiFeO₃ ceramics show Fe-rich areas near the grain border and Bi-rich selenite phases within their grains. The faster bismuth diffusion might explain these Fe-rich zones. It is essential to conceptualize this system as a coexisting kinetically stabilized phase system to prevent an unreacted phase. Chemical vapour deposition, hydrothermal and microwave hydrothermal deposition are some effective ways to manufacture different-sized and morphological samples that fall under the umbrella of soft chemistry. Throughout this way, reaction ions are evenly dispersed in the precursor solution, gel, and polymer precursor, which improves the quality of the final sample. Soft chemistry procedures often operate at very low temperatures, allowing for precise control over the stoichiometry of the material. Hydrothermal procedures have recently yielded a variety of BiFeO₃ morphologies. A mixture of alkaline conditions was added to the precursor solution by Fei al. to produce BiFeO₃ cubes as well as pills with exposed facets [29]. Sol-gel techniques were also utilized to synthesise BiFeO₃ in various sizes and with various precursors. Many different oxides need chelation, and hydroxyl is the most often used chelating agent because it retains and maintains the correct stoichiometric ratios. It is well known from the literature that reducing the grain boundary area reduces internal energy after recovery and recrystallization. Hence, different synthesis temperatures are required for materials of different sizes and shapes.

1.7.1.1. Solid-state- technique

A solid-state method is one of the most common and effective methods for preparing BFO. The solid-state synthesis method was developed mainly because of commercial need and

scholarly curiosity. Solid-state BFO synthesis has been reported in some studies up to this point. The first solid-state synthesis of BiFeO₃ was in 1960 by Filipev et al. [30]. Following this, Achenbach et al. [31] sought to manufacture pure BiFeO₃ through solid-state synthesis. Because of the less essential phases Bi₂O₃ and Bi₂Fe₄O₉, they have not been able to produce single-phase BiFeO₃ sintering conditions. By eliminating the concentrated form of BiFeO₃ that was created by utilising an excessive amount of Bi₂O₃, these issues (formation of secondary phases) were resolved. Perovskite BiFeO₃ is formed when the heart and shell are nearby. At the hypothetical conclusion of the reaction, the secondary selenite and mullite phases should disintegrate to produce a single stage of BiFeO₃. It turns out that the crystallization of mullite (Bi₂Fe₄O₉) particles coincides with the increase in temperature and the spread of Bi ions in the BFO structure. Mullite crystals are stable, and the subsequent reaction has slowed down. The BiFeO₃ and two different processes coexist in the final product.

1.7.1.2. Wet chemical methods

1.7.1.2.1. Co-precipitation method

When co-precipitation takes place, precipitates from materials that are normally soluble will be carried down under the present conditions. Generally, it is not desirable in chemical analysis, but it can also be exploited in some cases. The co-precipitating method is not suitable for gravimetric scrutiny, which involves precipitating analytes and measuring their mass to determine their concentration or purity. Due to unwanted impurities co-precipitating with the analyte and resulting in excess mass, it is not suitable for gravimetric scrutiny.

In radiochemistry, however, this method is usually the only way to separate elements when looking for trace elements. Three major steps are involved: inclusion, adsorption and occlusion. Whenever a carrier's crystal structure contains an impurity that occupies a lattice site, inclusion occurs when the impurity's ionic radius and charge values are as carrier. Adsorption is the second step, where an impurity weakly adheres to the precipitate's surface. In addition, as the crystal grows, an adsorbed impurity can become trapped inside the crystal. This is called occlusion [32].

1.7.1.2.2. Sol-gel method

Solid materials are usually produced from small precursor molecules using the sol-gel method. One of the most desired techniques for synthesizing nanostructured materials is this one. To obtain a solid material, the precursors are dissolved in a solvent, the solvent is removed by dry drying, then the material is sintering. In this method, no high processing temperature is required, making it an economical and simple procedure. Since the reactants are better mixed by this method, the samples produced by this method are more pure, homogeneous, and small in particle size. The sol-gel method utilizes chemical reactions to produce solid particles or clusters in liquid by hydrolyzing and condensation of precursor materials. Metal oxides and nitrates are usually used as precursors for the sol's preparation. Solid particles suspended in liquid are called sols. In a typical sol-gel process, the sol is formed through hydrolysis and polymerization of the precursors. Sol-cast will create a wet gel when placed in a mould. The liquid in a wet gel can be heated or removed under a supercritical condition to produce the low-density, voluminous material and porous known as xerogel/aerogel [33]. As a result of sol-gel technology, atomically mixed materials are capable of crystallizing and densifying at much lower temperatures.

1.7.1.2.3. Microwave-assisted-solvothermal/hydrothermal

In 2002, Newalkar and Komarneni synthesized mesoporous silica SBA-15, which was stable through microwave-assisted hydrothermal method at 372 K for two h utilizing a precursor Pluronic 123 copolymer and sodium silicate which is containing ethanol and hydrochloric acid [34]. They found that the microwave-assisted hydrothermal/solvothermal process is an excellent choice owing to its energy efficiency and environmental friendliness [35]. Peisong Tang and their team [36] synthesized LaFeO₃ nanoparticles through the microwave hydrothermal method at 850 W and reported pure phase formation of LaFeO₃. The as-prepared LaFeO₃ exhibits high crystalline nature and a sphere-like form, as demonstrated by XRD and SEM. According to the findings of the DRS (diffuse reflectance spectroscopy), as-prepared LaFeO₃ exhibits high light absorption with an optical absorption start of 525 nm, confirming a 2.36eV. The results of the photo electrocatalytic experiment show that the as-prepared LaFeO₃ is substantially more active in photo catalysing visible light than the industrial P25 photocatalyst. K. Chybczynska and their team [37-38] synthesized BFO micro flowers by varying microwave power from 20-60 min

at different KOH concentrations. XRD results revealed the pure phase BFO was obtained in a longer reaction time of 1hr. In the work reported in [37], BFO has composed of big flowers with a non-uniform distribution. These BFO flowers have shown weak magnetic properties. Upendra A. Joshi and team [39] synthesized BFO nanotubes through microwave method in 30 min using KOH as a mineralizer. The BFO synthesized in this work has shown excellent optical properties with a narrow band gap of 2.1 eV. It is well known from the literature that BFO is an excellent photocatalyst with magnetic recovery properties. However, it is showing poor catalytic performance compared to the other semiconductors. To improve its activity, many research groups have explored the strategies such as synthesising BFO heterostructures [40-44].

1.8. Motivation and Objectives of the present thesis work

The Motivation

- ❖ To synthesize a pure phase BiFeO₃ using conventional wet chemical techniques, the entire reaction process takes days to complete without producing impurities that don't react. Additionally, to produce pure phase BFO crystals using these methods requires a step of high-temperature calcination or sintering, which consumes a lot of energy. Therefore, the reaction time must be shortened to achieve a pure phase BFO, which will also reduce energy consumption.
- Mineralizers are still a challenge for material researchers when it comes to controlling the crystal growth of bismuth ferrite (BFO) during the solvothermal/hydrothermal process. Mineralizers may introduce metal cations into the BFO structure during the synthesis of pure phase BFO, resulting in impurities forming in the system.
- ♦ Photocatalytic applications of pristine BFO have not yet been developed due to the short separation between e- and h+ pairs formed after bandgap excitation. Therefore, a pristine BFO needs to be enhanced in terms of photocatalytic activity and performance.

The objective of the thesis work based on the research gaps are

♦ Hexamethylenetetramine (HMTA) is not reported to be used as a precipitating agent, nor is it reported that it is used as a mineralizer, but only KOH, NaOH, and LiOH are reported to be used for synthesizing the BFO. Therefore, our goal was to quickly produce a pure phase BFO using HMTA as a precipitating agent using the solvothermal method (180°C).

- Very few studies have been conducted on the rapid synthesis of BFO using a microwave-assisted solvothermal route. We, therefore, designed a one-step microwave-assisted solvothermal route to synthesize a pure phase BFO with improved multiferroic properties.
- ❖ We attempted to load various ratios of n-type Fe₂O₃ [bandgap of 1.9 eV] semiconductor onto pristine BFO [(1-x) BFO + x Fe₂O₃] where (x = 0.10, 0.20, 0.30] in order to increase the photocatalytic activity. It is anticipated that the creation of BFO heterostructures using Fe₂O₃ will increase the pristine BFO's photocatalytic activity and efficiency.
- ♦ We chose black TiO₂ as the second semiconductor to improve the photocatalytic property of pure BFO (BTO). When black TiO₂ is added to pure BFO, there are no reports of the formation of heterostructures based on BFO. So, for the first time, we tried to load different amounts (x = 0.10, 0.20, and 0.3) of black TiO₂ (with a bandgap of 1.68 eV) onto the BFO. Therefore, the overlap between the bandgaps of the two semiconducting materials will slow down the rate of charge carrier recombination in the pure BFO.

REFERENCES

- 1. Ivanov, S., 2012. Multiferroic complex metal oxides: main features of preparation, structure, and properties. In *Science and Technology of Atomic, Molecular, Condensed Matter & Biological Systems* (Vol. 2, pp. 163-238). Elsevier.
- 2. Buurma, A.J.C., Blake, G.R., Palstra, T.T.M. and Adem, U., 2016. Multiferroic materials: physics and properties. *Reference Module in Materials Science and Materials Engineering*.
- 3. Kimura, T., Goto, T., Shintani, H., Ishizaka, K., Arima, T.H. and Tokura, Y., 2003. Magnetic control of ferroelectric polarization. *nature*, 426(6962), pp.55-58.
- 4. Smolenskii, G.A. and Chupis, I.E.E., 1982. Ferro electromagnets. *Soviet Physics Uspekhi*, 25(7), p.475.
- 5. Zhang, S., 2014. Electric-Field Control of Magnetization and Electronic Transport in Ferromagnetic/Ferroelectric Heterostructures. Springer Science & Business Media.
- 6. Martin, L.W., Crane, S.P., Chu, Y.H., Holcomb, M.B., Gajek, M., Huijben, M., Yang, C.H., Balke, N. and Ramesh, R., 2008. Multiferroics and magnetoelectrics: thin films and nanostructures. *Journal of Physics: Condensed Matter*, 20(43), p.434220.
- 7. Ham, W.S., Pradipto, A.M., Yakushiji, K., Kim, K., Rhim, S.H., Nakamura, K., Shiota, Y., Kim, S. and Ono, T., 2021. Dzyaloshinskii–Moriya interaction in noncentrosymmetric superlattices. *npj Computational Materials*, 7(1), pp.1-7.
- 8. Wallyn, J., Anton, N. and Vandamme, T.F., 2019. Synthesis, principles, and properties of magnetite nanoparticles for in vivo imaging applications—A review. *Pharmaceutics*, 11(11), p.601.
- 9. Khikhlovskyi, S.V.V. and Blake, G., 2010. The renaissance of multiferroics: bismuth ferrite (BiFeO₃)-a candidate multiferroic material in nanoscience. *University of Groningen*, p.1.
- 10. Kittel, C., McEuen, P. and McEuen, P., 1996. *Introduction to solid state physics* (Vol. 8, pp. 105-130). New York: Wiley.
- 11. Tokura, Y., Seki, S. and Nagaosa, N., 2014. Multiferroics of spin origin. *Reports on Progress in Physics*, 77(7), p.076501.
- 12. Haumont, R., Kornev, I.A., Lisenkov, S., Bellaiche, L., Kreisel, J. and Dkhil, B., 2008. Phase stability and structural temperature dependence in powdered multiferroic BiFeO₃. *Physical review B*, 78(13), p.134108.

- 13. Zhou, C.R. and Liu, X.Y., 2007. Dielectric properties and relaxation of Bi₀₅Na₀₅TiO₃-BaNb₂O₆ lead-free ceramics. *Bulletin of Materials Science*, *30*(6), pp.575-578.
- 14. Ederer, C. and Spaldin, N.A., 2005. Recent progress in first-principles studies of magnetoelectric multiferroics. *Current Opinion in Solid State and Materials Science*, 9(3), pp.128-139.
- 15. Ederer, C. and Spaldin, N.A., 2005. Recent progress in first-principles studies of magnetoelectric multiferroics. *Current Opinion in Solid State and Materials Science*, 9(3), pp.128-139.
- 16. Wang, N., Luo, X., Han, L., Zhang, Z., Zhang, R., Olin, H. and Yang, Y., 2020. Structure, performance, and application of BiFeO₃ nanomaterials. *Nano-Micro Letters*, *12*(1), pp.1-23.
- 17. Tokura, Y. and Nagaosa, N., 2000. Orbital physics in transition-metal oxides. *science*, 288(5465), pp.462-468.
- 18. Gadhi, T.A., Hernández, S., Castellino, M., Chiodoni, A., Husak, T., Barrera, G., Allia, P., Russo, N. and Tagliaferro, A., 2018. Single BiFeO₃ and mixed BiFeO₃/Fe₂O₃/Bi₂Fe₄O₉ ferromagnetic photocatalysts for solar light driven water oxidation and dye pollutants degradation. *Journal of industrial and engineering chemistry*, 63, pp.437-448.
- 19. Lu, J., Qiao, L.J., Fu, P.Z. and Wu, Y.C., 2011. Phase equilibrium of Bi₂O₃–Fe₂O₃ pseudo-binary system and growth of BiFeO₃ single crystal. *Journal of crystal growth*, 318(1), pp.936-941.
- 20. Polomska, M., Kaczmarek, W. and Pająk, Z., 1974. Electric and magnetic properties of (B1– xLax) FeO₃ solid solutions. *physica status solidi* (a), 23(2), pp.567-574.
- 21. Palai, R., Katiyar, R.S., Schmid, H., Tissot, P., Clark, S.J., Robertson, J., Redfern, S.A.T. and Scott, J.F., 2007. The beta phase of multiferroic bismuth ferrite and its beta-gamma metal-insulator transition. *arXiv preprint arXiv:0705.2883*.
- 22. Zhang, R., Liu, S., Kong, F., Tong, J., Ruan, L., Duan, Q., Zhou, J. and Zhang, X., 2020. α-Fe₂O₃/BiFeO₃ composites as visible-active photocatalysts and their optical response mechanism. *Journal of Physics and Chemistry of Solids*, *141*, p.109329.
- 23. Tokura, Y. and Nagaosa, N., 2000. Orbital physics in transition-metal oxides. *science*, 288(5465), pp.462-468.
- 24. Yin, L. and Mi, W., 2020. Progress in BiFeO₃-based heterostructures: materials, properties and applications. *Nanoscale*, *12*(2), pp.477-523.

- 25. Choi, T., Lee, S., Choi, Y.J., Kiryukhin, V. and Cheong, S.W., 2009. Switchable ferroelectric diode and photovoltaic effect in BiFeO₃. *Science*, *324*(5923), pp.63-66.
- 26. Safizade, B., Masoudpanah, S.M., Hasheminiasari, M. and Ghasemi, A., 2018. Photocatalytic activity of BiFeO₃/ZnFe₂O₄ nanocomposites under visible light irradiation. *RSC advances*, 8(13), pp.6988-6995.
- 27. Safizade, B., Masoudpanah, S.M., Hasheminiasari, M. and Ghasemi, A., 2018. Photocatalytic activity of BiFeO₃/ZnFe₂O₄ nanocomposites under visible light irradiation. *RSC advances*, 8(13), pp.6988-6995.
- 28. Fei-Fei, L. and Perona, P., 2005, June. A bayesian hierarchical model for learning natural scene categories. In 2005 IEEE Computer Society Conference on Computer Vision and Pattern Recognition (CVPR'05) (Vol. 2, pp. 524-531). IEEE.
- 29. Filipe-Santos, O., Bustamante, J., Chapgier, A., Vogt, G., de Beaucoudrey, L., Feinberg, J., Jouanguy, E., Boisson-Dupuis, S., Fieschi, C., Picard, C. and Casanova, J.L., 2006, December. Inborn errors of IL-12/23-and IFN-γ-mediated immunity: molecular, cellular, and clinical features. In *Seminars in immunology* (Vol. 18, No. 6, pp. 347-361). Academic Press.
- 30. Achenbach, T.M. and Rescorla, L.A., 2014. The Achenbach system of empirically based assessment (ASEBA) for ages 1.5 to 18 years. In *The use of psychological testing for treatment planning and outcomes assessment* (pp. 179-214). Routledge.
- 31. Shetty, M.S. and Jain, A.K., 2019. *Concrete Technology (Theory and Practice)*, 8e. S. Chand Publishing.
- 32. Hu, Y., Fei, L., Zhang, Y., Yuan, J., Wang, Y. and Gu, H., 2011. Synthesis of bismuth ferrite nanoparticles via a wet chemical route at low temperature. *Journal of Nanomaterials*, 2011.
- 33. Komarneni, S., Li, D., Newalkar, B., Katsuki, H. and Bhalla, A.S., 2002. Microwave–polyol process for Pt and Ag nanoparticles. *Langmuir*, *18*(15), pp.5959-5962.
- 34. Komarneni, S., Li, D., Newalkar, B., Katsuki, H. and Bhalla, A.S., 2002. Microwave–polyol process for Pt and Ag nanoparticles. *Langmuir*, *18*(15), pp.5959-5962.
- 35. Tang, P., Tong, Y., Chen, H., Cao, F. and Pan, G., 2013. Microwave-assisted synthesis of nanoparticulate perovskite LaFeO₃ as a high active visible-light photocatalyst. *Current Applied Physics*, *13*(2), pp.340-343.
- Ahmad, W.R.W., Mamat, M.H., Zoolfakar, A.S., Khusaimi, Z. and Rusop, M., 2016,
 December. A review on hematite α-Fe₂O₃ focusing on nanostructures, synthesis

- methods and applications. In 2016 IEEE Student Conference on Research and Development (SCOReD) (pp. 1-6). IEEE.
- 37. Tang, P., Tong, Y., Chen, H., Cao, F. and Pan, G., 2013. Microwave-assisted synthesis of nanoparticulate perovskite LaFeO₃ as a high active visible-light photocatalyst. *Current Applied Physics*, *13*(2), pp.340-343.
- 38. Joshi, U.A., Jang, J.S., Borse, P.H. and Lee, J.S., 2008. Microwave synthesis of single-crystalline perovskite BiFeO₃ nanocubes for photoelectrode and photocatalytic applications. *Applied Physics Letters*, 92(24), p.242106.
- 39. Bagvand, N., Sharifnia, S. and Karamian, E., 2018. A visible-light-active BiFeO₃/ZnS nanocomposite for photocatalytic conversion of greenhouse gases. *Korean Journal of Chemical Engineering*, 35(8), pp.1735-1740.
- 40. Volnistem, E.A., Bini, R.D., Silva, D.M., Rosso, J.M., Dias, G.S., Cotica, L.F. and Santos, I.A., 2020. Intensifying the photocatalytic degradation of methylene blue by the formation of BiFeO₃/Fe₃O₄ nanointerfaces. *Ceramics International*, 46(11), pp.18768-18777.
- 41. Flak, D., Braun, A., Mun, B.S., Döbeli, M., Graule, T. and Rekas, M., 2012. Electronic structure and surface properties of non-stoichiometric Fe₂O₃-δ (α and γ) and its application in gas sensing. *Procedia Engineering*, 47, pp.257-260.
- 42. Zheng, F., Shen, M., Guo, R., Fang, L. and Dong, W., 2011. Magnetically separable BiFeO₃ nanoparticles with a g-Fe₂O₃ parasitic phase: controlled fabrication and enhanced visible-light photocatalytic activity. *J Mater Chem*, 21, pp.18645-18652.
- 43. Gadhi, T.A., Hernández, S., Castellino, M., Chiodoni, A., Husak, T., Barrera, G., Allia, P., Russo, N. and Tagliaferro, A., 2018. Single BiFeO₃ and mixed BiFeO₃/Fe₂O₃/Bi₂Fe₄O₉ ferromagnetic photocatalysts for solar light driven water oxidation and dye pollutants degradation. *Journal of industrial and engineering chemistry*, 63, pp.437-448.
- 44. Zhang, R., Liu, S., Kong, F., Tong, J., Ruan, L., Duan, Q., Zhou, J. and Zhang, X., 2020. α-Fe₂O₃/BiFeO₃ composites as visible-active photocatalysts and their optical response mechanism. *Journal of Physics and Chemistry of Solids*, *141*, p.109329.

CHAPTER-2

Experimental and characterization techniques

2.1. Introduction

As was mentioned in a previous chapter, techniques in addition to the chemical composition and general synthesis factors have a substantial effect on the properties of materials. Recent advances in synthesis, as well as characterization methods, have made it possible to enhance the characteristics of materials. Thus, the intriguing and appealing qualities of materials will make it possible to use them in extremely sophisticated technical applications and realise one's fantasies. Applications could be found in the communications, energy, defence, entertainment, biological, and scientific fields, among many others. Materials and military manipulations have made all of these conceivable. Researchers have been working on developing and using different ways to make new materials so that they can be manipulated at the atomic level.

This chapter discussed the detailed experimental methodologies used to make multiferroic BiFeO₃ samples and their heterostructures. We also discussed the techniques used to characterize these materials. Important relationships and variables have been discussed briefly. In these studies, solvothermal, microwave-assisted-solvothermal and coprecipitation synthesis methods were used. Powder XRD, FESEM with EDS, TEM, FTIR, XPS, Raman, VSM, dielectric measurements, ferroelectric measurements and optical properties are all ways to find out about the structural, magnetic, electrical, and properties of a material.

At this point, it seems appropriate to discuss the various approaches to creating something so we can comprehend the approaches as a whole, contrast them, and determine the outcomes. Additionally, since each synthesis method has a unique impact on research outcomes, it is beneficial to describe and emphasise these methods briefly. This will assist in formulating fresh research ideas. In the following sections, the characterization techniques will also be covered in more detail, particularly in light of the current materials.

2.2. Synthesis techniques employed

2.2.1. Solvothermal method

Solvothermal synthesis is a chemical reaction in which a solvent is heated above its boiling point in a sealed vessel. This approach offers fine control over the particle size distribution and form by altering the reaction conditions. If water is used as the solvent, this process is also referred to as a hydrothermal process, and if a different solvent, such as alcohol, is referred to as a solvothermal process [1]. This process is frequently done in an autoclave, which is a sealed vessel made of steel or another sturdy alloy that can withstand the pressure that naturally builds during the reactions, as shown in the **figure. 2. 1**. The Teflon liner inside the autoclave serves as a chemically stable vessel for the reactions and protects the autoclave from corrosion.



Figure 2. 1. Photograph of hot air oven and autoclave used for solvothermal sythesis [right side].

In this thesis work, we have synthesized four sets of BFO samples through the solvothermal method utilizing metal chlorides as a starting material, ethanol as a reaction medium, and Hexamethylenetetramine (HMTA) as a precipitating agent. All samples were synthesized at 180° C for 4 hours. After solvothermal treatment, the final product was cleaned with ethanol and DI water before being dried at 80°C for 8 hours.

2.2.2. Microwave-assisted-solvothermal method

In recent years, a novel technique for making powder has emerged called the microwave-assisted hydrothermal process. Although it follows the hydrothermal technique's general principles, it differs from the conventional hydrothermal synthesis method because it uses microwave signals for heating. The microwave-assisted hydrothermal approach fully utilises the advantages of both microwaves and hydrothermal processes by combining

them. The microwave-assisted hydrothermal heating approach contrasts with the hydrothermal method in using microwaves to heat the solution instead of a simple conduction method. Despite the microwaves could penetrate through the sample and heat it simultaneously in all directions, which significantly sped up the reaction time. Compared to the traditional hydrothermal method, the microwave-assisted hydrothermal approach can quickly produce nanoparticles with a uniform particle size distribution and uniform morphology due to its reactivity, fast-heating, and uniform heating system. Therefore, the microwaves propagate equally irrespective of the material. Additionally, the microwave hydrothermal method has much potential for study and application in creating ultrafine powder. Microwave-assisted synthesis is frequently more efficient, cost-effective, and quicker than traditional hydrothermal processes.



Figure 2. 2. A schematic of the commercial microwave solvothermal synthesis system.

2.2.2.1. Factors that affect the rate of reaction in microwave system [2]

Sample volume: A review by Richard N [2] has proven that the smallest (less than one mole) volumes of material will be present in the Teflon reaction vessel, where the heating will occur the quickest and rate enhancements will be the largest.

Reactions in nonpolar solvents

The microwave oven heats diluted solutions of polar substances in nonpolar fluids by a prolonged process. This happens because the polar molecules in the solution are the only ones that can absorb the microwaves. Then, when molecules hit each other, they transfer heat energy to the nonpolar solvent. Microwave irradiation seems to speed up organic synthesis only in polar solvents. This is because microwave synthesis heats much more slowly and has shorter reaction times [2].

The point at which the solvent boils

When the solvent's boiling temperatures are up, the rate of reaction improvement goes down. This is because an alteration in the solvent affects the reaction rates of microwave and traditional reactions differently. The speed of the classical reaction increases with increasing reaction temperature. According to the results from [2], the microwave technique only accelerates reactions in low boiling solvents. But in reality, this is not the case. There are two ways to increase the reaction rate of a chemical reaction in a solvent with a higher boiling point: modifying the volume of the solvent in the microwave container or increasing the microwave power utilized in the fabrication.

Reaction vessel size: Increasing the volume of a container decreases the reaction rate. Due to the inverse relationship between pressure and volume in Teflon bottles, the rate of reaction increases as pressure is increased in Teflon bottles. Since the boiling point of liquid rises as its pressure increases, this relationship is valid.

Simple domestic microwave-assisted-solvothermal system

The single-phase BFO is produced using the microwave-assisted solvothermal technique in a domestic microwave oven by varying microwave power from 200W - 800W, and the frequency is 2.45GHz. We synthesized the BFO in powder form using two metal precursors (BiCl₃ and FeCl₃.6H₂O) and a mineralizer (KOH). After adding the metal precursors to ethanol and stirring them mechanically for an hour at equimolar concentrations (0.05M), different molar KOH was added dropwise to the metal precursor solution at constant magnetic stirring. A microwave acid digestion jar (model 4782 from Parr) with a 40-50 ml capacity was then filled with 5-10 ml of this mixture and placed in a domestic microwave oven at different MW powers and durations to get the best combination of the experimental conditions. We have optimized the KOH concentration from 6 to 12M by keeping optimal MW power (800 W) and time (3min) as constant parameters. We have also synthesized a few samples through a commercial MW system by applying maximum power and time and compared these results with the results obtained through the domestic oven.

Compared to a commercial microwave system [figure 2.2], we could quickly synthesize all BFO samples using a simple domestic microwave oven [figure 2.3]. Higher temperatures will be needed to make pure BFO under high pressure to avoid the formation of Bi and Fe-based impurity phases. It is thought that as we use more vessels, at least four are needed for a commercial microwave system to function, and the applied microwave power may not be homogeneous across all vessels. In a commercial microwave oven [model: Anton Paar Rotor 16], the sample won't acquire the provided power immediately;

instead, it will take some time, and the pressure required for BFO creation in this oven is minimal. The sample in a domestic microwave oven, however, will start to receive the entire amount of applied power as soon as the appliance is turned on.

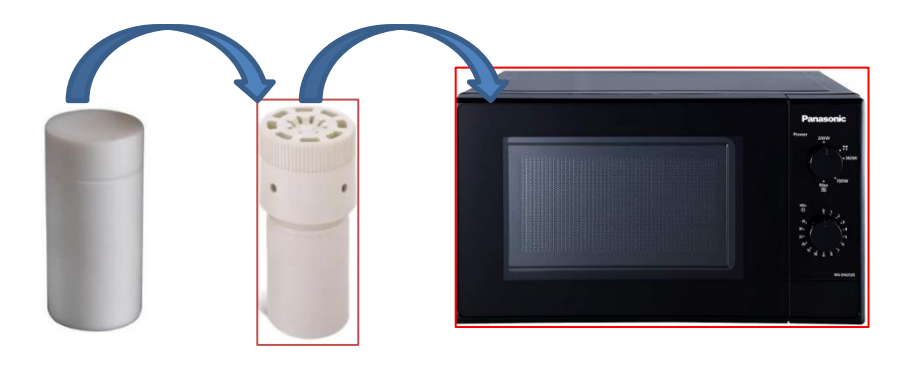


Figure 2. 3. A photograph of the domestic microwave oven system utilized in the present thesis work.

2.2.3. Co-Precipitation method

Within the co-precipitation method, precipitates of substances that are typically soluble under specific conditions will be transported downward. It is a significant problem during sample preparation because carbonate-based chemistry has a slower rate of reaction, longer retention times, and the potential to release CO₂. However, under certain circumstances, it can be helpful because carbonate reagents are relatively simple to handle and are available in large quantities, and the best results are obtained under lower pH conditions. The quantitative approach, which involves precipitating the solutes and weighing them to determine their concentration or level of purification, doesn't benefit from the co-precipitation method. This is due to the possibility of introducing impurities and co-precipitating with the analyte to produce excess mass [3]. For ferrites, this process relies on creating source powder aqueous solutions within concentrations required for the compositions. We synthesized all BFO-based heterostructures (BFO+Fe₂O₃ and BFO+black TiO₂) using this method, and we dried all samples in the microwave for 3 to 5 minutes at 350W.

2.2.4. Pellet Preparation for electrical measurements

Pellets were made utilizing a few simple but meticulous techniques for electrical measurements. Polyvinyl alcohol was added to the ultrafine particles, which were then crushed into a fine powder using a pestle and mortar for 60 minutes. PVA (polyvinyl

alcohol) was employed as a binder, and then a pellet with the shape of a circular disc was formed by pressing a powder mixture with a hydraulic press at a pressure of 5 tonnes for roughly 5 minutes. The pellet is then sintered for six hours at 500°C. We have calculated the densities of prepared pellets using a simple method, and the density of sintered BFO pellets was discovered to be within 85%–90% of the predicted value.

2.3. Material Characterization

2.3.1. Physical and Structural Characterization

Materials' physical characteristics include electrical, magnetic, optical, and other characteristics. An understanding of these features is necessary for reasonable and efficient formulation procedures. Therefore, we have unique experimental approaches that reveal and ensure the correct identification of chemicals we can use to examine these qualities. In the following review, a few analytical methods using particular instrument types have been discussed.

2.3.1.1. X-ray powder diffraction (XRD)

As a result of the discovery of X-rays by W. C. Roentgen in 1895, a wealth of new medicinal and technological uses was made feasible (Roentgen, 1895). For example, Laue, Friedrich, and Knipping's discovery of X-ray diffraction (XRD) by crystals in 1912 opened up new avenues for studying crystalline materials. Materials science and engineering have significantly benefited from developing these approaches since they were first introduced.

X-rays are produced when high-speed, high-kinetic-energy charged particles rapidly decelerate near their target. The electrons usually are accelerated to create X-rays. Two metal electrodes generate X-ray radiation in an X-ray tube by conducting electrons. Due to the enormous potential difference that can approach hundreds or thousands of volts, the movement of electrons toward the target or anode is extremely high. Radiation can be seen in all directions from where X-rays are generated [4].

The structure, crystallite size, lattice parameters, phase identification, and purity of our powder samples can all be studied using the X-ray powder diffraction (XRD) technique. In this study, we used powder XRD with a PANanalytic XPert-Pro diffractometer equipped with CuK radiation (1.5406) between $2\theta^o$ =10-80 in 0.002° steps.



Figure 2. 4. Powder X-ray diffractometer's photograph.

2.3.1.2. Field Emission Scanning Electron Microscopy (FESEM)

Various signals are generated when a solid material is irradiated with elevated electrons, resulting in experiments using this method. Analyzing the signals produced by the electron-sample contact allows one to determine the chemical composition, external shape or topography, orientation, and crystal structure of a sample. In addition, a high vacuum is required for this instrument to function. The SEM's intensification or clarity in resolving the material's surface could be one of its important qualities and essential elements. This device measures the magnification power by how much the specimen shows up on the monitor compared to the total area being scanned.

The various signals caused by decelerated electrons just at the interaction between electron-samples could be explained by various types of electrons produced after the collision. Thus, an image is created by these electrons. The two most popular ones are the secondary electron image (SEI) and backscattered electron image (BEI). In addition to providing a high-resolution image of the specimen surface, the SEI is primarily used to examine its topology and morphology. On either hand, the BEI's brightness depends on the sample's atomic number and is commonly used to highlight differences in composition throughout multiphase samples. Furthermore, all SEM pictures are inherently white and black,

although they may later be given artificial colours for aesthetic purposes or to facilitate interpretation [5].



Figure 2. 5. Photograph of FESEM with EDAX.

2.3.1.2.1. Energy Dispersive X-ray Spectroscopy (EDAX)

We may need to use the EDS approach if we are worried about the elemental composition of our specimens. It relies on a specimen's interaction and an X-ray excitation source. Its electromagnetic spectrum has a distinctive set of peaks due to the peculiarity of the structure of the atom. So, when the electron beam bombards the specimen, electrons are emitted from the particles that comprise the sample's surface. As a consequence of the emitted electrons, a free space is created; however, this space is quickly filled with greater energy electrons. However, when higher energy level electrons enter these empty spaces, an X-ray signature is released; as a result, the material's constituent element under inquiry can be identified by the energy of the X-rays. X-ray sensors using EDAX analyze the ratio between emitted X-rays and their energies to determine a substance's composition [5].

2.3.1.3. Fourier Transform Infrared Spectroscopy (FTIR)

Another analytical method for identifying specific organic compounds is FTIR spectroscopy. Using this analytical tool, we determine sample absorption as just a function of wavenumber. This infrared frequency band absorption indicated the existence of specific molecular structures and parts. In other words, by employing this approach, we can

determine the chemical bond types present in the material under study. We could also detect unidentified materials using the frequency modes. In other words, chemical bonds will contract, expand, and bend when the material is subjected to IR source light. Therefore, regardless of the validity of the molecule's structure, a functional group will absorb this radiation at a particular frequency. Therefore, using the modes of a molecule with a single frequency vibrational configuration, one can determine the material's constituent elements and chemical bonding configuration. Because a particular molecule has a different IR spectrograph that can reveal its individuality, the reverse process is utilised [6]. Additionally, this method is employed to find cation distribution, chemical process completion, layered structure distortion and vibration modes. FT-IR spectroscopy measurements are also carried out utilising a transmittance technique with KBr pellets as an IR window within the 400–4500 cm⁻¹ wavelength range.



Figure 2. 6. Photograph of Fourier Transform Infrared Spectroscope (FTIR).

2.3.1.4. Raman Spectroscopy

In 1928, Sir Chandrashekhar Venkata Raman discovered Raman spectroscopy. The Raman effect happens when it makes contact with a molecule; this causes the atoms to vibrate uniformly and changes the wavelength of the light. If the scattered radiation frequency increases after interacting with the sample, it is referred to as stokes; if it reduces, it is referred to as anti-stokes. Since stokes are stronger than anti-stokes, the Raman spectrum usually measures stokes like a Raman shift. Inelastic scattering of monochromatic light is used to analyse the matter in Raman spectroscopy. One of the most widely used instruments for studying current physics, biology, microscopy and geochemistry. Photon absorption or emission triggers transitions between quantum levels of atoms or molecules, as opposed to

the usual absorption or emission spectroscopy investigations (IR, visible, UV). Its sensitivity is less than that of emission or absorption spectroscopy, but it offers several advantages, including the ability to use an incident wavelength that is not absorbed by the surrounding media, the ability to precisely focus the light on micron-sized spots, and the use of symmetry-based selection rules. The transmission of monochromatic light on a transparent material is virtually completely unaffected. The material scatters a tiny amount of light in all directions, but this scattering is preferentially in the direction of travel ahead. Some of the light dispersed in this way comprises photons of a lower frequency than the incident frequency, such as the frequency of a chemical transition (usually rotational or vibrational) [7]. Raman spectroscopy can be used to see a material's molecular structure. The pure phase formation of the BFO will be confirmed by Raman spectroscopy. The current study examined the functional groups in BFO samples synthesized using solvothermal and microwave-assisted solvothermal techniques.



Figure 2. 7. Raman spectroscope's photograph.

2.3.1.5. Transmission Electron Microscopy (TEM)

Ernst Ruska, a German scientist, created the first electron microscope in 1932 and was awarded the Nobel Prize for his innovation in 1986. Because electrons have a wavelike quality, he thought he could handle them like light waves. Electron trajectories may be affected by magnetic fields, which, like optical lenses, might concentrate them. To test these theories, he set out to build the electron microscope. Since electron waves are shorter than regular light waves, Ruska reasoned that an electron microscope would be much more powerful than an optical microscope and could see many smaller structures. The first

primitive electron microscope was capable of a 400-fold magnification. The construction of a functional, 10 nm-resolution electron microscope was discovered in 1938. Even though current electron microscopes can magnify an item 2 million times, they are still based on Ruska's prototype and the relation between wavelength and magnification.

An electron beam of a high voltage produces an image in a TEM. TEM electrons pass through the vacuum tube of the microscope as they are released from an electron source. In contrast to optical microscopy, which focuses light through a glass lens, TEMs use electromagnetic lenses to concentrate electrons into a narrow beam. After passing through the extremely thin material, this beam's electrons scatter or strike a fluorescent screen just at the microscope's base. Each component of the specimen is depicted according to its density in various tones on display. An image taken with a camera [8] can then be examined or studied in the TEM. For various reasons, the electron microscope has become a standard tool at many research facilities. For example, it's used by scientists to investigate biological materials (such as germs and cells), numerous significant compounds, medical biopsy samples, metals and crystalline structures, as well as the features of diverse surfaces. Therefore, we have used the TEM characterization technique to study the nanostructures of BFO micro flowers synthesized through the microwave method.



Figure 2. 8. Transmission Electron Microscope (TEM).

2.3.1.6. X-ray photoelectron microscope (XPS)

The photoelectric effect is used by the surface-sensitive quantitative spectroscopic technique known as XPS to identify the elements present in a material or on its surface, as well as their density of the electronic states, general electronic structure and chemical state in the material. An effective measurement technique is XPS because it identifies the elements present and the other elements to which they are bonded. The technique can be used to line profile, depth profile, and elemental composition over the surface in conjunction with ion-beam etching. The states of the materials are commonly examined before or after being subjected to heat, scraping, UV radiation, reactive gases, cleaving, or during the implantation of an ion [9].

All elements can be easily detected by XPS using laboratory X-ray beams, except helium and hydrogen. Although parts per million (ppm) can be obtained with lengthy collecting times and concentrations over the surface top, the detection limit will be in the ppm (ppt) range. Therefore, in our work, we have utilized XPS analysis to study oxidation states and binding energies of the core level spectra of BiFeO₃ constituent elements.

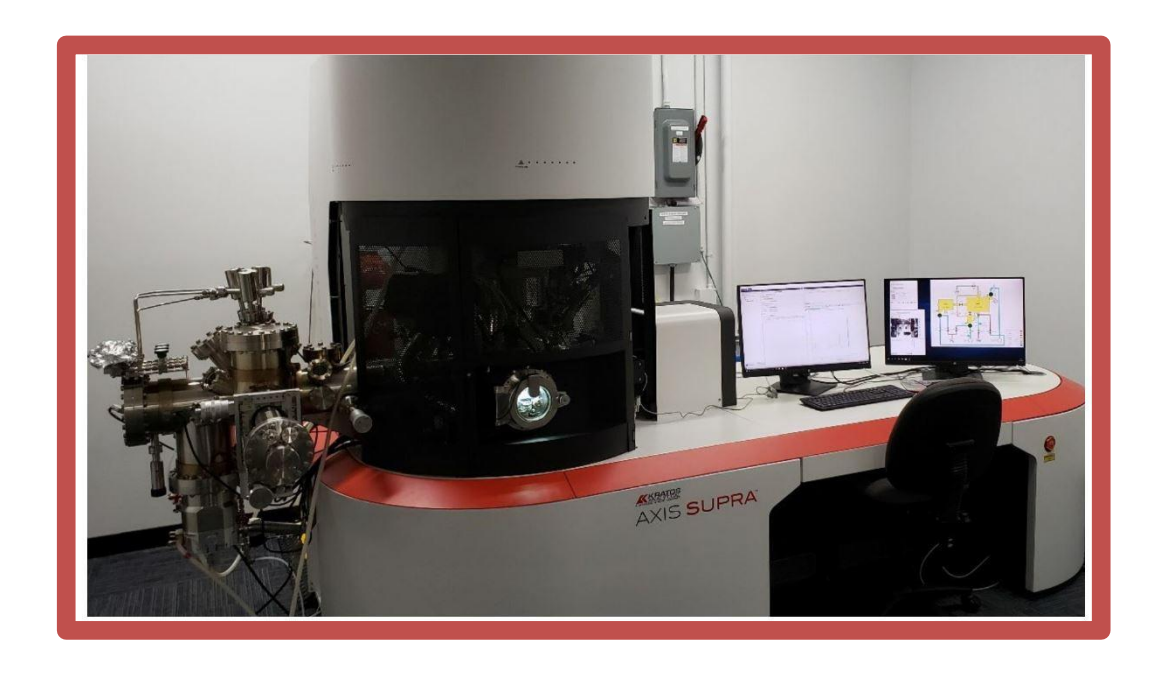


Figure 2. 9. X-ray photoelectron microscope (XPS).

2.3.1.7. UV-Vis Spectrometer

UV light (with wavelengths ranging from 200 to 400 nanometres) is used in molecular absorption spectroscopy to collect data on a sample. UV radiation absorption causes

electrons in the ground state to rise in energy. $E = h\vartheta$ is the energy difference between the system's ground state and the system's higher energy states, which is proportional to the amount of UV energy absorbed. Moving from the highest molecular orbital to the lowest molecular orbital is the most common way of accomplishing this task. This type of electron transfer may take place in organic and inorganic molecules, transitions in which charge is transferred from ligand to metal or vice versa. This absorption spectroscopy uses electromagnetic radiation ranging from 190 to 800 nm and ultraviolet and visible wavelengths. Since the absorption of UV or visible radiation by molecules results in an electronic energy level shift, it is also known as spectroscopy based on the electronic energy levels of molecules.



Figure 2. 10. Photograph of UV-Visible spectroscope.

The Beer-Lambert rule, which states that the rate at which radiation intensity decreases as the thickness of an absorbent is proportional to incident radiation and the concentration of the solution, is followed in UV spectroscopy [10-12].

One way to state the Beer-Lambert law is as follows:

$$A = log \frac{I_0}{I} = \varepsilon c L$$

Where A denotes absorbance, I_0 represents the amount of light entering the sample, I indicate the amount of light leaving the sample, c is the solute's molar concentration, L is the sample cell's length, and ε is its molar absorptivity.

Tauc Plot

The optical band gap of semiconductors and amorphous can be calculated from the Tauc relation. A Tauc plot shows photon energy $(h\theta)$ on the X-axis and absorption coefficient $(\alpha h\theta)^n$ on the Y- axis. This linear region's abscissa extrapolation yields the material's

optical bandgap energy. This characterization has been used to study all the prepared samples' absorption properties in visible light and band energy gap [13-14].

Depending on transition, we have to consider n values

directly permitted transitions, n = 1/2

direct forbidden transitions, n = 3/2

permitted indirect transitions, n = 2

indirect prohibited transitions, n = 3

2.3.2. Electrical properties

2.3.2.1. Dielectric properties

Several types of polarizations can occur when a dielectric material is exposed to an external electric field [15]:

- Electric polarization
- ii. Atomic polarization
- iii. Space charge polarization
- iv. Dipolar polarization

Materials have electronic polarisation near optical frequency (10^{15} Hz). Electronic polarisation in the substances leads to ionic polarisation at frequencies around 10^{13} Hz. While space charge polarisation only contributes below 10^2 Hz, orientation polarisation does so in the frequency range of 10^6 to 10^{10} Hz. The orientation polarization and the space charge polarisation are affected by temperature but not ionic or electronic polarization. Dipole moment rises at elevated temperatures due to the mobility of ions and crystal flaws. These four polarizations make up the total polarization.

Dielectric constant

Dielectric property analysis is a helpful tool for determining how conduction mechanisms work. An increase in charge carriers leads to an increase in ionic conductivity, indicating a material's ability to store charge through its dielectric property. A broad frequency dielectric relaxation spectroscopy can be used to analyse the relaxation of dipoles. A material's improved ionic conductivity and ionic dissociation are made possible by an enhanced dielectric constant.

The complex dielectric permittivity is indicated by $\varepsilon^* = \varepsilon' - i\varepsilon''$, ε' (stored energy) and ε'' (loss of energy), which represent the real and imaginary components of the permittivity, respectively. To determine the dielectric constant, we will use the equation below:

$$\varepsilon = \frac{cd}{\varepsilon A}$$

C stands for capacitance (F), d for pellet thickness (cm), and A for the area (cm²). The permittivity depends on the alternating voltage field frequency, material flaws, temperature, chemical composition and pressure.

Dielectric loss tangent (tan δ)

Dielectric materials absorb electrical energy from an AC signal and release it as heat once the signal is applied. This happens because dielectrics are insulators. The term "dielectric loss" refers to dissipation. The resonance phenomenon occurs when the range of the applied frequency coincides with the time to relax. Therefore, the current drives the voltage by a factor of $(90-\delta)$, where δ is referred to as loss angle, $\tan \delta$ is the electrical loss caused by resonance and therefore is referred to as tangent loss, and the loss tangent can be written as

$$\tan \delta = \frac{\varepsilon''}{\varepsilon'}$$

The imaginary and real parts of permittivity are denoted by ε'' and ε' , respectively. One of the benefits of $tan\delta$ is that this does not depend on the sample 's geometry. In other words, if the sample's geometry is unknown, as it would be in the case of an electrolytic capacitor or a p-n junction where it would be impossible to determine ε'' and ε' separately, $\tan \delta$ would be the only distinctive feature that could be reliably obtained [16].



Figure 2. 10. Photograph of Dielectric property measurement system.

2.3.2.2. Ferroelectric properties

In ferroelectric materials, without external electric fields, ferroelectrics change polarization. Crystals with spontaneous polarisation and dielectric changes have ferroelectricity. Electric fields switch grain domain orientation. Applying an electric field at a specified frequency and measuring polarisation creates an electric hysteresis loop. Remanent polarisation (P_r), saturation polarisation (P_s), and coercive electric field (E_c) parameters were extracted from the hysteresis loop and provided details about the ferroelectric domain's boundaries, orientation, switching, and other characteristics [17]. In the present study, we have measured the ferroelectric properties of the samples on circular pellets (12mm diameter and 1mm thickness). The P-E loops were measured using an advanced FE test system from the aixACCT, GmbHwhich is made in Germany.



Figure 2. 11. Photograph of Ferroelectric test system.

2.3.3. Magnetic properties

A vibrating sample magnetometer (VSM) uses a magnetic field and temperature to measure magnetism. Magnetism and crystal orientation are all measured. Faraday's law states that flux changes cause emf. The local magnetic flux modifies when a magnetic material vibrates in an even magnetic field. Pickup coils can pick up vibrations. Signal intensity is affected by frequency, vibration and magnetism. Using differential reference coils and amplifiers with the same amplitude and frequency will allow the last two terms to be removed. One can determine a magnet's curie temperature, magnetic force and maximum energy product by using the VSM to analyse basic magnetic properties like the hysteresis

loop, thermal magnetic curve, magnetization curve, demagnetization curve, etc. Piezoelectric sine wave vibrations are used to move samples in vertical tubes. The magnetic field does not impact the voltage induced in the pickup coil. Measure the induced voltage with a lock-in amplifier and a piezoelectric reference signal. The dipole field of a dimple can be converted into an AC electrical signal by measuring a small magnetic sample in the field of an external electromagnet. The magnetic properties of synthesized BFO samples were examined using VSM in the current thesis to study their magnetic properties at room temperature [18].



Figure 2. 12. Photograph of vibrating sample magnetometer.

REFERENCES

- 1. Nair, G.B., Swart, H.C. and Dhoble, S.J., 2020. A review on the advancements in phosphor-converted light emitting diodes (pc-LEDs): Phosphor synthesis, device fabrication and characterization. *Progress in Materials Science*, *109*, p.100622.
- 2. Gedye, R.N., Smith, F.E. and Westaway, K.C., 1988. The rapid synthesis of organic compounds in microwave ovens. *Canadian Journal of Chemistry*, 66(1), pp.17-26.
- 3. Ashik, U.P.M., Kudo, S. and Hayashi, J.I., 2018. An overview of metal oxide nanostructures. *Synthesis of Inorganic Nanomaterials*, pp.19-57.
- 4. Nasrazadani, S. and Hassani, S., 2016. Modern analytical techniques in failure analysis of aerospace, chemical, and oil and gas industries. *Handbook of Materials Failure Analysis with Case Studies from the Oil and Gas Industry*, pp.39-54.
- 5. El-Eskandarany, M.S., 2020. Characterizations of mechanically alloyed powders. *Mechanical Alloying*, pp.13-18.
- 6. Shameer, P.M. and Nishath, P.M., 2019. Exploration and enhancement on fuel stability of biodiesel: A step forward in the track of global commercialization. In *Advanced biofuels* (pp. 181-213). Woodhead Publishing.
- 7. Mulvaney, S.P. and Keating, C.D., 2000. Raman spectroscopy. *Analytical Chemistry*, 72(12), pp.145-158.
- 8. Rostamabadi, H., Falsafi, S.R. and Jafari, S.M., 2020. Transmission electron microscopy (TEM) of nanoencapsulated food ingredients. In *Characterization of nanoencapsulated food ingredients* (pp. 53-82). Academic Press.
- 9. Mather, R.R., 2009. Surface modification of textiles by plasma treatments. In *Surface modification of textiles* (pp. 296-317). Woodhead Publishing.
- 10. Tauc, J., Grigorovici, R. and Vancu, A., 1966. Optical properties and electronic structure of amorphous germanium. *physica status solidi* (*b*), *15*(2), pp.627-637.
- 11. Macfarlane, G.G. and Roberts, V., 1955. Infrared absorption of germanium near the lattice edge. *Physical Review*, 97(6), p.1714.
- 12. MacFarlane, 2., McLean, T.P., Quarrington, J.E. and Roberts, V., 1958. Fine structure in the absorption-edge spectrum of Si. *Physical Review*, 111(5), p.1245.
- 13. Davis, E.A. and Mott, N., 1970. Conduction in non-crystalline systems V. Conductivity, optical absorption and photoconductivity in amorphous semiconductors. *Philosophical magazine*, 22(179), pp.0903-0922.

- 14. Zanatta, A.R., 2019. Revisiting the optical bandgap of semiconductors and the proposal of a unified methodology to its determination. *Scientific reports*, 9(1), pp.1-12.
- 15. Henisch, H.K., 1984. Dielectric relaxation in solids: By AK Jonscher. Chelsea Dielectrics Press Ltd., 33 Lynwood Road, London W5 1JQ (1983), 400 pp. Price: \$56.00 ppd.
- 16. Shepherd, P., Mallick, K.K. and Green, R.J., 2007. Magnetic and structural properties of M-type barium hexaferrite prepared by co-precipitation. *Journal of magnetism and magnetic materials*, 311(2), pp.683-692.
- 17. Valasek, J., 1921. Piezo-electric and allied phenomena in Rochelle salt. *Physical review*, 17(4), p.475.
- 18. Leslie-Pelecky, D.L. and Rieke, R.D., 1996. Magnetic properties of nanostructured materials. *Chemistry of materials*, 8(8), pp.1770-1783.

Chapter-3

Synthesis and Characterization of Bismuth ferrite (BiFeO₃) synthesized by a solvothermal process using Hexamethylenetetramine (HMTA) as precipitating agent.

Objectives

- ❖ The present work aims to develop pure phase BiFeO₃ using strong organic Hexamethylenetetramine (HMTA) as a precipitating agent.
- ❖ HMTA will promote the high dissolution rate of precursor solutions, fast crystallization growth of BFO particles, and high denser BFO nanoparticles
- ❖ The novelty of the current approach is that, to date, only KOH, NaOH and LiOH were used as a mineralizer to prepare pure phase BFO, no works reported a synthesis of pure phase BFO using Hexamethylenetetramine (HMTA) as a precipitating agent. Hence, we aimed to produce a pure phase BFO using HMTA as a precipitating agent through the solvothermal method in a short reaction time at a low temperature (180°C).

3.1. Introduction

Multiferroic compounds for spintronics, data storage, and multi-state-memories have received a lot of interest in recent decades [1-3]. ABO₃ perovskites are multiferroic. BiFeO₃, RECrO₃, and REMnO₃ can be used as scaffolds [4]. BFO is one of the most studied multiferroic materials at room temperature due to its ferroelectric and anti-ferromagnetic properties [5-6]. BFO has a rhombohedral R_{3C} structure [7]. When oxygen partial pressure and temperature are not carefully controlled during synthesis, many secondary phases of Fe and Bi can form [8]. Since BFO's discovery in the 1960s, impurity phase formations, high leakage currents, poor ferroelectric properties with limited spontaneous polarisation, low resistivities, high defect densities, and inhomogeneity of magnetic spin structure have hindered its practical applications. Obtaining phase pure BFO requires a synthesis technique/process that allows scientists to overcome limitations and achieve BFO with

improved multiferroic properties. Microemulsion, sonochemical, sol-gel, solution combustion, soft chemical route, hydrothermal, and co-precipitation synthesis have all been used to produce pure phase BFO. Most synthesis methods require calcination above 400°C, where BFO is unstable.

The solvothermal synthesis strategy is based on chemical reactions in a nonaqueous solution as opposed to modern synthesis methods, which increases the reactivity and solubility of the reactants. This method entails carrying out chemical reactions in a closed container while raising autogenous pressures brought on by heat to raise solvent temperatures to levels near or beyond their boiling points [16–17]. Solvothermal approaches are straightforward, non-toxic chemical solution processes that may regulate crystallinity, size, and shape without using post-annealing processes like calcination [18-19]. Specific experimental factors, such as reaction duration, reaction temperature, surfactant, solvent type, and reductant type, must be tuned to change the properties of multiferroic BFO. The solvothermal process has the potential to be scaled up and uses an autoclave with a PTFE-coated reactor [20].

Every solvothermal system's reaction medium has a substantial impact overall. Particularly in supercritical circumstances, the solvents used in the solvothermal process have specific characteristics. In the case of a chemical reaction, the equilibrium and kinetics directly affect the interaction of the solvent with the intermediates, products, and reactants. By interacting with produced particles, the solvent used in the solvothermal method can change the structure of the material. Solvents may impact micelle structures in reaction media when surfactants are present. Additionally, in addition to serving as a reaction media, organic solvents can dissolve reactants to form complexes called solvent-reactant mixtures, which alter the pace of chemical reactions. Faster inorganic material production is better suited to solvents with high loss tangent and boiling points [21–22]. According to the literature, mineralizers are crucial for controlling processes including dissolution, nucleation, and crystallisation generated by pressure and temperature. It is still difficult for material researchers to control the crystal formation of bismuth ferrite (BFO) under the solvothermal/hydrothermal method. A hydrothermal approach was used by Mirabbos hojamberdiev et al. [23] to investigate the influence of alkaline mineralizers (KOH, NaOH, and LiOH) on the crystallisation of BFO. On the synthesis of BFO utilising KOH, NaOH, KNO₃, and LiOH as a mineralizer, there are numerous papers available [24,25,26]. Although hydrothermal or solvothermal synthesis appears to be a successful method for producing BFOs with various morphologies, using mineralizers during the synthesis of pure phase BFO may cause the introduction of metal cations from the mineralizer into the BFO structure, which results in the formation of impure phases. Therefore, to achieve ultrapure BFO, extra purification procedures are also required.

In this work, a method for producing pure phase BFO with improved multiferroic characteristics without using mineralizers is being developed. A powerful organic HMTA is used as the precipitation agent in a solvothermal reaction to produce pure phase BFO. This innovative synthesis method completely eliminates the possibility of introducing additional metal cations into the BiFeO₃ structure. Additionally, no reports of BFO being synthesised with HMTA acting as a precipitation agent. We attempted to create a pure phase BFO for the first time utilising HMTA and the benefits of the solvothermal method within the reaction period of 4 hours at low temperature (180°C). We looked at how HMTA concentrations affected the morphological, magnetic, dielectric, ferroelectric, and optical characteristics of BFO produced using the solvothermal method.

3.2. Experimental Section

3.2.1. Materials used in the synthesis

BiCl₃ (Bismuth Chloride, purity 98%), FeCl₃.6H₂O (Iron Chloride, purity 98%), Hexamethylenetetramine (HMTA, purity 98%), double distilled water (DDW), and ethanol (purity 99%) serve as the reaction medium in this synthesis method. These chemical agents were bought from the SRL firm in India on the open market.

3.2.2. Synthesis of BFO by Solvothermal technique

The solvothermal method is used to synthesize pure phase BFO in a hot air oven at 180oC for four hours. The metal precursors bismuth chloride (BiCl₃), iron chloride hexahedrite, and hexamethylenetetramine (HMTA) were used to create a powdered form of bismuth ferrite (BFO). An equimolar (0.1M) solution of BiCl₃ and FeCl₃.6H₂O was stirred magnetically for two hours in 50 ml of ethanol. We have tweaked the HMTA concentrations to understand better how they affect BFO phase development and other features. We created four sets of BFO samples for the optimization investigation by dropwise adding 0.5, 2, 4, and 6M) HMTA solutions to the bismuth chloride and iron chloride mixed solution, stirring for an hour. This liquid underwent an hour of magnetic stirring before being put into a PTFE cup and heated for four hours at 180°C in a regular hot air oven. After the solvothermal treatment, the final product was obtained, washed

several times in double-distilled water, and dried at 100°C for four hours. All characterizations use the synthetic BFO powder.

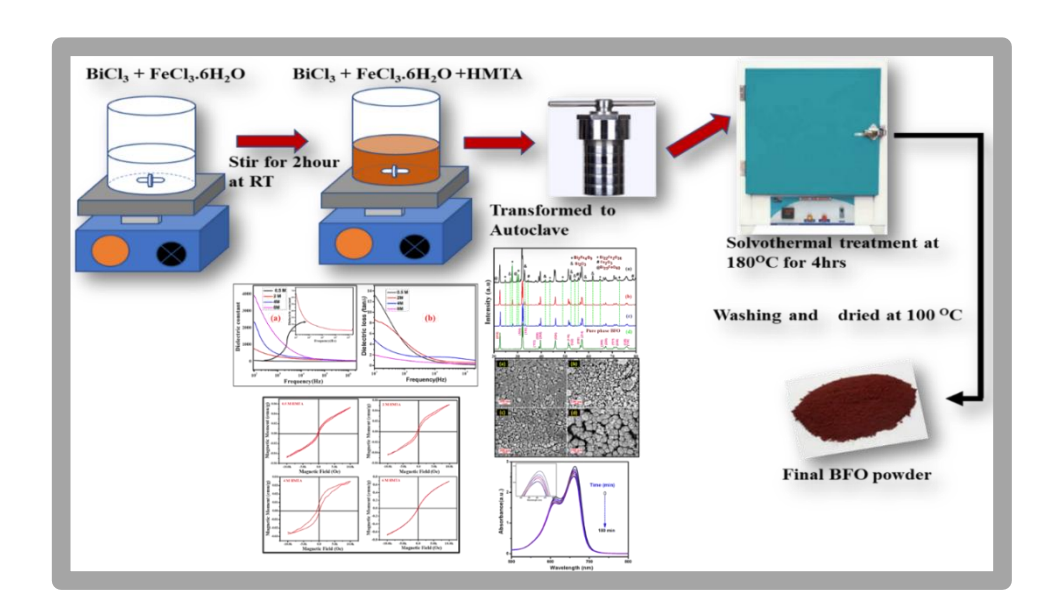


Figure 3.1. Synthesis procedure for BFO particles by solvothermal method at various HMTA concentrations (0.5, 2, 4 and 6M) at 180° C for 4hrs.

Pellet Preparation for electrical measurements

Pellets were made utilising a few straightforward but meticulous techniques for electrical experiments. Polyvinyl alcohol was added to the ultrafine particles, which were then crushed for 60 minutes. PVA was employed as a binder, and then a pellet with the shape of a circular disc was formed by pressing a powder mixture with a hydraulic press at a pressure of 5 tonnes for roughly 5 minutes. The pellet is then sintered for six hours at 500°C. Ceramics were characterized electrically using a simple approach for determining their densities. The sintered BFO pellets' measured density was within 85%–90% of the predicted value.

3.3. Characterization Techniques utilized

The structural formation of pure phase Bismuth ferrite (BFO), synthesised by the solvothermal technique, was studied using an X-ray diffraction spectrometer (XRD; PANalytical, X'Pert Powder Diffractometer employing CuK radiation, = 1.541, where 2 = 20-80 degrees). The unit cell characteristics of the BFO particles were discovered using the Rietveld refinement study (Model: Xpert high score plus version 4.9 software). To examine the morphology of the as-produced BFO, Field emission scanning electron microscopy

(FE-SEM, Model: Carl Zeiss Smart Sem) was used. Using a vibrating sample magnetometer and a dielectric-spectrometer (Novocontrol GmBH), the room temperature dielectric and magnetic characteristics were assessed (VSM, Model: LakeShore). The ferroelectric characteristics of BFO material at room temperature have been researched using the ferroelectric analyser (Model: Trek Model 609B). BFO's optical characteristics were examined using a UV-vis-NIR absorbance spectrometer (Model: Agilent Technologies Cary Series Spectrometer).

3.4. Results and Discussions

3.4.1. X-ray diffraction analysis of BFO Powders

To determine the structural formation of BFO particles produced by HMTA using the solvothermal technique at 180°C for 4 hours, powder samples are subjected to X-ray diffractometry (XRD). The XRD patterns of BFO particles created at four distinct HMTA solution concentrations (0.5, 2, 4, and 6M) are shown in **figure 3.2**. Bi₂Fe₄O₉ (ICSD:98-018-6440), Bi₂O₃ (ICSD: 98-001-5752), Bi₂₂FeO₄₀ (ICSD: 98-019-4664), Bi₂₂Fe₂O₃₆ (ICSD:98-024-8805) and Fe₂O₃ (ICSD:98-006-4599 are among the impurity phases we have found at 0.5M HMTA concentration, along with the considerable production of BFO.

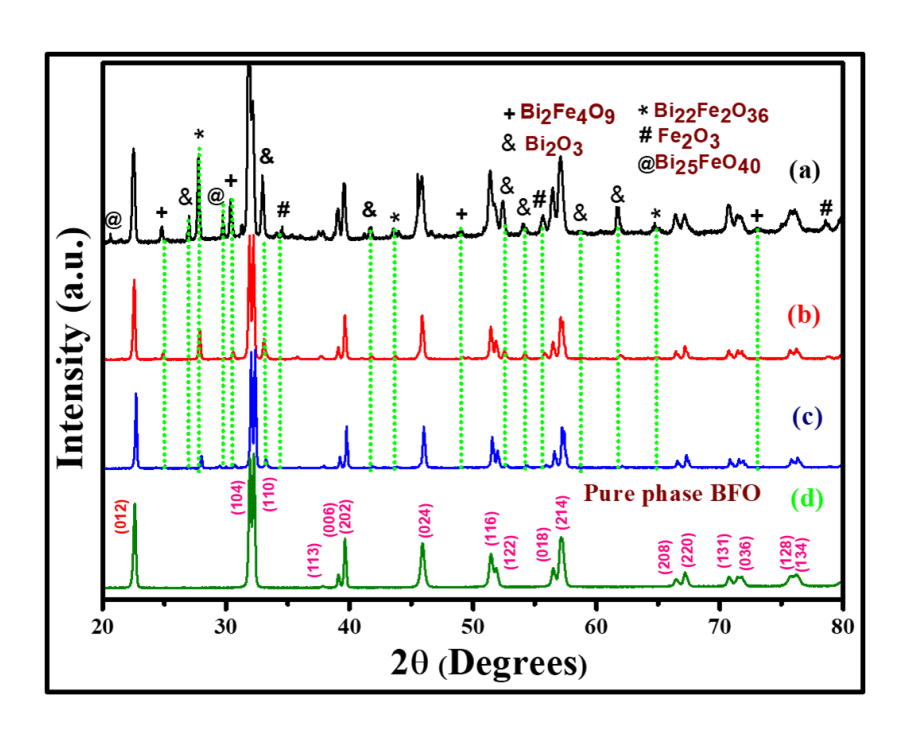


Figure 3. 2. XRD patterns of BFO particles synthesized by the solvothermal method at various HMTA concentrations a) 0.5M, b) 2M, C) 4M, d) 6M at 180°c for 4hrs.

Because the precursors did not dissolve appropriately at low HMTA concentrations, some unreacted bismuth and iron phases are present in the sample, as shown in **figure 3.2(a)**. This reduces the yield of the pure form of BFO.

The impurity peaks corresponding to the Bi₂Fe₄O₉, Bi₂O₃, and Bi₂₂Fe₂O₃₆ phases did not change as HMTA concentration increased from 0.5 to 2M, but the Fe₂O₃ and Bi₂₂FeO₄₀ impurity peaks did [**figure 3.2(b)**]. This shows that the bismuth and iron-based impurity peaks changed into the BFO phase as the HMTA concentration was raised. The number and intensities of all the impurity peaks were significantly reduced in the second sample by increasing the HMTA concentration from 2 to 4M, and only two impurity phases (Bi₂O₃ and Bi₂₂Fe₂O₃₆) remained alongside BFO phases [**figure 3.1(d)**], indicating that all the unreacted remnants from impure phases are converting to pure BFO phases. It is a sign that the high concentration of HMTA greatly influences the unreacted phases' ability to dissolve. To obtain pure phase BFO, we increased the HMTA concentration from 4M to 6M. All of the XRD peaks from the sample made with 6M HMTA are well-indexed with the rhombohedral perovskite pure phase BFO in the R_{3c} space group, devoid of any impurity phases, as shown in **figure 3.2(d)**.

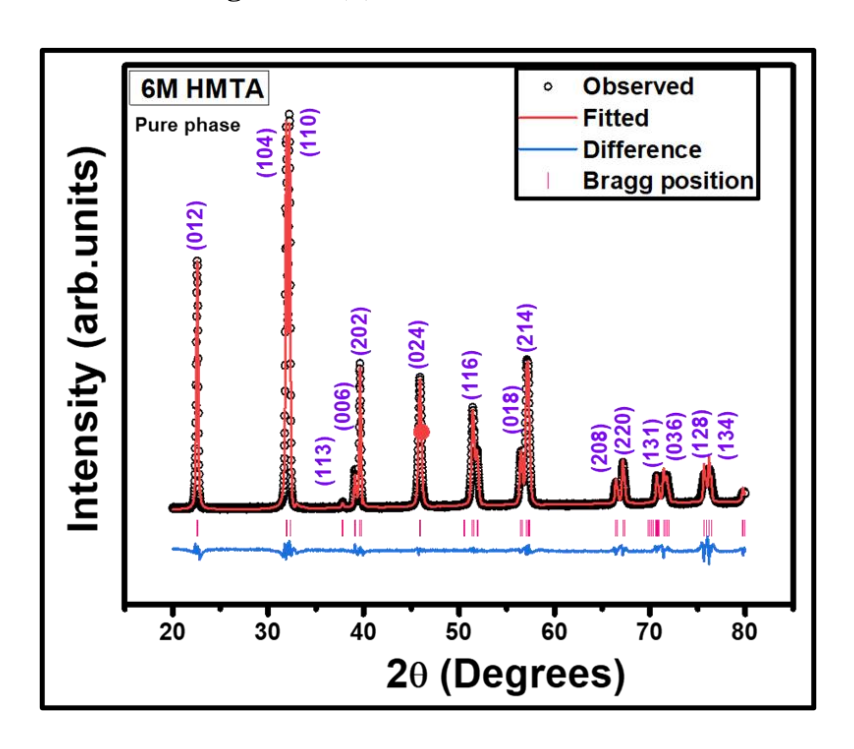


Figure 3. 3. Rietveld refinement of X-ray diffraction of pure phase BFO synthesized with 6M HMTA under 4h of solvothermal treatment at 180°C.

This is in line with the data that has been provided (ICSD: 98-023-7368). The concentration of HMTA significantly impacts how quickly the precursors dissolve and pure phase BFO forms, according to XRD analysis. Therefore, one of the most important variables in solvothermal reactions is optimising an appropriate molar ratio of an organic HMTA as a precipitation agent. After HMTA concentration was optimised, we used 6M HMTA and 4 hours of solvothermal heating to produce a highly pure phase BFO. The Rietveld refinement using High Score Plus software produced the Rhombohedral distorted perovskite crystal system with the R_{3c} space group in **figure 3. 3.** We were able to reproduce all the observed results using this crystal structure. The unit cell parameters acquired as a result of the Rietveld refinement analysis are displayed in **table 3.1**. The experimentally determined unit cell parameters agree with those found in published research [27].

Table 3. 1. Rietveld refined crystallographic unit cell values for pure phase BFO (6M HMTA)

Parameters	Experimental Data	Literature values (27)	Reference (ICSD Card No. 98-023- 7368)
a (Å)	5.58133	5.572	5.5720
b (Å)	5.58133	5.572	5.5720
c (Å)	13.86787	13.847	13.8350
α (°)	90.000	90.000	90.000
β (°)	90.000	90.000	90.000
γ (°)	120.000	120.000	120.000
Volume (10 ⁶ pm ³)	374.2824	372.326	371.99

3.4.2. FE-SEM Micrographs of BFO powders

The microstructures of the BFO powder were analysed using FE-SEM, a powerful structural characterization method, as the majority of the attributes of multiferroic materials heavily depend on their microstructures. **Figure 3. 4(a-d)** displays the FE-SEM images of BFO powder produced at various HMTA concentrations (0.5M, 2M, 4M, and 6M). According to the FE-SEM pictures, it has been found that when the HMTA concentration rises, the BFO microstructures gradually transform into more uniform granular structures with larger pores. As seen in **figure 3.4(a)**, the BFO powder produced by synthesising it with 0.5 M HMTA comprises various grains with irregular grain development in some areas. The granular size has risen, and the discontinuous grain growths have been restricted to some places for the 2M HMTA concentration [**figure 3.4(b)**]. Additionally, we have observed small clusters of BFO particles that are discontinuously expanding in various directions as the HMTA concentration was increased from 2M to 4M [**figure 3.4(c)**]. When the HMTA concentration rose from 4M to 6M, we observed a massive cluster of BFO nanoparticles with wide pores and different grain sizes.

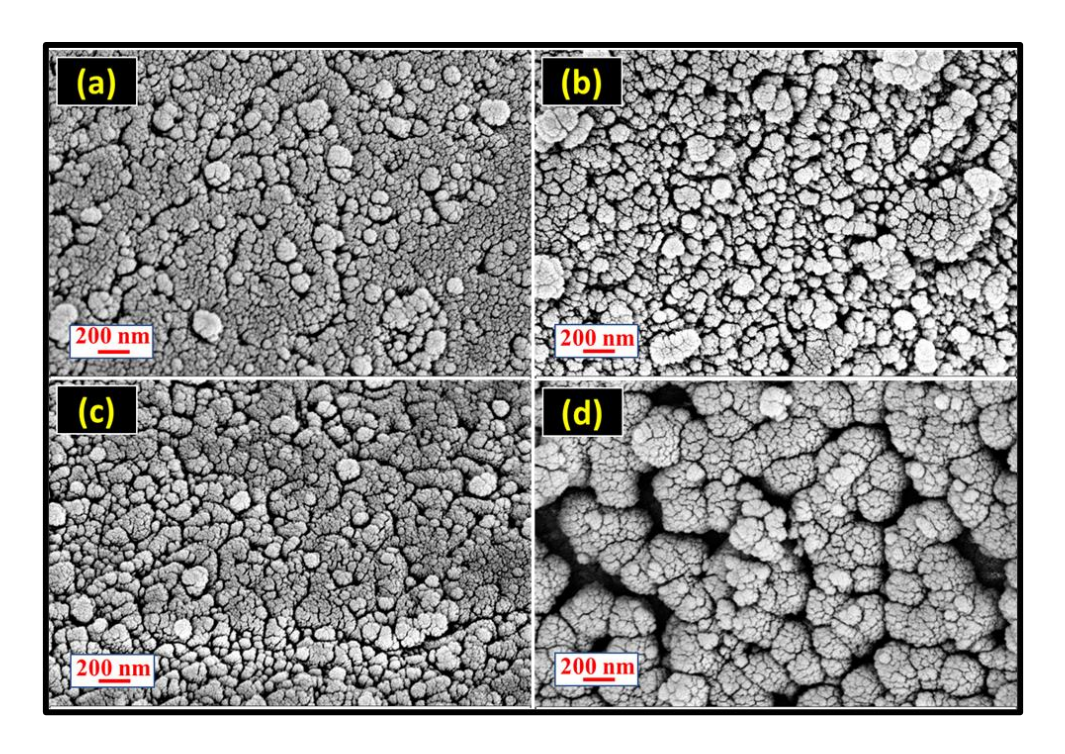


Figure 3.4. FESEM Micrographs of BFO powder synthesized at different HMTA concentrations a) 0.5M, b) 2M, c) 4M, and d) 6M prepared by solvothermal method at $180^{\circ}C$ for 4 hrs.

In light of these findings, we conclude that the increased HMTA concentration (6M) encourages continuous grain formation, presumably due to variations in metal ion diffusion rates at various HMTA concentrations. As a result, we conclude that the organic HMTA played a crucial role in precipitating the BFO nanostructures and attaining phase pure BFO using the solvothermal method.

3.4.3. Fourier transform infrared spectroscopy analysis (FTIR)

Multiferroic materials need to be characterised to learn more about the linked groups' structural and functional characteristics using FTIR (Fourier transform infrared spectroscopy) research. **Figure 3.5** depicts the FTIR spectra of BFO powders made by a solvothermal reaction with varying HMTA concentrations at 180°C for 4 hours. The FTIR spectra show that the absorption modes for all four BFO samples range from 400-3500 cm⁻¹. An absorption band that is within 1000 cm⁻¹ is what creates the bond between inorganic elements [27]. The BFO [28] modes correspond to vibrational bands between 650 and 400 cm⁻¹.

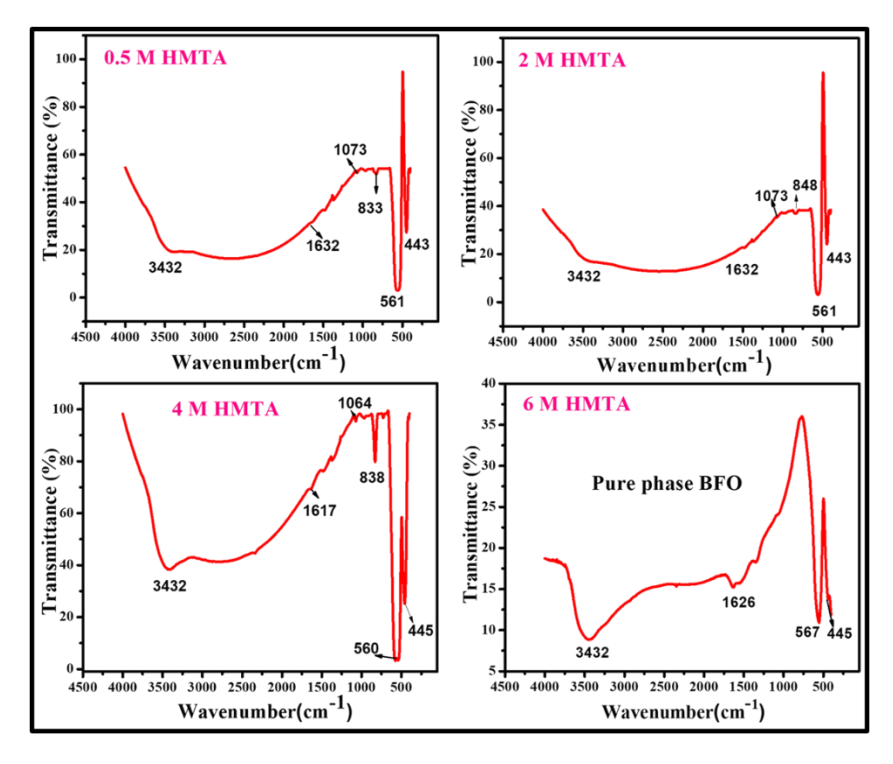


Figure 3.5. Fourier transform infrared spectroscopy of the BFO sample synthesized with different HMTA concentrations (0.5, 2, 4, and 6M) at 180°C for 4hrs.

The iron-oxygen (Fe-O) stretching and iron-oxygen (Fe-O) vibration of BFO, respectively, are represented by the low-intensity absorption bands in the region of 400 cm⁻¹ and 600 cm⁻² ¹ for all the samples (0.5, 2, 4, and 6 M HMTA), which can be regarded as a characteristic of octahedra (FeO₆) [29]. BFO samples exhibit absorption peaks at 550–568 cm⁻¹ and 1063–1073 cm⁻¹ due to vibrations of the Bi-O bonds. These linkages between metal and oxygen attest to the development of BFO's rhombohedral perovskite structure [30]. The bending vibration of water molecules was assigned to the absorption band at 1631 cm⁻¹. The broad absorption band at 3000-3750 cm⁻¹ is caused by the asymmetric and symmetric stretching of the hydroxyl (OH⁻) and hydrogen dioxide (H₂O) groups, respectively [31]. BFO powders synthesized with 0.5, 2, and 4M HMTA have much broader absorption bands at 3432cm⁻¹ than pure phase BFO synthesized with 6M HMTA, suggesting that these samples contain more hydroxyl groups and residual water than pure phase BFO, indicating that additional heat treatment is necessary to remove these hydroxyl groups and residual water from BFO samples (synthesized with 0.5, 2, 4M, HMTA). On the other hand, pure phase BFO doesn't need additional heat treatment (synthesized at 6M HMTA). The BFO powder samples made at 0.5, 2, and 4M HMTA displayed an absorption peak in the 830-848 cm⁻¹ region, indicating the presence of trapped or unreacted chloride residues. Contrarily, the BFO powder made at 6M HMTA showed no such absorption peak (in the region of 830-848 cm⁻¹), demonstrating the creation of a highly pure phase of BFO. The extremely pure phase of BFO was successfully produced using the solvothermal method and 6M HMTA, according to the FTIR analysis, without requiring extra calcination.

3.4.4. Raman spectroscopy analysis

The Raman spectra of BFO powders produced at varied HMTA concentrations are shown in **figure 3.6** at room temperature (0.5, 2, 4, and 6M). Raman scattering is a method of molecular vibrational spectroscopy that may be used to identify any molecular system's distinct fingerprint and investigate the dynamics of different materials' lattices [32]. The group theory predicts that the severely deformed ABO₃ (perovskite) structure known as the Rhombohedral BFO, which belongs to the R_{3c} space group, should have 13 Raman active modes (4A1+E) [33]. The BFO produced with 0, 2, 4, and 6M HMTA have, respectively, 7 (2A1+5E), 8 (3A1+5E), 9 (3A1+6E), and 11 (3A1+8E) Raman active modes out of the 13 standard active modes as described for BiFeO₃ in the prior publications [34, 35]. The obtained Raman spectra showed that the Raman active vibrational modes at the high-

frequency range ($> 400~\rm cm^{-1}$) are related to the stretching vibrations of (Fe) Iron - atoms within the FeO₆ octahedron, while the vibrational modes at the low-frequency range (400 cm⁻¹) are linked to the preferential state of the (Bi) Bismuth-atoms in the Rhombohedral perovskite unit.

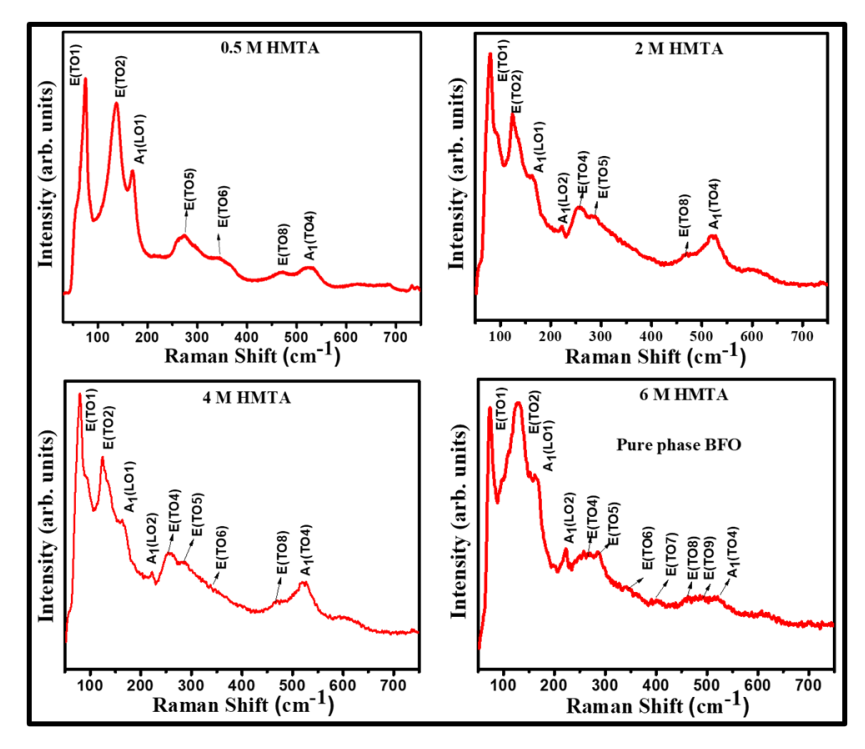


Figure 3.6. Raman spectra of BFO powders synthesized with different HMTA concentrations (0.5, 2, 4, and 6M) by solvothermal method at 180°C for 4hrs.

The Bi - O covalent bonds are related to the Raman vibrational active modes and longitudinal active peaks below 170 cm⁻¹ [36]. The presence of iron atoms within the FeO₆ octahedral structure is indicated by the active Raman stretching vibrational mode at 522 cm⁻¹. The distorted ferroelectric state is responsible for the vibrational modes E about 263–273 cm⁻¹, while the internal stretching of the FeO₆ octahedral structure is responsible for all other E vibrational modes around 295, 346, 470, and 497 cm⁻¹ [37]. As a result, **figure 3.6** demonstrates that the Raman peaks of all the BFO samples created using various HMTA concentrations are related to the rhombohedral BFO perovskite structure. It is important to note that when HMTA concentration rises, more Raman active modes are observed, indicating that the BFO is becoming more crystalline. These Raman study findings support the X-ray diffraction findings by demonstrating that the BiFeO₃ (BFO) nanoparticles synthesised with 6M HMTA have a pure phase and more excellent crystallinity than other samples (synthesised at 0.5, 2, and 4M HMTA).

Table 3.2. Raman Modes for the BFO samples synthesized at different HMTA concentrations.

Standard 13 Raman Modes [33]	BFO (0.5M) (Cm ⁻¹)	BFO(2M) (Cm ⁻¹)	BFO (4M) (Cm ⁻¹)	BFO (6M) (Cm ⁻¹)
E (TO1)	76	78	78	77
E (TO2)	135	132	131	129
A1 (TO1)	171	168	165	164
E (TO3)	-	-	-	-
E (TO4)	-	258	265	265
A1 (TO2)	-	221	223	223
E (TO5)	275	271	280	276
A1 (TO3)	-	-	-	-
E (TO6)	344	-	349	346
E (TO7)	-	-	-	378
E (TO8)	472	470	464	464
E (TO9)	-	-	-	492

A1 (TO4)	525	520	522	522

3.4.5. Dielectric properties of BFO samples

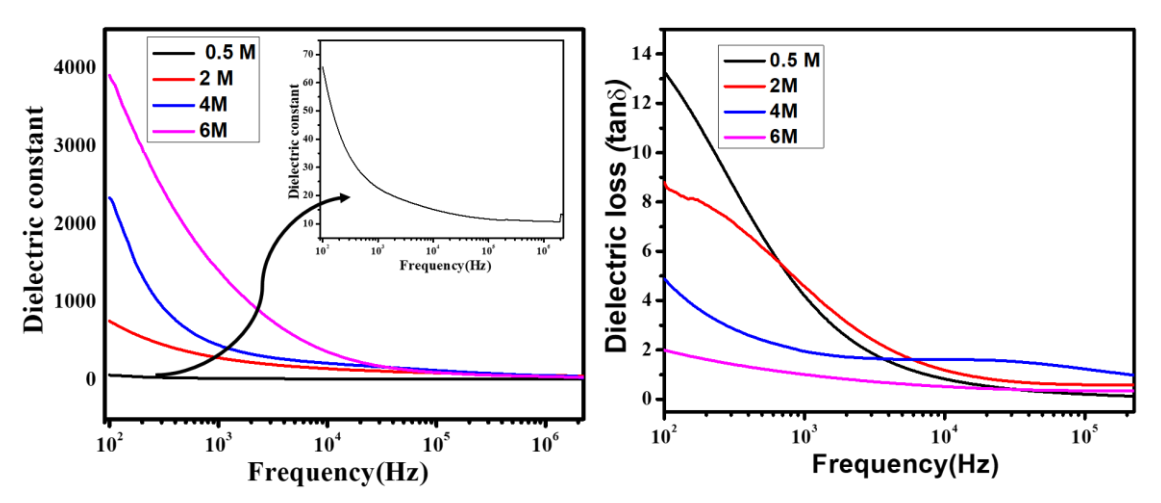


Figure 3.7. Room temperature dielectric properties a) dielectric constant, b) Dielectric loss of BFO samples synthesized at different HMTA concentrations (0.5, 2, 4, and 6M).

At frequencies between 100 Hz and 20 MHz, the room temperature dielectric constant and dielectric loss of BFO samples with various HMTA concentrations (0.5, 2, 4, and 6M) were calculated. All of the BFO samples were synthesized using various concentrations of HMTA, as shown in figure 3.7(a), and their room temperature-dependent dielectric constants (0.5, 2, 4, and 6M). It has been noted that as HMTA concentration rises, the dielectric constant also rises. At lower frequencies (less than 1 kHz), we have seen a substantial frequency dependency of the dielectric constant, and at higher frequencies, we have seen a sharp drop. The dielectric constant's diminishing tendency slows down as frequency rises and stays constant at higher frequencies. The pure phase BFO sample synthesised at 6M HMTA has a relatively high dielectric constant value (4k) at low frequencies, followed by a progressive decline in that value to reach nearly the lowest stable value at higher frequencies, in contrast to BFO samples synthesised with 0.5, 2 and 4M HMTA. It is possible that the uniform grain growth effect and the contribution of grain boundary volume are to blame for the increase in the dielectric constant. In addition, the number of domains and the mobility of the domain walls affects the dielectric constant. Additionally, it is thought that homogeneous grain size results in very simple and regular domain wall movement, which raises the dielectric constant. The mechanical deformation of the unit cells when the Curie transition temperature is reached results in internal strains

in the substance. As a result, the homogeneity and grain size influence the internal tension. Uniform grain size reduces internal tension, which facilitates simpler domain wall motion. An amorphous grain boundary has a lower dielectric constant value than a crystalline grain boundary, as is widely known from the literature. Due to the possibility that they also exhibit dielectric behaviour due to space charge polarisation, the fraction/percentages of BFO grain border volume decreases as grain size increases [38–41]. According to Koop's theory, the grain boundaries and grains appeared d to be arranged in series and parallel patterns, similar to how space charge polarisation occurs [42]. Free charges can oscillate back and forth when an AC electric field is applied, moving in the direction of the applied electric field towards the material's surface. Charge builds up on the dielectric surface as a result. The free charge carriers are more likely to migrate at lower frequency ranges and less likely to move at higher frequency ranges because of the physical resistance provided by the dielectric material during each reversal. It means that, in general, a sufficient period is needed for the free charge carriers in a dielectric substance to adapt to the field reversal. This causes the direction of the field reversals to lag behind the applied field, which lowers the material's dielectric constant. As a result, the frequency of field reversals will rise to the point where the electric polarisation can no longer sustain its saturation. However, as the electric field frequency rises, the space charge carriers eventually begin to migrate just before the field reverses, having essentially no impact on the polarization of the dielectric. Thus, even at high frequencies, the dielectric constant is unchanged. Dielectric materials frequently experience this behaviour. Therefore, room-temperature dielectric behaviour may be observed in all BFO samples made at various HMTA concentrations.

The dielectric loss of the materials in the alternating applied electric field can be used to explain the lagging of the dielectric polarisation, as shown in **figure 3.7 (b).** Dielectric loss is typically brought on by impurities, structural uniformity, and flaws in the crystal lattice of the dielectric materials. The dielectric loss tangent of the BFO samples generated at various HMTA concentrations (0.5, 2, 4, and 6M) decreased with increasing frequency and was roughly constant at high frequencies in this investigation. A higher dielectric loss was observed in the BFO synthesised with 0.5, 2, and 4M than in the pure phase BFO (6M). Due to the presence of impurity phases [**figure 3.2 (a-c)**], structural flaws, and a large number of grains and grain boundaries in these materials' microstructures [**figure 3.4 (a-c)**], the samples with more significant grain boundaries show a high electrical resistance at low frequencies as a result of their grain boundary contributions, whereas the samples with

larger grains show a low electrical resistance at high frequencies. Accordingly, the high energy required for the interchange of electrons between Fe²⁺ and Fe³⁺ in these samples at low frequency (high resistivity area) is the cause of the significant dielectric loss. Similarly, a comparatively small amount of energy is required to transport electrons between the ions of different valence states in the same crystal lattice site in the high-frequency zone, which correlates to a region with low resistivity and minimal dielectric loss a result.

3.4.6. Room temperature Magnetic behaviour of BFO

The magnetic properties of the BFO powder synthesized with various HMTA concentrations are shown in **figure 3.8**. (0.5, 2, 4, and 6M). Here, we studied at all the BFO samples made at various HMTA concentrations' magnetic characteristics at room temperature (RT; M-H). Even though the geometries of M-H hysteresis loops made from different concentrations of HMTA (0.5, 2, 4, and 6M) are very similar, the magnetic moments in each sample are distinct and weakly ferromagnetic at ambient temperature.

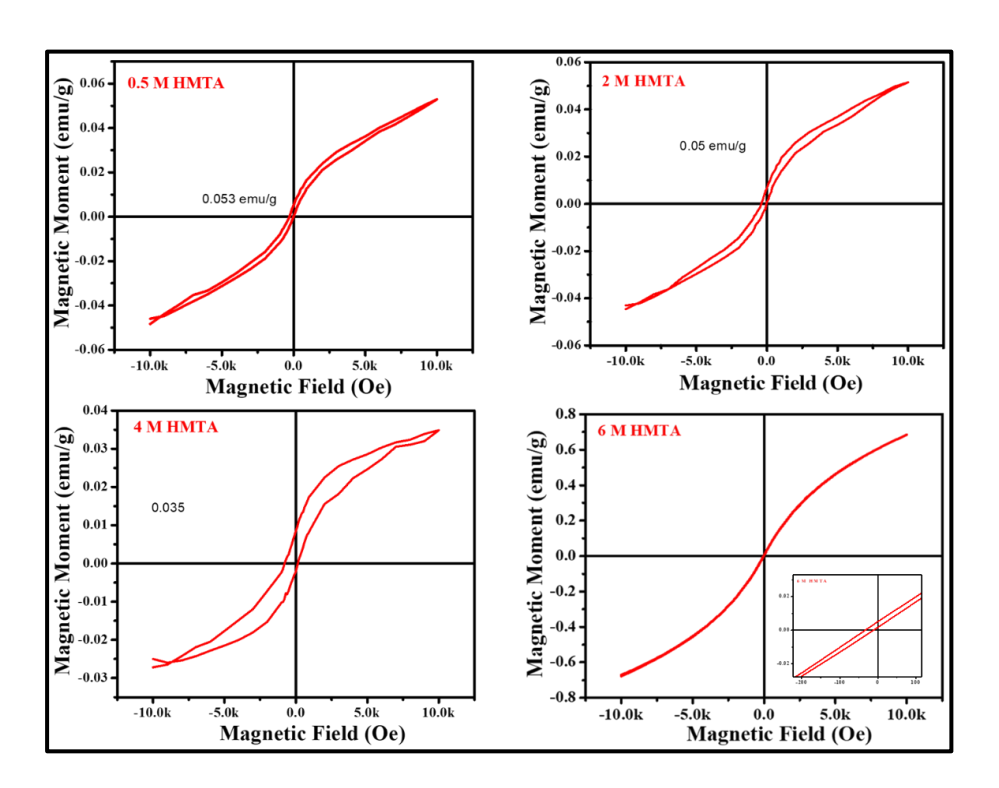


Figure 3.8. Room temperature Magnetic behaviour of the BFO samples synthesized with different HMTA concentrations (0.5, 2, 4, and 6M) at 180°C for 4h.

Because the Bi₂Fe₄O₉ and Fe₂O₃ magnetic phases occur at 0.5M HMTA [**figure 3.2(a**)], the BFO synthesised at 0.5M displayed a high magnetization value (0.053 emu/g) in

comparison to BFO synthesised at 2 and 4M HMTA. The removal of the magnetic phases Bi₂Fe₄O₉ and Fe₂O₃ [**figure 3.2(b)**], as well as the discontinuous grain development of the nanoparticles, cause the magnetization to drop (0.05 emu/g) as the concentration of HMTA rises from 0.5 to 2M. The magnetic moment of BFO fell to 0.034 emu/g (**figure 3.8**) with an increase in HMTA concentration from 2 to 4M, which is explained by the presence of the non-magnetic Bi₂O₃, Bi₂₂Fe₂O₃₆ phases and the complete reduction of the weak ferromagnetic phases such as Fe₂O₃ and Bi₂Fe₄O₉ [**figure 3.2(b-c)**]. A pure phase BFO displays a high magnetization value (0.72 emu/g) at 6M HMTA concentration in contrast to all other samples. Due to the high crystalline content of pure phase BFO and the steady enlargement of numerous nanosized grain boundaries and grains, the magnetization value in pure phase BFO at 6M has increased. As a result, every grain and grain boundary will contribute to the sample's magnetization value.

Table 3.3: Different magnetic parameters calculated from magnetic properties of BFO samples

Samples (BFO)	M _r (emu/g)	M _s (emu/g)	H _c (k Oe)
0.5M HMTA	0.005	0.053	32.97
2M HMTA	0.006	0.051	13.39
4M HMTA	0.006	0.034	155.48
6M HMTA	0.008	0.721	31.99

3.4.7. Room temperature Ferroelectric behaviour of BFO

To study the room temperature ferroelectric (P-E hysteresis loops) behaviour of BFO samples, an external electric field with a range of 5 to 15 kV/cm and a constant frequency of 100 Hz was applied. **Figure 3.9** shows that all of the BFO samples created at 0.5, 2, 4, and 6M HMTA exhibit unsaturated P-E loops. Compared to BFO samples made at 0.5, 2, and 4M HMTA, the pure phase BFO (6M HMTA) had a higher ferroelectric property. It is evident from **Figure 3.9** that the applied electric field has a significant influence on the P-

E hysteresis loops. Hysteresis loops were seen for applied electric fields under 15 kV/cm; however, at the highest voltage, no saturation was seen, indicating that polarisation switching was only partially completed. As the applied electric field grew (up to 15kV/cm), a maximum reversal occurred. Compared to the BFO samples made with 4 and 6M HMTA, the BFO samples made with 0.5 and 2M HMTA exhibit very poor remnant polarisation (2P_r) and saturation polarization (2P_s) values. We attempted to apply a stronger electric field (>6 kV/cm) to these samples (0.5 and 2M) to increase saturation, but the significant leakage in the samples prevented us from going any higher than 6 kV/cm.

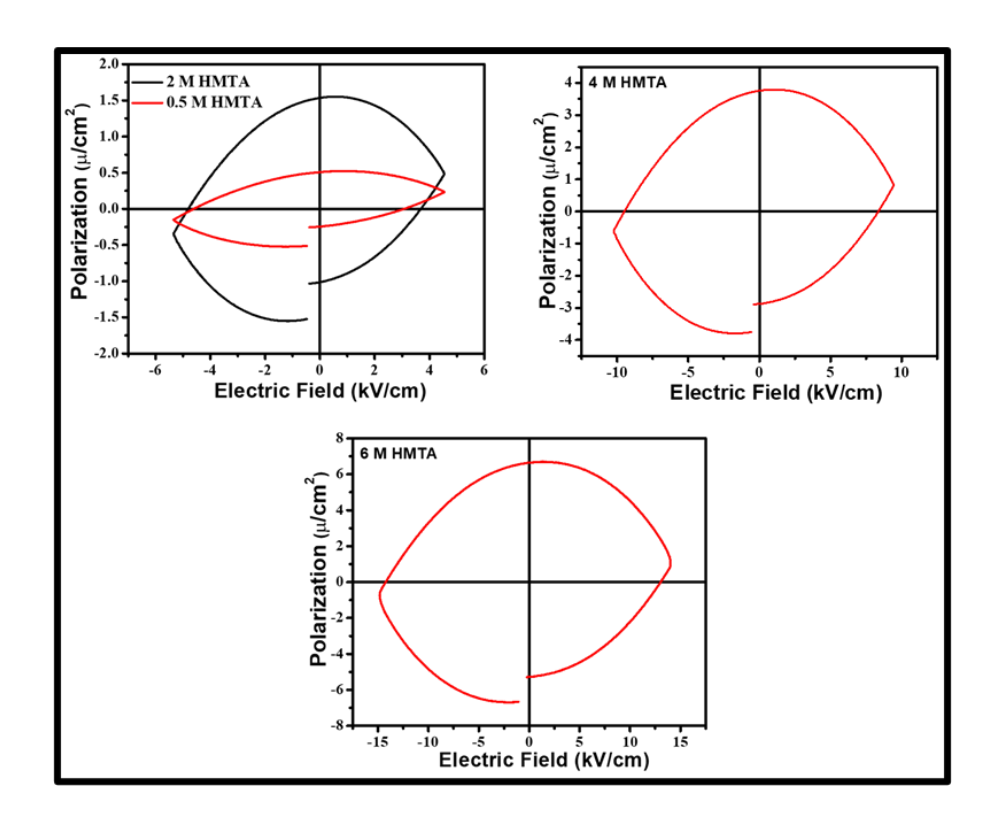


Figure 3.9. The room temperature ferroelectric behaviour of BFO samples synthesized at different HMTA concentrations (0.5, 2, 4, and 6M).

These samples may have significant leakage currents because of impurity phases [figure 3.2(a-b)]. Additionally, compared to the BFO samples with 0.5 and 2M HMTA, the BFO sample with 4M HMTA exhibits higher 2P_r and 2P_s values, and this sample allowed us to apply a field up to 10 kV/cm (P-E loops below 10 kV/cm had rounded shapes and were not shown in figure 3.9). This sample's increase in 2P_r and 2P_s is related to the decrease in the percentage of impure phases, which is the main reason for leakage current [figure 3.2(c)]. Pure phase BFO made at 6M HMTA shows much better ferroelectric properties than BFO samples made at 0.5, 2, and 4M HMTA. The field is limited to 15 kV/cm due to the

material's lossy behaviour, despite our attempts to apply a field higher than that to obtain a more saturated loop. It is important to note that the pure phase BFO has better $2P_r$ and $2P_s$ values than the other samples. The enhancement of $2P_r$ and $2P_s$ may be attributable to the pure phase BFO nanostructures [**figure 3.4(d)**]. According to the literature, the ferroelectrics' domain mobility, domain expansion, and grain size significantly impact their ferroelectric properties [44]. As a result of their function as a polarisation centre, grain boundaries prevent polarisation switching. As a result, the ferroelectric feature in tiny grain BFO is suppressed more, whereas electric polarisation switching is simpler in large grain BFO. All of the samples' lossy and unsaturated P-E loops could result from substantial leakage current, which can be explained by the formation of oxygen vacancies linked to the ionic moments of Fe³⁺ and Fe²⁺ ions [45–48]. Numerous studies have noted the same leaky behaviour for the pure phase BFO [49–54].

Table 3.4. Calculated Ferroelectric parameters for BFO samples derived from ferroelectric properties

Samples (BFO)	2P _r (μc/Cm ²)	2P _s (μc/Cm ²)	2E _c (kV/Cm ²)
0.5M HMTA	0.50	0.24	3.1
2M HMTA	1.55	0.49	3.69
4M HMTA	3.77	0.81	8.37
6М НМТА	6.65	1.02	13.19

3.4.8. Optical properties of pure phase BFO (synthesized at 6M HMTA)

Using a UV-VIS-NIR spectrophotometer in the 200-800 nm range, the optical characteristics of pure phase BFO produced at 6M HMTA were examined. It must absorb visible light (400–800 nm) and have a bandgap between 1.23 eV and 3.0 eV to be a visible photocatalyst [55]. **Figure 3.10** shows that the pure phase BFO is a visible photocatalyst due to its prominent 535 nm absorption peak. The peak broadness reveals the material's

greater ability to absorb electromagnetic radiation in the visual region. Optical absorption spectra can be used to calculate the optical band absorption edge, but not the precise bandgap of pure materials. According to **figure 3.10**, the intrinsic transitions for BFO are responsible for an optical absorption edge at about 535 nm. The optical band gap was determined using the classical Tauc's formula [56], which states that $\alpha h\vartheta = A(h\vartheta - E_g)n$ where h is the photon energy, E_g is the optical energy band gap, n is either 1/2, 3/2, 2 or 3, and A is a constant. In order to determine the optical bandgap energy, we have considered that n=1/2 permits a direct optical band gap for pure phase BFO, depending on the type of electronic transition responsible for optical absorption. For pure phase BFO, we plotted $(\alpha h \nu)^2$ as a function of $h\nu$ and determined the direct bandgap's value by extrapolating a tangent from the resulting slope.

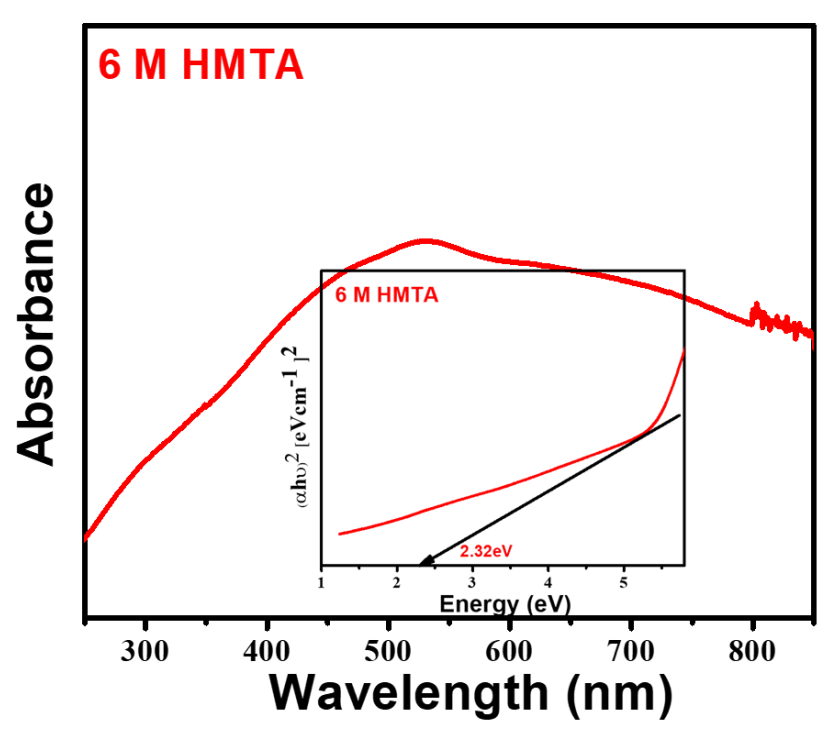


Figure 3.10. UV-Visible-NIR absorption of pure phase BFO synthesized at 6M HMTA under 4h of solvothermal treatment.

Our material's optical absorption bandgap value, 2.32 eV, is the tangent's X-intercept. This value is quite similar to the values of BFO that have been previously reported [57]. Therefore, multiferroic semiconductor applications would be appropriate for the pure phase BFO produced with HMTA as a precipitating agent.

3.4.9. Photocatalytic activity of pure phase BFO

Photocatalytic performance test. The photodegradation performance of MB was examined by irradiating MB+BFO under the heavy sunlight above the solution [**figure 3.11**]. 10mg/L of MB was dissolved in distilled water to prepare the solution. Then 40 mg of catalyst (BFO, synthesized at 6M HMTA) was added, and the solution was kept under the sunlight with a constant magnetic stirring. Throughout the illumination, an aliquot of the solution was taken at intervals of 30 minutes.

Photodegradation of MB. Figure 3.10 shows time dependant UV-visible-NIR absorbance spectra for the MB recorded from 450 to 800 nm while it was exposed to sunlight, followed by periodic sample collection. When BFO is used as a photocatalyst, the intensity of the light absorption band at 664 nm decreases with time, representing the characteristic wavelength of MB and confirming the degradation of the MB. MB degraded significantly in the presence of BFO catalyst within 180 min. The following equation calculates the degradation efficiency.

$$Efficiency = \frac{C_0 - C_t}{C_0} x \ 100$$

Where C₀ is the initial concentration of MB and C_t is the concentration of MB at time t. By substituting those values, we have calculated the photocatalytic activity of BFO, which shows 10% degradation in the MB under heavy sunlight irradiation time of 180 min. The low photodegradation performance of pure phase BFO might be due to the broader bandgap (2.32 eV) and very short separated electron-hole pairs.

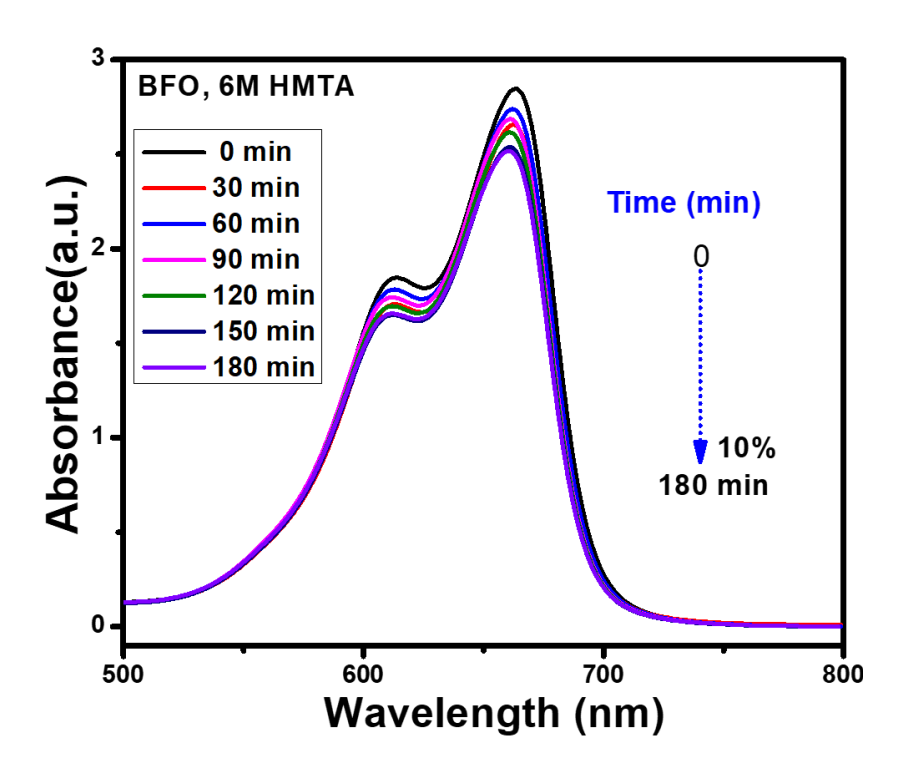


Figure 3.11. Time-dependent UV-Vis spectral changes of MB in the presence of pure phase BFO (6M HMTA).

3.5. Conclusion

As a result, we have shown that the solvothermal heating approach, in combination with the use of HMTA, an organic-based precipitation agent, is the simplest and most effective way to create single-phase multiferroic bismuth ferrite (BFO). After 4 hours of heating chemical reagents solvothermal at 6M HMTA in an ethanol medium, pure single phase BiFeO3(BFO) is produced. To determine the optimal conditions that would produce pure phase BFO, the concentration of HMTA was changed while keeping the reaction time and temperature constant. At a high concentration of 6M HMTA, all characterizations have shown the development of a very pure phase of BFO. The BFO particle's surface morphology is significantly influenced by the concentration of HMTA, according to optimization of HMTA concentration. Structural characterizations from FE-SEM and XRD support the morphology and pure phase of the synthetic BFO material. For the ambient temperature, dielectric spectroscopy is performed to evaluate the dielectric characteristics of BFO qualitatively. BFO with a single pure phase, produced at 6M HMTA, has a high dielectric constant and a low dielectric loss. VSM was also used to determine how HMTA concentration affected the magnetic characteristics. A significantly high magnetic moment of 0.72 emu/g has been observed in the pure phase BFO (6M HMTA). Additionally, the P-

E hysteresis loop provides information on how HMTA concentration affects the ferroelectric characteristics of BFO. The lossy, unsaturated P-E loops and polarisation were highly dependent on the materials' applied voltage, structural phases, and microstructure. Additionally, while having a narrower band gap of 2.32 eV, the pure phase BFO (6M HMTA) demonstrated outstanding absorption in the visible area. The magnetic, ferroelectric, dielectric, and optical properties of pure phase BFO have significantly improved as a result of the various characterizations of the material, and they can now be used for multiferroic semiconductor applications. In comparison with the other semiconductor material, the synthesised material using the solvothermal process with 6M HMTA had a very poor photocatalytic performance on the degradation of MB.

REFERENCES

- 1. Lee, C., Liu, J., Whangbo, M.H., Koo, H.J., Kremer, R.K. and Simon, A., 2012. Investigation of the spin exchange interactions and the magnetic structure of the high-temperature multiferroic CuBr₂. *Physical Review B*, 86(6), p.060407.
- 2. Eerenstein, W., Mathur, N.D. and Scott, J.F., 2006. Multiferroic and magnetoelectric materials. *nature*, 442(7104), pp.759-765.
- 3. Wang, J.B.N.J., Neaton, J.B., Zheng, H., Nagarajan, V., Ogale, S.B., Liu, B., Viehland, D., Vaithyanathan, V., Schlom, D.G., Waghmare, U.V. and Spaldin, N.A., 2003. Epitaxial BiFeO₃ multiferroic thin film heterostructures. *science*, 299(5613), pp.1719-1722.
- 4. An, X., Deng, J., Chen, J. and Xing, X., 2013. Facile and rapid synthesis of multiferroic TbMnO₃ single crystalline. *Materials Research Bulletin*, 48(12), pp.4984-4988.
- 5. Bhide, V.G. and Multani, M.S., 1965. Mössbauer effect in ferroelectric-antiferromagnetic BiFeO₃. *Solid State Communications*, *3*(9), pp.271-274.
- 6. Yu, H., Guo, H., Zhu, W., Zhuang, J., Ren, W. and Ye, Z.G., 2015. Multiferroic 0.7 BiFeO₃–0.3 PbTiO₃ thin films prepared by a sol-gel method. *Thin Solid Films*, 585, pp.82-85.
- 7. Michel, C., Moreau, J.M., Achenbach, G.D., Gerson, R. and James, W.J., 1969. The atomic structure of BiFeO₃. *Solid State Communications*, 7(9), pp.701-704.
- 8. Kumar, M.M., Palkar, V.R., Srinivas, K. and Suryanarayana, S.V., 2000. Ferroelectricity in a pure BiFeO₃ ceramic. *Applied physics letters*, 76(19), pp.2764-2766.
- 9. Chakrabarti, K., Das, K., Sarkar, B. and De, S.K., 2011. Magnetic and dielectric properties of Eu-doped BiFeO₃ nanoparticles by acetic acid-assisted sol-gel method. *Journal of Applied Physics*, 110(10), p.103905.
- 10. Gao, F., Chen, X.Y., Yin, K.B., Dong, S., Ren, Z.F., Yuan, F., Yu, T., Zou, Z.G. and Liu, J.M., 2007. Visible-light photocatalytic properties of weak magnetic BiFeO₃ nanoparticles. *Advanced materials*, *19*(19), pp.2889-2892.
- 11. Ghosh, S., Dasgupta, S., Sen, A. and Maiti, H.S., 2005. Low temperature synthesis of bismuth ferrite nanoparticles by a ferrioxalate precursor method. *Materials research bulletin*, 40(12), pp.2073-2079.

- 12. Ghosh, S., Dasgupta, S., Sen, A. and Sekhar Maiti, H., 2005. Low-temperature synthesis of nanosized bismuth ferrite by soft chemical route. *Journal of the American Ceramic Society*, 88(5), pp.1349-1352.
- 13. Chen, C., Cheng, J., Yu, S., Che, L. and Meng, Z., 2006. Hydrothermal synthesis of perovskite bismuth ferrite crystallites. *Journal of Crystal Growth*, 291(1), pp.135-139.
- 14. Shetty, S., Palkar, V.R. and Pinto, R., 2002. Size effect study in magnetoelectric BiFeO₃ system. *Pramana*, 58(5), pp.1027-1030.
- 15. Achenbach, G.D., James, W.J. and Gerson, R., 1967. Preparation of single-phase polycrystalline BiFeO₃. *Journal of the American Ceramic Society*, 50(8), pp.437-437.
- 16. Rabenau, A., 1985. The role of hydrothermal synthesis in preparative chemistry. *Angewandte Chemie International Edition in English*, 24(12), pp.1026-1040.
- 17. Feng, S. and Xu, R., 2001. New materials in hydrothermal synthesis. *Accounts of chemical research*, 34(3), pp.239-247.
- 18. Walton, R.I., 2002. Subcritical solvothermal synthesis of condensed inorganic materials. *Chemical Society Reviews*, *31*(4), pp.230-238.
- 19. Zhu, Y.J. and Chen, F., 2014. Microwave-assisted preparation of inorganic nanostructures in liquid phase. *Chemical reviews*, 114(12), pp.6462-6555.
- 20. Lai, J., Niu, W., Luque, R. and Xu, G., 2015. Solvothermal synthesis of metal nanocrystals and their applications. *Nano Today*, *10*(2), pp.240-267.
- 21. Zhu, Y.J. and Chen, F., 2014. Microwave-assisted preparation of inorganic nanostructures in liquid phase. *Chemical reviews*, 114(12), pp.6462-6555
- 22. Byrappa, K. and Adschiri, T., 2007. Hydrothermal technology for nanotechnology. *Progress in crystal growth and characterization of materials*, 53(2), pp.117-166.
- 23. Hojamberdiev, M., Xu, Y., Wang, F., Wang, J., Liu, W. and Wang, M., 2009. Morphology-controlled hydrothermal synthesis of bismuth ferrite using various alkaline mineralizers. *Ceramics–Silikáty*, 53(2), pp.113-117.
- 24. Banoth, P., Sohan, A., Kandula, C., Kanaka, R.K. and Kollu, P., 2022. Microwave-Assisted Solvothermal Route for One-Step Synthesis of Pure Phase Bismuth Ferrite Microflowers with Improved Magnetic and Dielectric Properties. *ACS omega*, 7(15), pp.12910-12921.

- 25. Wang, G., Lin, C., Liu, S., Deng, Q., Mao, Y. and Wang, S., 2018. Hydrothermal synthesis of bismuth ferrite with controllable phase structure, morphology and visible light photocatalytic activities. *Journal of Materials Science: Materials in Electronics*, 29(6), pp.4926-4932.
- 26. Wang, G., Lin, C., Liu, S., Deng, Q., Mao, Y. and Wang, S., 2018. Hydrothermal synthesis of bismuth ferrite with controllable phase structure, morphology and visible light photocatalytic activities. *Journal of Materials Science: Materials in Electronics*, 29(6), pp.4926-4932.
- 27. Biasotto, G., Simões, A.Z., Foschini, C.R., Zaghete, M.A., Varela, J.A. and Longo, E., 2011. Microwave-hydrothermal synthesis of perovskite bismuth ferrite nanoparticles. *Materials Research Bulletin*, 46(12), pp.2543-2547.
- 28. Sharif, M.K., Khan, M.A., Hussain, A., Iqbal, F., Shakir, I., Murtaza, G., Akhtar, M.N., Ahmad, M. and Warsi, M.F., 2016. Synthesis and characterization of Zr and Mg doped BiFeO3 nanocrystalline multiferroics via micro emulsion route. *Journal of Alloys and Compounds*, 667, pp.329-340.
- 29. Chauhan, S., Arora, M., Sati, P.C., Chhoker, S., Katyal, S.C. and Kumar, M., 2013. Structural, vibrational, optical, magnetic and dielectric properties of Bi _{1- x} Ba_x FeO₃ nanoparticles. *Ceramics International*, *39*(6), pp.6399-6405.
- 30. Čebela, M., Janković, B.Ž., Hercigonja, R.V., Lukić, M.J., Dohčević-Mitrović, Z., Milivojević, D. and Matović, B., 2016. Comprehensive characterization of BiFeO₃ powder synthesized by the hydrothermal procedure. *Processing and Application of Ceramics*, 10(4), pp.201-208.
- 31. Moharana, S., Mishra, M.K., Chopkar, M. and Mahaling, R.N., 2016. Enhanced dielectric properties of surface hydroxylated bismuth ferrite–Poly (vinylidene fluoride-co-hexafluoropropylene) composites for energy storage devices. *Journal of Science: Advanced Materials and Devices*, *1*(4), pp.461-467.
- 32. Lotey, G.S. and Verma, N.K., 2013. Multiferroic properties of Tb-doped BiFeO₃ nanowires. *Journal of nanoparticle research*, 15(4), pp.1-14.
- 33. Jasrotia, R., Singh, V.P., Kumar, R. and Singh, M., 2020. Raman spectra of sol-gel auto-combustion synthesized Mg-Ag-Mn and Ba-Nd-Cd-In ferrite-based nanomaterials. *Ceramics International*, 46(1), pp.618-621.

- 34. Srivastav, S.K. and S. Gajbhiye, N., 2012. Low temperature synthesis, structural, optical and magnetic properties of bismuth ferrite nanoparticles. *Journal of the American Ceramic Society*, 95(11), pp.3678-3682.
- 35. Verma, R., Chauhan, A., Batoo, K.M., Kumar, R., Hadhi, M. and Raslan, E.H., 2021. Effect of calcination temperature on structural and morphological properties of bismuth ferrite nanoparticles. *Ceramics International*, 47(3), pp.3680-3691.
- 36. Haumont, R., Kreisel, J., Bouvier, P. and Hippert, F., 2006. Phonon anomalies and the ferroelectric phase transition in multiferroic BiFeO₃. *Physical Review B*, 73(13), p.132101.
- 37. Lin, J.W., Tite, T., Tang, Y.H., Lue, C.S., Chang, Y.M. and Lin, J.G., 2012. Correlation of spin and structure in doped bismuth ferrite nanoparticles. *Journal of Applied Physics*, 111(7), p.07D910.
- 38. Kumar, M.M., Palkar, V.R., Srinivas, K. and Suryanarayana, S.V., 2000. Ferroelectricity in a pure BiFeO₃ ceramic. *Applied physics letters*, 76(19), pp.2764-2766.
- 39. Zhang, S.T., Lu, M.H., Wu, D., Chen, Y.F. and Ming, N.B., 2005. Larger polarization and weak ferromagnetism in quenched BiFeO₃ ceramics with a distorted rhombohedral crystal structure. *Applied Physics Letters*, 87(26), p.262907.
- 40. Cao, W., Chen, Z., Gao, T., Zhou, D., Leng, X., Niu, F., Zhu, Y., Qin, L., Wang, J. and Huang, Y., 2016. Rapid synthesis of single-phase bismuth ferrite by microwave-assisted hydrothermal method. *Materials Chemistry and Physics*, 175, pp.1-5.
- 41. Koops, C.G., 1951. On the dispersion of resistivity and dielectric constant of some semiconductors at audiofrequencies. *Physical review*, 83(1), p.121.
- 42. Jiang, Q., Ning, H., Zhang, Q., Cain, M., Reece, M.J. and Yan, H., 2013. Active ferroelectricity in nanostructured multiferroic BiFeO₃ bulk ceramics. *Journal of Materials Chemistry C*, 1(36), pp.5628-5631.
- 43. Koops, C.G., 1951. On the dispersion of resistivity and dielectric constant of some semiconductors at audiofrequencies. *Physical review*, 83(1), p.121.
- 44. Rhaman, M.M., Matin, M.A., Hakim, M.A. and Islam, M.F., 2019. Dielectric, ferroelectric and ferromagnetic properties of samarium doped multiferroic bismuth ferrite. *Materials Research Express*, 6(12), p.125080.

- 45. Cai, W., Fu, C., Hu, W., Chen, G. and Deng, X., 2013. Effects of microwave sintering power on microstructure, dielectric, ferroelectric and magnetic properties of bismuth ferrite ceramics. *Journal of alloys and compounds*, 554, pp.64-71.
- 46. Kazhugasalamoorthy, S., Jegatheesan, P., Mohandoss, R., Giridharan, N.V., Karthikeyan, B., Joseyphus, R.J. and Dhanuskodi, S., 2010. Investigations on the properties of pure and rare earth modified bismuth ferrite ceramics. *Journal of alloys and compounds*, 493(1-2), pp.569-572.
- 47. Lan, C., Jiang, Y. and Yang, S., 2011. Magnetic properties of La and (La, Zr) doped BiFeO₃ ceramics. *Journal of materials Science*, 46(3), pp.734-738.
- 48. Singh, R. and Dutta, S., 2018. Synthesis and characterization of solar photoactive TiO₂ nanoparticles with enhanced structural and optical properties. *Advanced Powder Technology*, 29(2), pp.211-219.
- 49. Dhana Lakshmi, B., Pratap, K., Rao, B. P., & Rao, P. S. (2016). Effects of Mn doping on structural, dielectric and multiferroic properties of BiFeO₃ nanoceramics. *Journal of Alloys and Compounds*, 676, 193-201.
- 50. Banoth, P., Sohan, A., Kandula, C., Kanaka, R.K. and Kollu, P., 2022. Microwave-Assisted Solvothermal Route for One-Step Synthesis of Pure Phase Bismuth Ferrite Microflowers with Improved Magnetic and Dielectric Properties. *ACS omega*, 7(15), pp.12910-12921.
- 51. Basith, M.A., Billah, A., Jalil, M.A., Yesmin, N., Sakib, M.A., Ashik, E.K., Yousuf, S.E.H., Chowdhury, S.S., Hossain, M.S., Firoz, S.H. and Ahmmad, B., 2017. The 10% Gd and Ti co-doped BiFeO₃: a promising multiferroic material. *Journal of Alloys and Compounds*, 694, pp.792-799.
- 52. Alam, M. and Mandal, K., 2021. Origin of ferroelectricity in multiferroic ErFeO₃. *Physica B: Condensed Matter*, 612, p.412935.
- 53. Hasan, M., Hakim, M.A., Basith, M.A., Hossain, M.S., Ahmmad, B., Zubair, M.A., Hussain, A. and Islam, M.F., 2016. Size dependent magnetic and electrical properties of Ba-doped nanocrystalline BiFeO₃. *AIP Advances*, 6(3), p.035314.
- 54. Kumar, S., Kumar, P., Walia, R. and Verma, V., 2019. Improved ferroelectric, magnetic and photovoltaic properties of Pr doped multiferroic bismuth ferrites for photovoltaic application. *Results in Physics*, *14*, p.102403.
- 55. Tauc, J. ed., 2012. Amorphous and liquid semiconductors. Springer Science & Business Media.

- 56. Srivastav, S.K. and S. Gajbhiye, N., 2012. Low temperature synthesis, structural, optical and magnetic properties of bismuth ferrite nanoparticles. *Journal of the American Ceramic Society*, 95(11), pp.3678-3682.
- 57. Papadas, I., Christodoulides, J.A., Kioseoglou, G. and Armatas, G.S., 2015. A high surface area ordered mesoporous BiFeO₃ semiconductor with efficient water oxidation activity. *Journal of Materials Chemistry A*, *3*(4), pp.1587-1593.

Chapter-4

Microwave-assisted solvothermal route for one-step synthesis of pure phase Bismuth Ferrite micro flowers with improved magnetic and dielectric properties

Objectives

- ❖ The present work aims to synthesize highly crystalline BFO in a rapid reaction time without any post-annealing.
- ❖ The structure, microstructure, magnetic, dielectric, ferroelectric and optical properties are investigated.
- ❖ The novelty of the current approach is that very few works have reported the production of BFO within a short reaction of time. Our goal was to synthesize the BFO with the microwave-assisted solvothermal method within the shortest possible time by optimizing the MW power, duration, and mineralizer concentration.

4.1. Introduction

A room temperature multiferroic Bismuth ferrite (BFO) is popular because it combines ferroelectricity as well as anti-ferromagnetism in the same phase with high transition temperatures. This extraordinary multiferroic behaviour has applications in spintronics, information storage, multiple-state memory, and sensing [1-4]. BFO shows G-type antimagnetism with a homogeneous magnetic field spin arrangement at Neel temperature (650 K) and high Curie temperature ($T_C = 1100 \text{ K}$). The spontaneous magnetization in BFO is caused by the partially filled orbits of Fe, while the 6s^2 lone-pair electrons cause the electric polarization on Bi, which may be integrated with a different phase. However, due to secondary bismuth-rich phases, poor spontaneous polarisation, and low magnetic properties, its possible future applications in satellite communications, optical filters, sensors, cameras, memory, and intelligent devices are restricted. Additionally, its mild insulating sensitivity due to the drop from Fe³⁺ to Fe²⁺ and oxygen vacancies has limited its applicability [5–6].

Many scientists have worked hard in recent years to create pure BFO crystals and ceramics utilising various synthesis techniques, including solid-state, soft-chemical, wet-chemical, microemulsion, and others [7-9]. Since most of these methods involve a common sintering step (typically at 500-900°C), the possibility of impurity additions is more due to high temperatures and pressures, where the stability of the pure phase BFO is disrupted sensitively during the synthesis process. The secondary impure phases (Bi₂Fe₄O₉ and Bi₂₅FeO₄₀) produced during the production process are also removed using nitric acid in the solid-state approaches. However, this process yields low-quality, inconsistent powder because bismuth and iron oxide are mixed before being heated by calcination. The required pure phase BFO is thus difficult to achieve when all the affecting impacts during the fabrication are considered. Recently, Ghosh et al. [12] used a tartaric acid-based sol-gel method with an extra sintering procedure to produce pure phase BFO nano-powder. Pure BFO ceramics have been created by Wang et al. [10] and Pradhan et al. [11] using a quick fluid-phase sintering technique. Avoiding bismuth condensation in such methods is challenging since the BFO crystallisation process necessitates high temperatures over the ferroelectric T_C .

To present, two synthesis techniques-liquid, phase sintering and percolation techniqueshave been identified as more effective for producing single-phase BFO. The undesirable phases are removed using the techniques by diluting the precursors with nitric acid. However, the practical device applications of the prepared sample are constrained by the large leakage current of the samples made utilising these two techniques. Therefore, to get pure single-phase BFO, it is imperative to synthesise and learn more about innovative synthesis techniques. Soft chemical methods can produce microcrystalline BFO at relatively low temperatures. Due to their simplicity and controllability over particle size, shape, and degree of crystallinity throughout the synthesis process, the hydrothermal and solvothermal procedures are more appealing and have attracted much interest among all chemical approaches [13–21]. However, the time it takes for a reaction to complete using this method might range from hours to days, which can restrict its usefulness for large-scale industrial processes. So, in the preceding procedures, the crystal growth rate should be sped up to shorten the reaction speed and form a single phase BFO of particles of the same size and a homogeneous bulk. The microwave (MW) heating method has recently received a great deal of attention [24–26] because of how fast it works, how uniform the samples are, how low the temperature range is, and how evenly the powders form nuclei. Many research teams have successfully created single-phase nanomaterials with high purity perovskites in a brief period at moderate temperatures without engaging in any other processes like sintering, agglomeration, gross powder development, etc. [22–23]. Shun Li et al. [27] reported pure degree BFO nanoplates employing NH₃.H₂O as a leaching agent to control the production of secondary phases. Rarely is the microwave-assisted solvothermal technique used to synthesise pure phase BFO published. Also, there hasn't been much research on the dielectric, and ferroelectric properties of BFO made this way.

Since ethanol has a high boiling point and a high loss tangent compared to other solvents, it allows for a rapid reaction rate in our work by combining the benefits of both the solvothermal and microwave approach to create BFO flowers [28]. To the greatest of our knowledge, only a few studies have shown reaction speed for the best and fastest synthesis methods (Microwave-assisted) of single crystal BFO usually ranges from fifteen to sixty minutes [29–33]. In this paper, we used the microwave-assisted-solvothermal (MWAST) technique to endorse our research for the first time by asserting that it was the fastest and most effective method of forming single-phase BFO within just three minutes without the need for dangerous acids. We also examined the magnetic, ferroelectric, and dielectric properties of freshly formed pure phase BFO flowers at room temperature.

4.2. Experimental Section

4.2.1. Materials

This method of production uses ethanol, double-distilled water, 98% pure potassium hydroxide (KOH), 98% pure ferric chloride (FeCl₃.6H₂O), 98% pure bismuth chloride (BiCl₃), and 98% pure ferric chloride (DDW). These chemical reagents were bought on the open market from the SRL firm in India.

4.2.2. Synthesis of BFO

The microwave-assisted solvothermal (MWAST) method synthesizes the pure phase BFO in a residential solo microwave oven with variable power from 200W to 800W and running at 2.45GHz. With the help of two metal precursors (BiCl₃ and FeCl₃.6H₂O) and a mineralizer, we created the BFO in powder form (KOH). BiCl₃ and FeCl₃.6H₂O were dissolved in ethanol and mechanically agitated for one hour at equimolar concentrations (0.05M). The dropwise addition of 8M KOH solution changed the initial solution. After 30 minutes of magnetic stirring, bismuth and iron precipitated as an oxide. A bespoke sealed

microwave acid digestion jar (model 4782 from Parr) with a 45 ml capacity was then filled with 10 ml of this mixture and placed in a handmade microwave oven. A steady microwave heating time of 3 minutes was used to carry out the chemical reactions while adjusting the microwave power levels from 360 W to 800 W. The reaction vessel was then allowed to cool to room temperature. The final reaction precipitate was cleaned in DDW before being dried for four hours at 80°C. Three samples were generated using 8M KOH for 3 minutes at three different MW power levels (360, 700, and 800 W). [BFO:360W, KOH(8M)], [BFO:700W, KOH(8M)], and [BFO:800W, KOH(8M)] were the samples' names. At 800 W and 8M KOH concentrations, the pure phase BFO nanoflowers were produced in three minutes. We have optimised the reactions by varying KOH concentrations from 6M to 12M to investigate the effect of mineralizer concentration on the microstructure of BFO.

We also synthesised BFO at 650 W for 15 minutes using four vessels of the commercial system (the system's maximum capacity is 16 vessels) in order to compare the microwave technology used in our studies with the commercially available microwave hydrothermal system (Model: Anton Paar Rotor 16). In order to assess the adaptability of getting pure phase BFO, the XRD results of the samples obtained using the two approaches were afterwards compared.

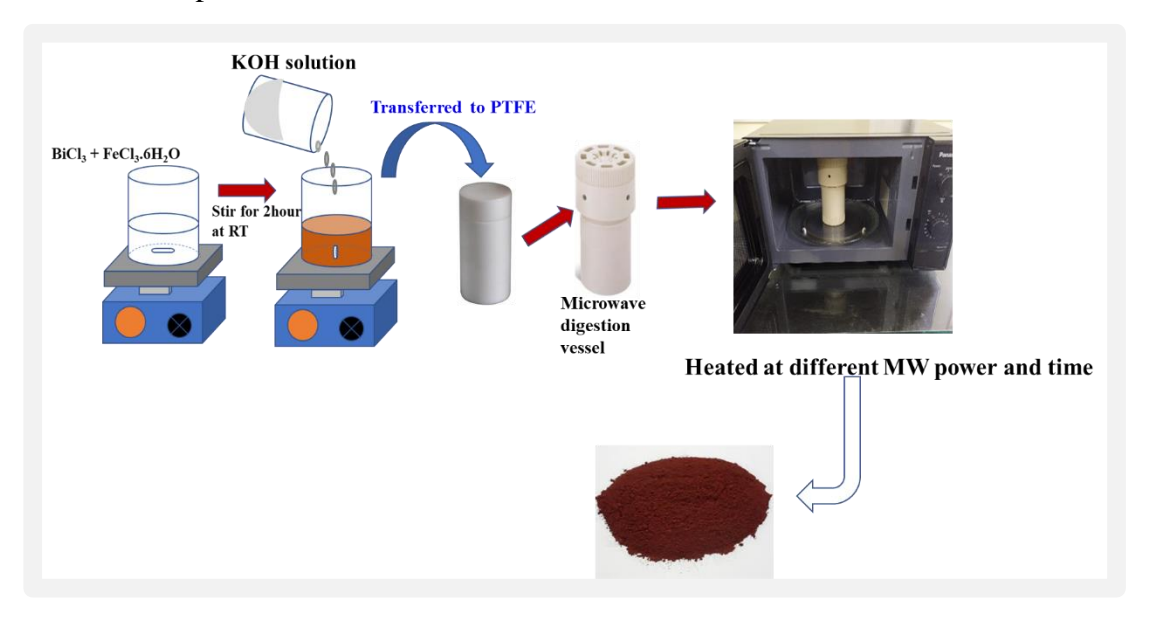


Figure 4.1. Synthesis procedure for BFO through solvothermal at 180°C for 4hrs.

4.3. Characterization techniques

The XRD analysis (PANalytical, X'Pert Powder Diffractometer) and Rietveld refinement demonstrate that BFO forms in the pure phase (Xpert High score plus-version 4.9). Field emission scanning electron microscopy (FESEM: Carl Zeiss Smart Sem) and transmission electron microscopy were used to study the morphology of BFO flowers (TEM: JEM-F200 kV). The elemental (Bi, Fe, and O) composition of pure phase BFO micro flowers has been verified by the energy dispersive x-ray (EDX) spectra and X-ray photoelectron microscopy (XPS) (Model: Axis Supra) data. At room temperature, measurements of the pure phase BFO's magnetic, dielectric, and ferroelectric properties were made using a vibrating sample magnetometer (VSM; LakeShore) and a dielectric spectrometer (Novocontrol GmBH), and a ferroelectric analyser (Trek Model 609B). FTIR (Model: Perkin Elmer-L1600400) and Raman (Model: HORIBA Micro-Raman) measurements of the produced BFO material were carried out to comprehend the composition of molecular mixtures and vibrational modes.

4.4. Results and Discussions

4.4.1. Structural analysis

Using a commercial microwave system (Model: Anton Paar Rotor 16, **figure S2**) and 650 W of power for 15 minutes, **figure S1** shows the XRD patterns of the as-synthesised BFO. We have noticed the production of several impurity peaks corresponding to Bi and Fe-rich phases from the collected XRD data, which are more pronounced than the pure phase BFO peaks (**figure S1**). This suggests that a commercial microwave system's reaction time is insufficient for the reaction to finish. The operating conditions and system settings may be responsible for impurity formations. We suspect that because the system requires a minimum of four vessels to operate, the power distribution across all vessels may not have been uniform, leaving the reactants unreacted even after longer periods of MW heating.

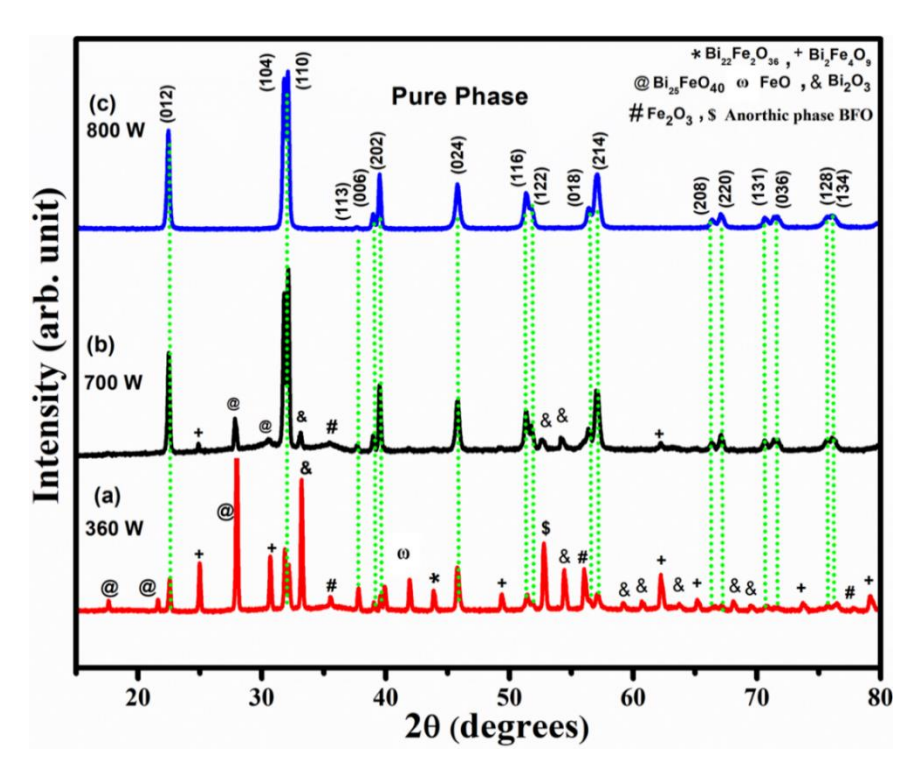


Figure 4.2. XRD patterns of BFO synthesized at different microwave powers: a)360W, b)700 W, c)800 W for 3 minutes with 8M KOH.

These unreacted chemical species are producing impurity peaks in the XRD data. Therefore, we want a sophisticated, simple approach for getting pure phase BFO to overcome these empirically discovered limits of a commercial microwave system and hasten the chemical process. To create a pure phase BFO, we thus used a straightforward microwave system that uses a domestic microwave oven and an acid digestion vessel. The pure phase BFO is attained with this microwave technique in a quick reaction time of three minutes. The likelihood of non-uniform microwave energy distribution is minimised, and the effective cross-sectional area is maximised in this microwave system, which can all work together to increase the reaction rate. Therefore, to get over the majority of the constraints provided by other methods/techniques, we adopted this quick method (MWAST) for all of our trials to get a pure phase BFO. To set an optimal parameter for the reaction time to form pure phase BFO, the microwave heating time was adjusted from 1 to 4 minutes at various microwave power levels (800, 700, and 360 W). In figure S3-S5, the XRD findings of BFO synthesised at 800, 700, and 360 W at various MW heating times (1 to 4 minutes) are shown. The pure phase BFO with a rhombohedral crystal structure is generated at 800 W after 3 minutes of microwave heating, according to the collected XRD data. To generate pure phase BFO utilising the MWAST method, the reaction duration of 3 minutes during microwave heating was specified as a constant parameter. Figure 4.2 displays the XRD patterns of the BFO produced by the MWAST process using ethanol as a solvent and different microwave powers from 360 to 800 W while heating the material for three minutes at a constant microwave power. Our results based on XRD data [figure 4.2 (a)] show that a large percentage of impurity peaks were found in just three minutes of microwave heating at 360 W.

Along with the already-existing rhombohedral pure phase BFO peaks, these impurity peaks include Bi₂₂Fe₂O₃₆ (ICSD: 98-024-8805), Bi₂Fe₄O₉ (ICSD: 98-002-6808), Bi₂₅FeO₄₀ (ICSD: 98-004-1937), Fe₂O₃ (ICSD: 98-005-6372), Bi₂O₃ (98-042-1856) These impurity peaks may represent chemical species that have not yet interacted. The intensity of all impurity peaks and their number have drastically decreased in the second sample synthesised at 700 W, as shown in [figure 4.2 (b)], with an increase in microwave power from 360 to 700 W. All of the impurity peaks that were previously evident in [figure 4.2 (a-b)] have been eliminated as a result of a further increase in microwave power from 700 to 800 W. The Rhombohedral distorted perovskite structure of BFO in the R_{3C} space group (ICSD 98-019-1940) with an average crystallite size of about 20 nm was well matched with the acquired XRD [figure 4.2 (c)] results. Thus, utilising the MWAST approach, the microwave power optimizations (360, 700, and 800 W) at a constant concentration of KOH (8M) result in the selection of a single MW power level (i.e., 800 W) for the quick threeminute synthesis of pure phase BFO. It is important to note that several experimental factors and settings contributed to the faster reaction time in our MWAST experiment. We think various factors may impact the sensitivity of the reaction rate in microwave oven heating studies. Important variables significantly influencing and substantially dictating reaction speeds and final product forms include solvent type, volume, vessel size, reaction mixture, and microwave power levels. Due to its high boiling point and high loss tangent, the solvent ethanol can help provide a favourable environment for the microwave-assisted synthesis of inorganic materials and provide enough heat for the reactants in the reaction medium [34]. The volume of the solvent/reaction vessel of choice affects how evenly the reaction mixture is heated across the volume, thus accelerating the reaction rate and eliminating any unreacted residues. In laboratories, smaller amounts can be employed to generate uniform heat from microwave energy to produce the quickest reactions. For larger volumes of reaction mixtures, we can increase the microwave energy/power to obtain the products in bulk for future industrial uses. As a result, microwave power is an unavoidable component that significantly impacts quick reactions with sensitivity and selectivity [35]. After

performing an XRD examination on the sample (produced at 800W, 8M KOH, 3 min), we refined the data using Rietveld refinement.

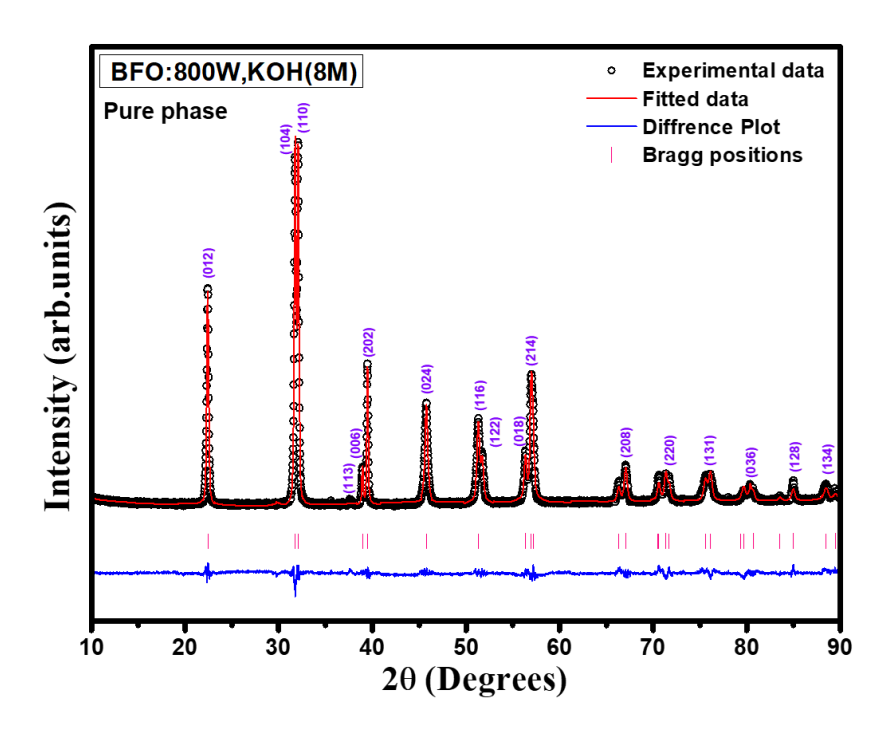


Figure 4. 3. Rietveld refinement of X-ray diffraction of pure phase BFO synthesized with 8M KOH under 3 minutes of microwave irradiation at 800W output power.

The outcomes of the Rietveld refinement performed using the perovskite rhombohedral crystal structure corresponding to the R_{3c} space group are shown in **figure 4.3**. This structural arrangement allowed us to reproduce all the observed reflections. The acquired lattice cell parameters were displayed in **table 4.1** based on the Rietveld refinement profile, and it has been noted that the experimental values obtained are in good agreement with the values given in the literature [36]. Additionally, we looked at how the KOH concentration affected the morphological and structural changes of the pure phase BFO after 3 minutes of 800 W microwave heating. The XRD patterns of BFO produced at various KOH concentrations (6M, 8M, 10M, and 12M) while maintaining all other parameters constant are shown in **figure 4.4**. We have observed considerable pure BFO peaks at 6M KOH concentration in addition to unreacted leftovers as Bi₂O₃ as shown in **figure 4.4** (a). This could result from the reduced precursor solubility at low KOH concentrations. As seen in **figure 4.4** (b), the rise in KOH concentration from 6M to 8M has changed the impurity phases that were already present (at 6M KOH) and transformed all the unreacted chemical species into BFO, leaving no traces of potential impurity peaks in the XRD data. The back-

dropped impurities (Bi₂O₃, Bi₂Fe₄O₉, and Bi₂₅FeO₄₉) at 10M KOH concentration have been noted as a result of the rise in KOH concentrations (from 8M to 10M), as illustrated in **figure 4. 4 (c)** may be the result of the decomposition of pure phase BFO [37-38].

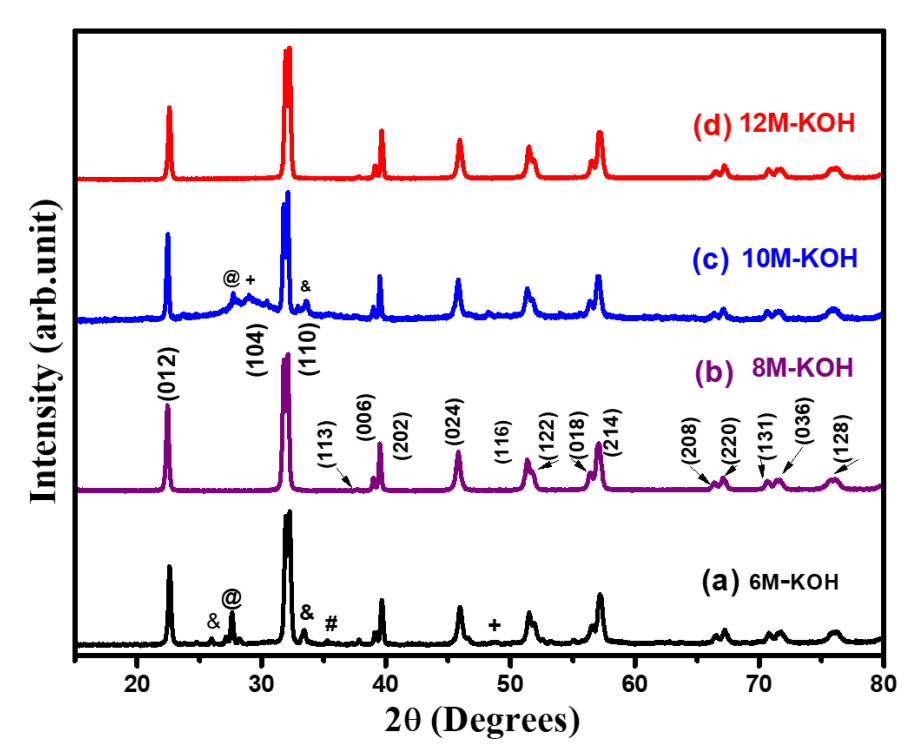


Figure 4.4. XRD patterns of pure phase BFO synthesized at different KOH concentrations a) 6M, b) 8M, c) 10M, d) 12M under 3 min of microwave irradiation at 800 W output power.

Additionally, we noticed that the pure phase BFO was driven back at very alkaline conditions (12M KOH), as seen in **figure 4.3** (d). This shows that all impurity phases were changed to single-phase BFO at greater alkaline conditions. Therefore, the concentration of mineralizer (KOH) is a crucial component in obtaining the single pure phase BFO, according to our findings based on XRD data analysis.

Table 4. 1. Crystallographic unit cell parameters obtained from Rietveld refinement for pure phase BFO as-synthesized at 800 W with 8M KOH.

Parameters	Experimental Data	Literature values ³⁶	Reference (ICSD Card No. 98-019- 1940)
a (Å)	5.57766	5.572	5.5820
b (Å)	5.57766	5.572	5.5820
c (Å)	13.86787	13.847	13.8780
α (°)	90.000	90.000	90.000
β (°)	90.000	90.000	90.000
γ (°)	120.000	120.000	120.000
Volume (10 ⁶ pm ³)	373.63	372.326	374.49
c/a ratio	2.4863	2.4851	2.4862
Agreement	$R_{\text{exp}} = 4.2142,$		
parameters indices	$R_p = 4.3124,$		
	$R_{wp} = 5.0806,$		
	$\chi^2 = 1.4520$		

4.4.2. Microstructural analysis

The properties of multiferroic materials are highly dependent on the microstructure of pure composites [39-42Researchers have recently studied the effect of mineralizer (KOH) on the formation of BFO micro flowers and reported that KOH concentration depends strongly on the size and shape of the flowers to enhance their magnetic and dielectric properties [43]. FESEM was used to investigate the structural properties of multiferroic material BFO synthesised at 800 W microwave heating for 3 minutes with different KOH concentrations (6M, 8M, 10M, and 12M). **Figure 4.5(a)** illustrates that the synthesized BFO (800W, 6M

KOH, 3min) is mainly composed of micro flowers with nano petals resembling miniature roses. **Figure 4.5(a)** shows the structural morphology of a miniature rose with multiple openly exposed petals surrounded by four interconnected petals. **Figure 4.5(b)** shows uniform spherical BFO flowers with similar shapes developed at 8M KOH. There are numerous magnificent nano petals with rectangular cages on the surface of the magnified single spherical shaped BFO microwave flowers, indicating a similar cage-like pattern as seen in **figure 4.5(a)** but with closed or covered petals.

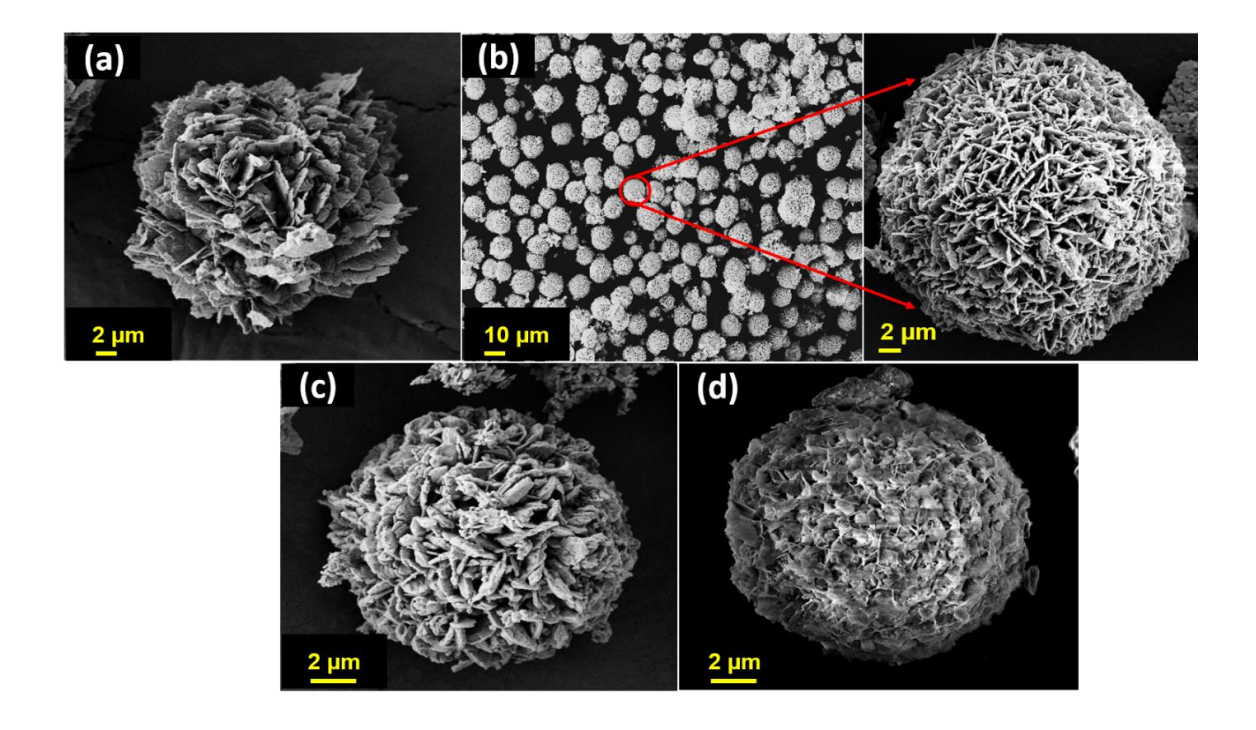


Figure 4.5. FESEM micrographs of BFO synthesized in three minutes at 800 W for a) 6M, b) 8M, C) 10M, and d) 12M KOH concentrations.

We have also observed that when the concentration of KOH is increased from 8M to 10M, the floral cages disappear due to increased growth and size of the petals, as shown in **figure 4.5(c)**. Similarly, for 12M KOH concentration, the floral cages completely disappeared due to masking from largely grown petals and turning the micro flowers into perfectly spherical balls [**figure 4.5(d)**], indicating the nucleation of petals at higher KOH concentrations. The microstructural analysis of BFO micro flowers using FESEM indicates that the mineralizer (KOH) has significantly influenced the shape, size, and number of crystalline petals of the developed flowers. It is believed that micro flower petals with inhomogeneous petals positions on their surface will assist in improving the dielectric property of pure phase BFO synthesized at 8M KOH [**figure 4.11(a)**].

Figure 4.6 shows the elemental composition of BFO synthesized using the MWAST method. The spectral peaks quantitatively represent the chemical elements that are present in the sample of the synthesised material. **Figure 4.6(a)** demonstrates that the prepared sample is pure BFO micro flower with no other impurities or pollutants. According to the EDAX quantitative study [**figure 4.6(b)**, Bi, Fe, and O's respective elemental compositions are 65.55%, 23.93% and 10.52%.

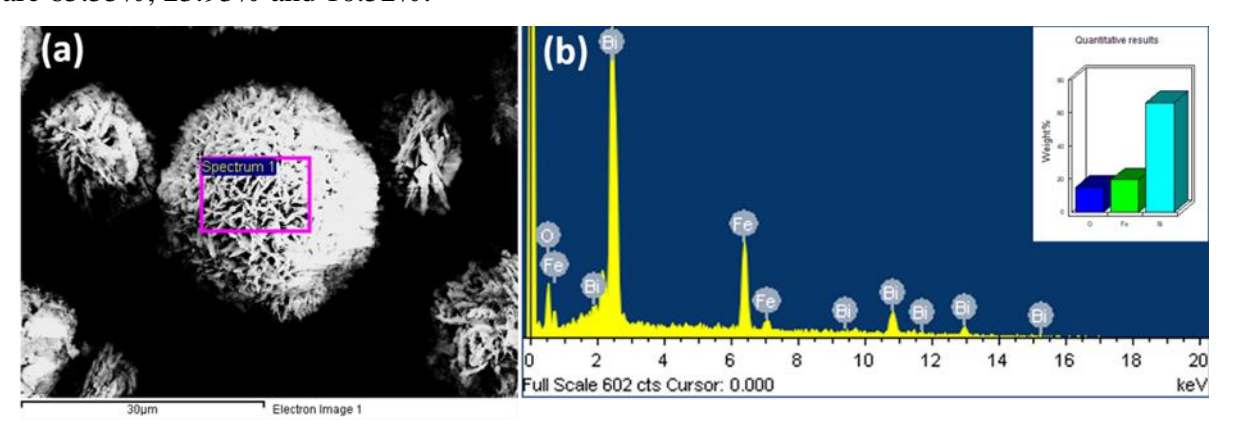


Figure 4.6. FESEM micrograph (a), EDAX spectra (b) of pure phase BFO synthesized with 8M KOH in 3 minutes at 800 W.

These elemental moles (%) values, which are 66.80%, 17.85%, and 15.34% of Bi, Fe, and O, respectively, are pretty near to the empirical formula BFO for pure bismuth ferrite [44].

4.4.3. Transmission electron microscopy (TEM) analysis

TEM, high-resolution TEM (HR-TEM), and selected area electron diffraction (SAED) analyses provide detailed structural features of synthesised pure phase BFO. By drop-casting BiFeO₃ solution onto a copper grid, the TEM sample was ready (coated with carbon). The BiFeO₃ solution was made by ultrasonically dispersing BiFeO₃ powder in ethanol. TEM images of pure phase BFO micro flower petals synthesised under ideal circumstances (800 W, 8 M KOH, 3 min) and utilising the MWAS approach are shown in **figure 4.7(a)**. **Figure 4.7(a)** shows that the petals of pure phase BFO flowers are made up of nanocrystalline BFO blocks that are more than 50 nm in size. To determine the crystallinity in the nanostructures of BFO micro flower petals, we used SAED and HRTEM analysis. Pure phase BFO is attributed to a perovskite rhombohedral structure with an R_{3c} space group and does not contain any amorphous phases. The SAED patterns of pure phase

BFO [figure 4.7(b)] show a regular arrangement of sharp diffraction spots suggesting perfect crystallisation of pure phase BFO.

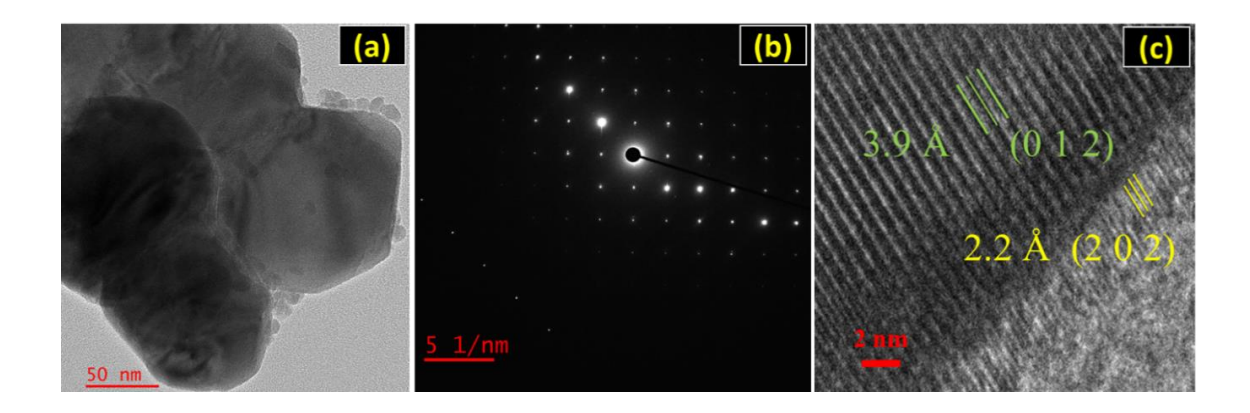


Figure 4.7. HRTEM images of BFO micro flowers (a) TEM image, (b) SAED patterns, and (c) HR-TEM image of BFO micro flowers synthesized at 800 W with 8M KOH in 3 min.

The HRTEM pictures of pure phase BFO flower petals synthesised at optimal conditions (800 W, 8M KOH, 3 min) are shown in **figure 4.7(c)**. The crystal planes' interplanar spacing was found to be 3.9 and 2.2 Å, respectively, corresponding to their respective crystal planes (012) and (202) of rhombohedral pure BFO. The structural characterization of BFO using TEM revealed remarkable results, in contrast to previously reported works that found aggregations and amorphous phases of BFO, indicating that the crystallinity of pure phase BFO micro flowers has no particle-particle aggregation that can enhance the multiferroic properties of BFO [45].

4.4.4. Fourier Transform Infrared Spectroscopy (FTIR) analysis

FTIR analysis is a crucial characterisation tool for gathering qualitative structural information about the functional groups and their interactions in multiferroic materials. To extrapolate the information from the elemental absorption bands of BFO produced at 800W, 8M KOH, and 3 minutes, we have evaluated the data acquired. The FTIR spectrum, whose spectral range was obtained from 400 to 4000 cm⁻¹, is shown in **figure 4.8**. A broad absorption band between 3000 and 3500 cm⁻¹ corresponds to the antisymmetric and symmetric stretching modes of water and OH⁻ bond factions. The peak at 1631 cm⁻¹ is believed to be caused by the vibrational bending of the water molecules. The Fe-O bond's bending vibration mode is associated with the high-intensity absorption peak at 561 cm⁻¹, while its stretching vibration mode is associated with the absorption peak at 442 cm⁻¹,

which can be understood as a defining characteristic of the octahedra [FeO₆] in the BFO perovskite structure [46–47]. Additionally, it was noted that there were no nitrates or other intermittent impurities, indicating that our material closely matched the literature that was accessible, especially with the pure phase of BFO [48–49].

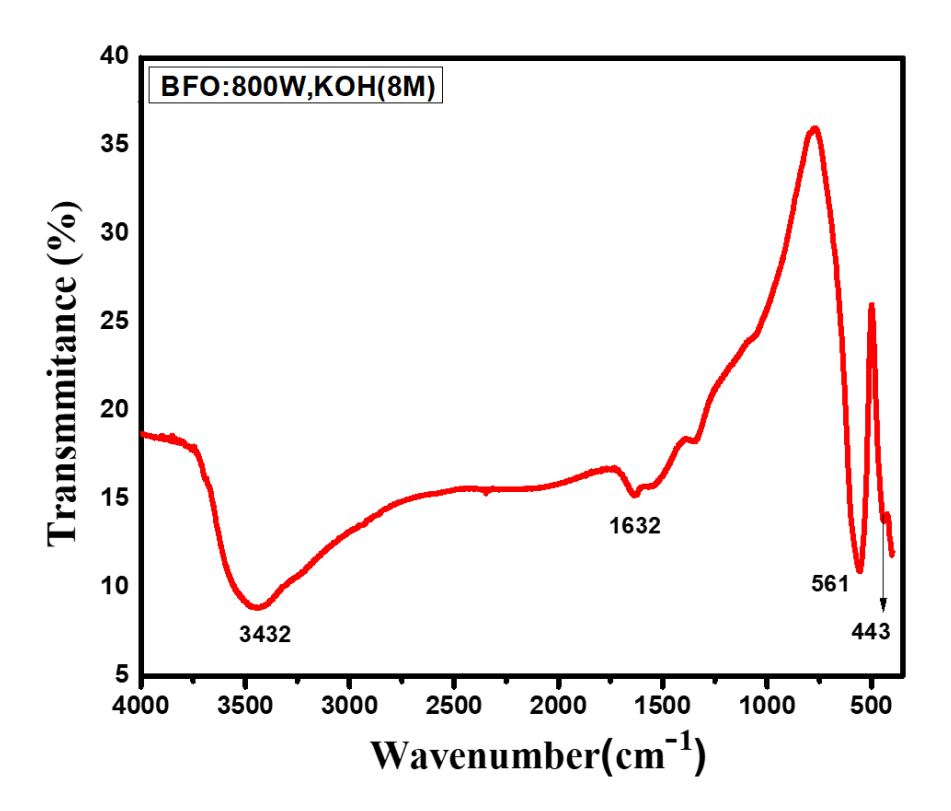


Figure 4.8. FTIR spectrum of BFO synthesized at 800 W in 3 minutes with 8M KOH.

4.4.5. Raman analysis

Raman scattering, a method of studying the lattice dynamics of diverse materials, is a molecular vibrational spectroscopic technique that can identify the distinctive fingerprint of any molecular system. The Raman spectra obtained from a 632 nm laser stimulation at room temperature are shown in **figure 4.9**. Based on the literature [50], 13 standard Raman modes are associated with R_{3C} space grouping of Rhombohedral distorted pure phase BFO material. The 3A1 and 9E transverse optical (TO) vibrational modes are present in the pure phase BFO produced at 800W in 3 minutes. The assignments of the observed vibrational modes have been determined in light of the literature review. In the acquired Raman spectra, we found ten transverse vibrational modes for pure BFO (one A1(TO)+nine E(TO) and two longitudinal A1(L.O.) modes).

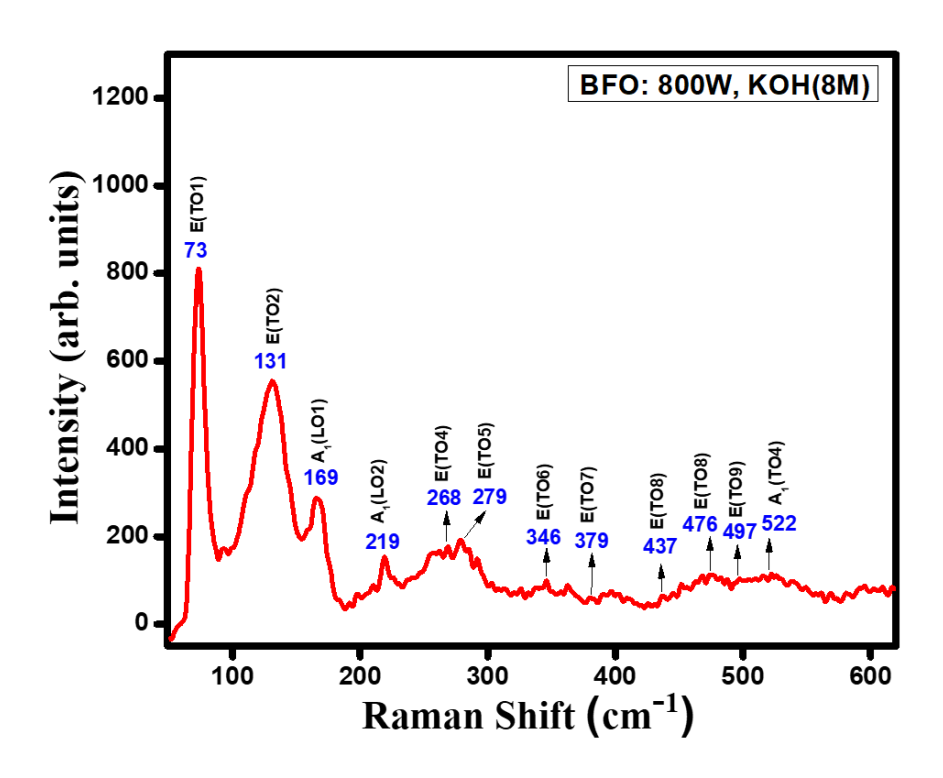


Figure 4.9. Room temperature Raman spectra of pure phase BFO synthesized with 8M KOH at 800 W microwave power for 3 minutes of microwave irradiation.

The E(T01), E(T02), A1(L01), A1(L02), E(T04), E(T05), E(T06), E(T07), E(T08), E(T08), E(T09), and A1(T04) modes, respectively, are represented by the Raman peaks at 73 cm⁻¹, 131 cm⁻¹, 169 cm⁻¹, 219 cm⁻¹, 268 cm⁻¹, 279 cm⁻¹, 346 cm⁻¹, while the oxygen motion predominates at higher wavenumbers (i.e., above 270cm-1), the vibrational modes and longitudinal modes provide information on the Bi atoms in lower wavenumber regions (i.e., below 170cm-1) [51–52].152 cm⁻¹ to 268 cm⁻¹ are where most of the Fe atom modes are observed, with a few occurring at higher wavenumbers. The E(TO1) and E(TO2) modes, which are present in our pure phase BFO sample's Raman spectrum, stand in for the covalent bond of Bi. According to Raman analysis, the multiferroic material synthesized using the MWAST method reveals a distinctive fingerprint of all bonds and vibrational modes, indicating the development of pure phase BFO.

4.4.6. X-ray Photoelectron Spectroscopy (XPS) analysis

Bi, Fe, and O constituent element's electron binding energies were studied using X-ray photoelectron spectroscopy, and the results support the purity of the single crystalline BFO phase. While analysing the XPS data for the pure phase BFO, oxygen vacancies and Fe²⁺ ions are closely monitored because they significantly impact the multiferroic characteristics [53–54]. Numerous structural flaws in a stoichiometric BFO could impact its magnetic and

electrical properties. The typical XPS spectra for the Bi, Fe and O elements at the core level are shown in **figure 4.10** (a-c). The core-level spectra of Bi 4f are shown in **figure 4.10** (a), indicating that the bismuth ion is in the +3-oxidation state due to its binding energy peaks at 161.62 and 156.31 eV with the corresponding spin-orbit splitting energies are discovered to be 5.31 eV for 5/2 and 7/2 spin-orbit doublet components. All of the Bi 4f values found closely match the previously reported ones [52].

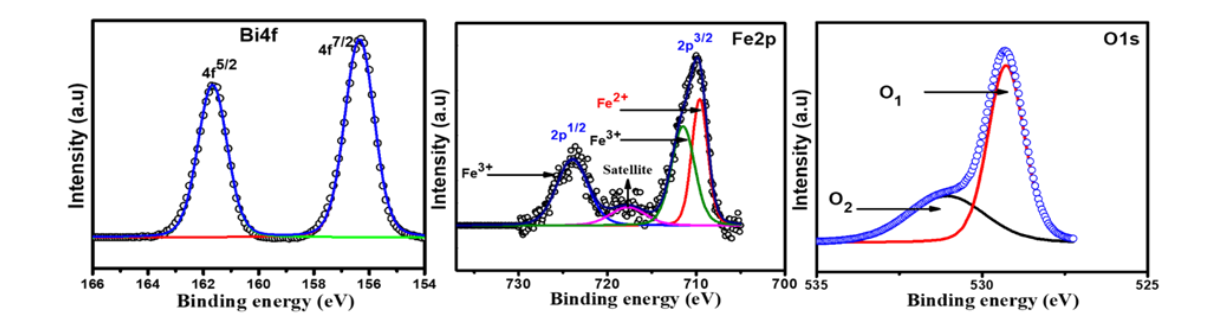


Figure 4.10. X-ray photoelectron spectroscopy core-level spectra for (a) Bi, (b) Fe, and (c) O elements of pure phase BFO micro flowers synthesized at 800 W with 8M KOH in 3 min.

The deconvolution of XPS core-level spectra of Fe 2p is shown in figure 4.10(b). The binding energy peaks for Fe 2p^{3/2} are well-known at 709 eV for the +2-oxidation state and 710.5 eV for the +3-oxidation state [55–57]. Two broad doublet peaks have been observed in an asymmetric scan of pure Fe 2p located at 724.21 eV and 711.03 eV a with spin-orbit splitting energy of 13.18 eV, respectively, confirming the +3-oxidation state of Fe and is consistent with earlier studies [58]. Fe 2p^{3/2} has two sub-bands at 711.03 eV and 709.49 eV that signify the presence of the +3 and +2 oxidation states of Fe ion, respectively. The Fe²⁺ intensity at an absolute peak is calculated based on the relative integral of the Fe²⁺ to the overall peak, which gives the proportion of Fe^{2+} (43%), Fe^{3+} (47%), and Fe^{4+} (49%). The XPS peak at 717 eV corresponds to the satellite peak of Fe³⁺. Therefore, it is clear that the MWAST-produced pure phase BFO contains more Fe³⁺ ions than Fe²⁺ ions. A thorough examination of the O 1s XPS spectra of pure BFO (800 W, 8M KOH, 3min) is carried out to study the presence of oxygen vacancies further. According to figure 4.10(c), the O1s peaks have two components as oxygen vacancies frequently contribute another component to the lattice oxygen. The O1s peaks are a superposition of two neighbouring peaks labelled "O₁" and "O₂" and are located at 529.27 and 531.1 eV, respectively. Dual O1s peaks are

frequently found in oxide materials containing cations in various valence states. This suggests that O_2^{2-} ions are prevalent in oxygen-deficient locations while O_1^{2-} ions are abundant in oxygen-rich neighbouring atoms [60]. As a result, the O_2 peak can be attributed to the oxygen vacancies and the O_1 peak to the lattice oxygen [61]. By integrating the intensity of the O_2 peak with the total peak intensity, we determined the percentage of O_1 and O_2 and estimated the values to be 36% for O_2 and 64% for O_1 . Because of this, a thorough study of the XPS data has shown that the oxidation values of Fe and O indicate the presence of extensive oxygen vacancies at ambient temperature and Fe-based impurities.

4.4.7. Dielectric analysis

BFO samples synthesized at 8M KOH, 800W for 3 minutes were measured for their dielectric constants and losses as a function of frequency by applying frequency from 100 Hz-20 MHz, and the response curve obtained was shown in **figure 4.11.** The sample BFO has a high dielectric constant value throughout the frequency range with a low dielectric loss, as can be shown in **figure 4.11(a)**. The significant frequency-dependent dielectric constant is observed at lower frequencies, but tends to decrease as frequency increases. At higher frequencies, the pace of the dielectric constant value decreasing with frequency is seen to be very slow, and at the maximum frequency point, the value achieved its lowest stable value, which is a very common behaviour for all dielectric materials

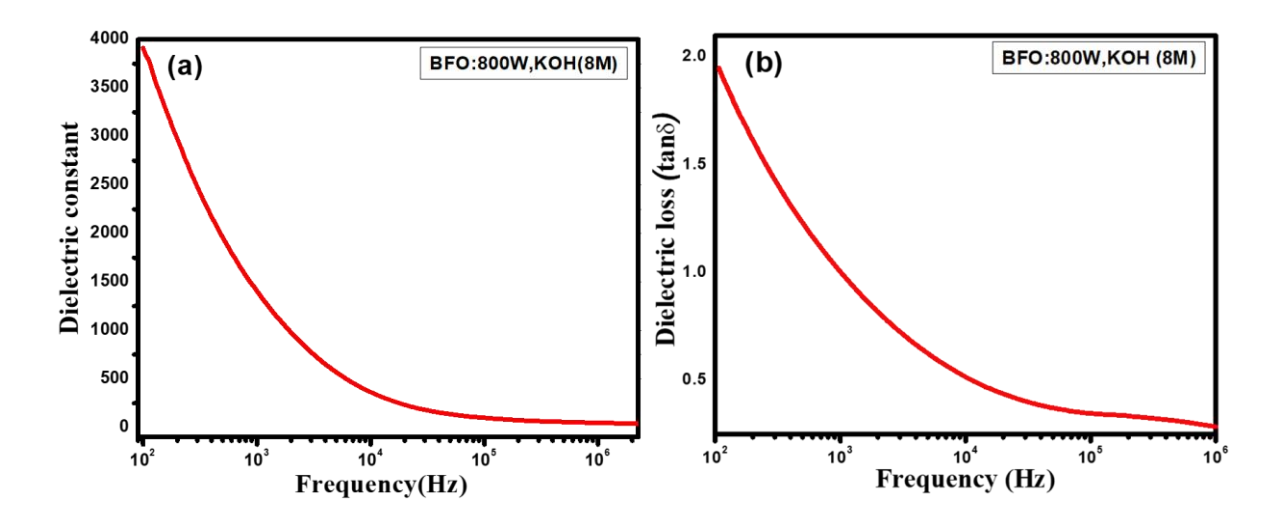


Figure 4.11. Frequency response room temperature (a) Dielectric constant and (b) Dielectric loss of pure phase BFO synthesized with 8M KOH in 3 minutes at 800 W.

Our results are in strong accord with previously published publications, and several researchers have observed similar dielectric behaviour for multiferroic materials [62–63]. The single-phase BFO has a high dielectric constant value (4000) at low frequencies (100 Hz), and its exhibits excellent dielectric values (136) even at higher frequencies (1 MHz), indicating that pure BFO is an excellent dielectric material at higher frequencies. Due to the inverse relationship between dielectric constant and grain boundary thickness, it has been recognised from the literature [64-65] that constituent materials with thin and inhomogeneous grain boundaries are mostly the reason for high dielectric constant values at low frequencies. As a result, as shown, the formation of thin, crystalline flower petals with inhomogeneous grain boundaries and different orientations of grains in **figure 4.5(b)** is the crucial factor in the material's dielectric strength in a low-frequency region. Additionally, due to a rapidly accelerating field, the material reaches an extremum at higher frequency ranges where all the electric dipoles cannot rotate or align. Eventually, the electric polarisation cannot maintain its saturation, which causes a decrease in the dielectric constant [66–67]. Electric dipoles cannot follow the rapid variations in the electric field, so their reduced dielectric constant remains constant at saturation in the higher frequency region [68]. In **figure 4.11(b)**, we can observe the corresponding dielectric dissipation $(tan\delta)$. This study investigated the dielectric loss of the pure phase BFO and showed that it was related to structural homogeneity, stoichiometry, and material compositions [69]. Generally, any dielectric material has a high electrical resistance at low frequencies. This is because of the restricted motion of the electrons from Fe²⁺ to Fe³⁺ ions, which requires a lot of energy to exchange electrons and leads to a high dielectric loss. At low frequencies, pure phase BFO (800W, 8M KOH, 3min) has a high electrical resistance because it has a lot of inhomogeneous grain boundaries. Thus, it takes a lot of energy for electrons to move from Fe^{2+} to Fe^{3+} , so it has a high dielectric loss at low frequencies. Similar to this, at higher frequencies, the pure phase BFO shows low electrical resistance because of the presence of various crystalline petals and, as a result, requires a small amount of energy for electron exchange, implying relatively limited restrictions just on the flow of electrons for a reduced stable dielectric loss in the sample as shown in **figure 11(b)**.

4.4.8. Magnetic Properties

Here, it was examined how a BFO sample synthesized at different microwave powers (300W, 700W, and 800W), 8M KOH, and a constant reaction time of 3 minutes behaved magnetically at room temperature. **Figure 4.12** illustrates the results of our investigation into the magnetic behaviour of BFO samples at room temperature as a function of the applied magnetic field. The sample prepared at 360W exhibited a higher magnetic order (1.51emu/g) than the pure phase BFO prepared at 800W, this is because the sample had a high percentage of impurity phases such as Bi₂₂Fe₂O₃₆, Bi₂₅FeO₄₀, as well as a few magnetic phases like Bi₂Fe₄O₉, and Fe₂O₃, which increased the magnetic order. Compared to pure phase BFO synthesised at 800W, the sample prepared at 700W displayed low magnetic order (0.54emu/g).

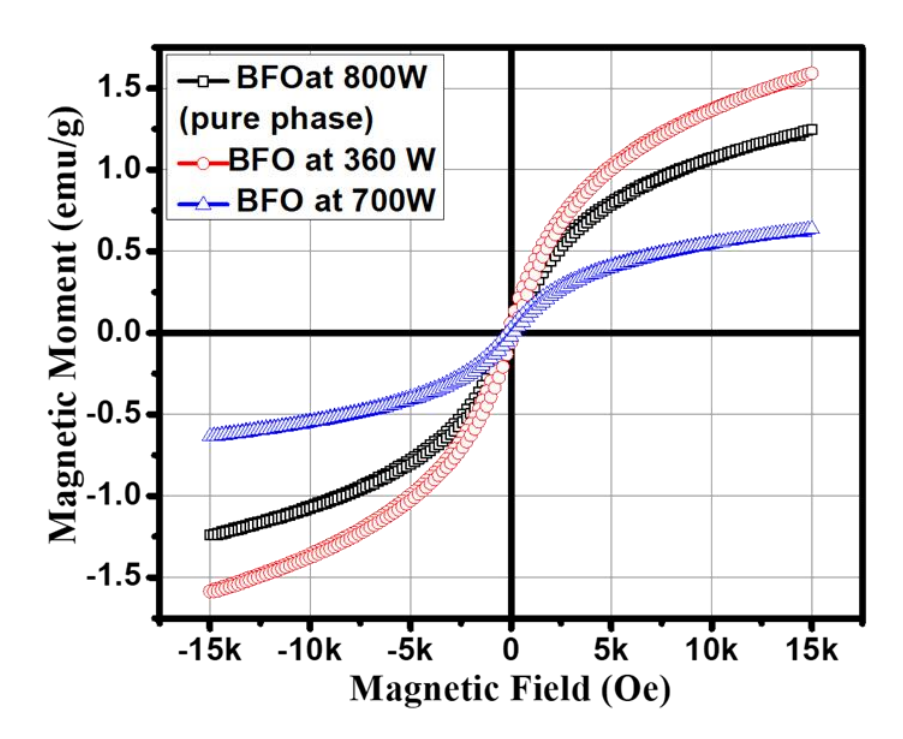


Figure 4.12. The magnetic moment as a function of applied magnetic field for BFO synthesized (8M KOH, 3 min) at different microwave power levels (360, 700, and 800 W).

This difference may result from reduced impurity peaks from magnetic phases like Fe₂O₃, Bi₂Fe₄O₉, and Bi₂₅FeO₄₀, as well as the presence of Bi oxide phases, which significantly influenced the magnetic behaviour and decreased the magnetic order. The pure phase BFO sample synthesized at 800 W exhibits weak ferromagnetic behaviour, which differs from the anti-ferromagnetic behaviour reported for the bulk BFO. It is worth mentioning that pure phase BFO exhibits a high magnetization value of 1.25 emu/g which is the highest

magnetic value reported so far for BFO related to the pure phase BFO synthesized through MWAST in previous works [70-72]. However, the M-H loops did not saturate completely due to the limited applied fields. The field from -1.5T to +1.5T has been applied to our BFO sample to evaluate the magnetisation effect. As a result of the small applied field (i.e., -1.5T to +1.5T), the M-H curve in **figure 4.12** exhibits an unsaturated behaviour. We believe that if the applied field for our BFO sample is increased further, saturated magnetic loops could occur. Our continued research on magnetic behaviour at higher fields has been constrained by the range of applied fields that can be used with our VSM device. The pure phase BFO has a magnetic value of 1.25 emu/g, which is higher than the values thus far recorded [73-74], with a remnant magnetization value of 0.04 emu/g and a low critical field of +171.01 Oe and -159.06 Oe. The single-phase BFO sample exhibits antiferromagnetic and ferromagnetic order, which can be seen in the small changes in two critical magnetic fields. This variation guides establishing an exchange bias characteristic to promote the reposition of coercivity and unidirectional anisotropy. The improvement in the magnetic property of pure phase BFO (800 W, 8M KOH, 3min) is attributed to the particle size effect. The average crystallite size of pure phase BFO is calculated using Debye Scherrer's formula. BFO average particle size is about 26.33 nm, smaller than the spin cycloid structure (62 nm), and also, BFO flowers are composed of a number of thin crystalline petals. Therefore, we believe that when BFO is synthesised as flowers with thin nanopetals, the inhomogeneous spin cycloid structure may be partially destroyed in bulk BFO and exhibit improved magnetic properties in BFO micro flowers [75].

Table 3.4: Different magnetic parameters calculated from magnetic properties of BFO samples synthesized in 3min at different microwave powers with 8M KOH

Samples (BFO)	M _r (emu/g)	M _s (emu/g)	H _c (k Oe)
360 W	0.065	1.51	178.36
700 W	0.027	0.54	217.72
800 W	0.051	1.25	171.01

4.4.8.1. Influence of KOH concentration on magnetic properties of BFO

The room temperature magnetic properties (M-H) of BFO samples synthesized with different KOH concentrations (6M, 8M, 10M, 12M) were examined as a function of the magnetic field (**figure 4.13**). All the BFO samples synthesized at various KOH concentrations (6M, 8M, 10M, and 12M) exhibit poor ferromagnetic properties at room temperature. Compared to BFO synthesised at 10M and 12M KOH, the BFO produced at 6M KOH concentration has demonstrated a high magnetic moment (0.82 emu/g), which may be because Bi₂₅FeO₄₀, Bi₂Fe₄O₉, and Fe₂O₃ magnetic phases are present [**figure 4.4** (**a**)]. The BFO material's magnetic moment value has improved with the rise in KOH concentration from 6M to 8M (1.25emu/g), which can be attributed to the size of the thin petals and homogeneity in the crystalline petals [76].

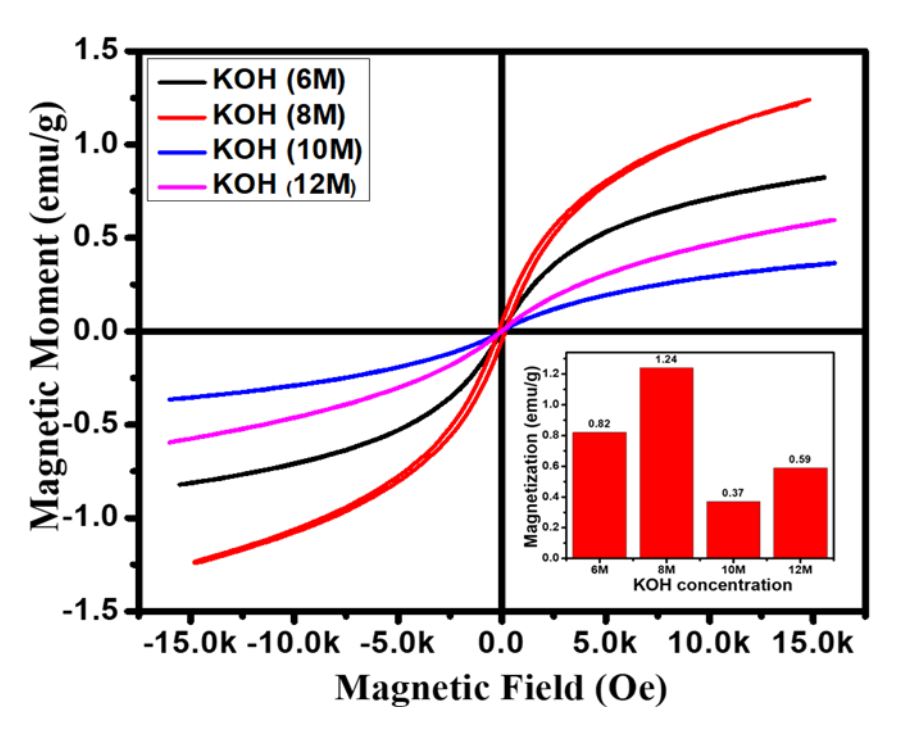


Figure 4.13. The room temperature magnetic behaviour of the BFO micro flowers synthesized with different KOH concentrations (6, 8, 10, and 12M) at 800 W for 3 minutes of microwave heating.

The magnetic moment of the sample was reduced to 0.36 emu/g as the KOH content was raised further from 8M to 10M. As the amount of KOH increased from 8M to 10M, the sample's magnetic moment decreased to 0.36 emu/g. This drop in magnetic value can be explained by phases of impurities like Bi_2O_3 (a weakly magnetic phase) along the pure BFO crystal phase [**figure 4.4(c**)]. Also, the effect of BFO (800 W, 10M, 3 min)

microstructures may reduce the magnetic moment because spherical micro flowers have large size petals on the surface [figure 4.5(c)]. Additionally, it has been discovered that the magnetic moment at 12M KOH is only 0.6 emu/g, which is lower than the magnetic moment of pure phase BFO synthesised at 8M KOH. The nucleation and growth of crystalline petals, which eventually closed the open cages of BFO micro flowers [figure 4.5(b), (d)], are responsible for the reduction in the magnetic moment with a retained pure phase of BFO at 12M KOH. As a result, none of the petals will contribute to the magnetic property.

4.4.9. Ferroelectric properties

The BFO's ferroelectric characteristics were investigated at room temperature after being synthesised at 8M KOH, 800W, and 3 min. **Figure 4.14** demonstrates the obtained P-E hysteresis loops for pure phase BFO at a constant frequency of 100 Hz and variable electric fields between 2 and 25 kV/cm. As we can see from **figure 4.14**, the polarisation value of the material increases with the applied electric field. The highest remnant polarisation (around 15.67 C/cm²) is attained at 25 kV/cm, and the remnant polarisation rises with the applied field.

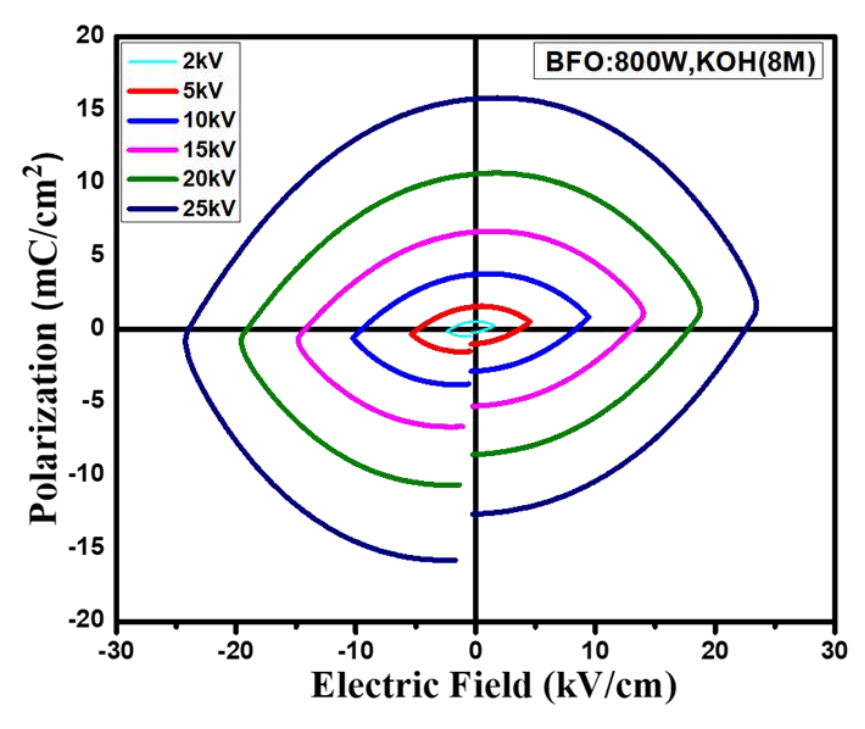


Figure 4.14. P-E Hysteresis loops at a constant frequency (100 Hz) with varying fields of BFO synthesized with 8M KOH in 3 minutes at 800W.

The significant leakage in the sample is attributed to lossy behaviour and unsaturated P-E loops, which may be explained by the ionic moments of Fe³⁺ to Fe²⁺ ions that allow oxygen vacancies to occur [77-80]. As revealed by the XPS data, the presence of Fe²⁺ ions and oxygen vacancies in our pure phase BFO suggests that the material may display a substantial leakage current, which could impact its ferroelectric behaviour at room temperature. Therefore, poor ferroelectric and unsaturated P-E loops, as depicted in **figure 4.14**, can contribute to the large leakage current in the pure phase BFO. To the best of our knowledge, no group has concentrated explicitly on researching the ferroelectric behaviour of pure phase BFO in the prior efforts related to the microwave-assisted hydrothermal synthesis of BFO [81]. We tried to use large electric fields in our experiments to investigate the ferroelectric property of the sample BFO in a wide range of electric fields to obtain the complete well saturated P-E loops. However, we could not reach above 25kV/cm to observe the saturation because of the large leakage current in our sample. Only unsaturated P-E loops were as a result obtained.

4.4.10. Optical properties of pure phase BFO

The optical properties of pure phase BFO produced were examined using a UV-VIS absorption spectrophotometer between 200 and 800 nm. A visible photocatalyst must have a bandgap between 1.23 eV and 3.0 eV and be able to absorb visible light. In **figure 4.15**, the pure phase BFO shows a significant absorption peak at 550 nm, which indicates that it is a visible photocatalyst. The peak broadness reveals the material's extraordinary ability to absorb electromagnetic radiation in the visible region. According to **figure 4.15**, the intrinsic transitions for BFO are responsible for a light absorption edge at about 550 nm. The band gap was determined using the traditional Tauc's formula, which states that $(\alpha h\vartheta) = A(h\vartheta - E_g)n$ where h is the photon energy, E_g is the optical energy band gap, n=1/2, 3/2, 2 or 3, and A is a constant. According to the electronic transition responsible for optical absorption, we have considered n=1/2, which permits a direct energy band gap for single phase BFO and thus provides the bandgap energy. We plotted $(\alpha h\vartheta)^2$ as a function of $h\vartheta$ for single-phase BFO and determine its value by extrapolating a tangent line from the resulting slope to obtain the direct bandgap. The bandgap value for our material,

2.25 eV, is the tangent's X-intercept. As a result, multiferroic semiconductor applications could benefit from the pure phase BFO produced in 3 min.

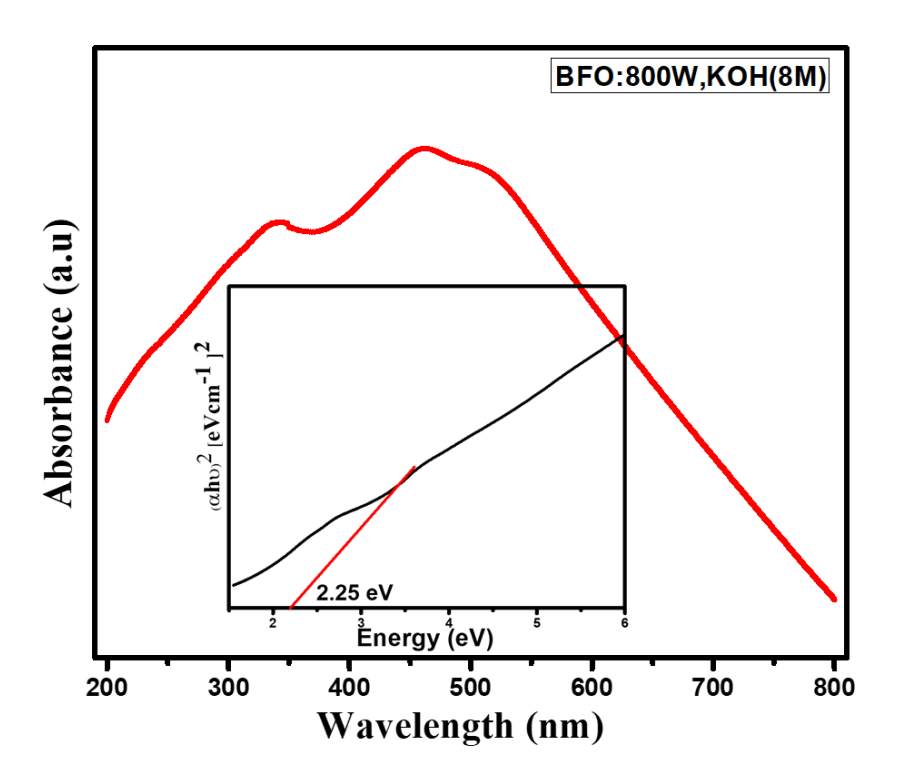


Figure 4.15. UV-Vis-NIR spectroscopy and bandgap of pure phase BFO (800 W, 8M KOH, 3 min).

4.4.11. Photocatalytic activity of pure phase BFO

Performance test for photocatalysis. The photocatalytic performance of pure phase BFO was tested on the photodegradation of Methylene Blue by exposing MB+BFO to heavy sunlight above the solution. To make the solution, 10mg/L of MB was added to distilled water. In the next step, 40 mg of catalyst was added, and the mixture was kept in the sunlight while continuously stirred magnetically. The change in the concentration of MB solution was determined by collecting a sample every 10 minutes and studying its UV and Vis spectra during illumination.

Photodegradation of MB

Figure 4.16 displays time-dependent UV-visible absorbance spectra for the MB captured from 450 to 800 nm while it was exposed to sunlight, followed by periodic sample collection. The intensity of the MB absorption peak at 664 nm declines with time when BFO is used as a photocatalyst, meaning the MB is degrading over time. We have observed the full degradation of the MB was completed within 180 min of sun exposure in the

presence of the BFO catalyst. By using the following equation, the deterioration efficiency is determined.

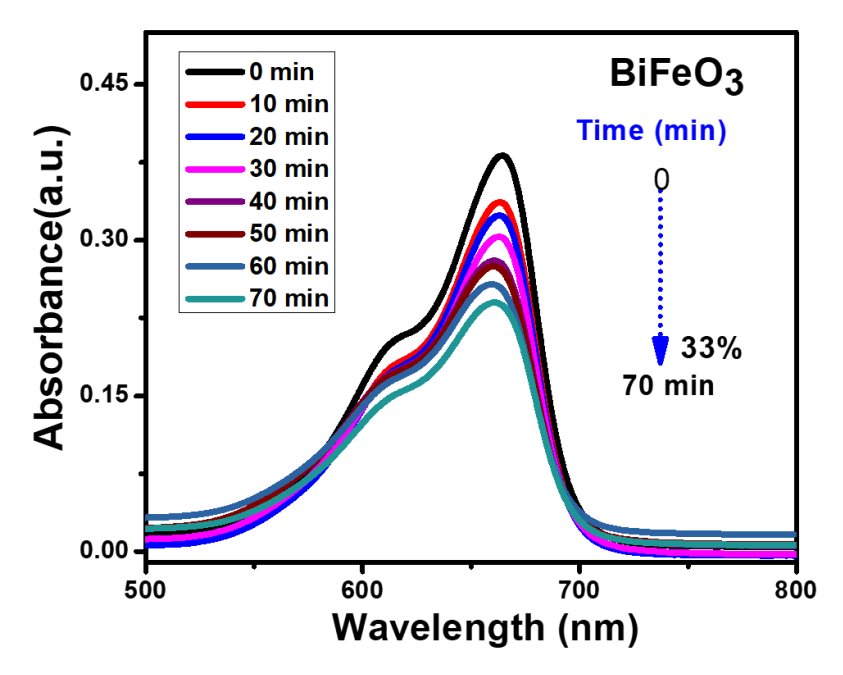


Figure 4.16. Time-dependent UV-Vis spectral changes of MB in the presence of pure phase BFO (800 W, 8M KOH, 3 min).

$$Efficiency = \frac{c_0 - c_t}{c_0} x \ 100$$

Where C_t is the concentration of MB at time t and C₀ is the initial concentration of MB. By replacing those values, we could determine the photocatalytic activity of BFO, which is exhibiting a degradation of 33% in the MB after 180 minutes of intense solar exposure. We found that pure phase BFO synthesised using a microwave-assisted solvothermal approach demonstrated improved degradation efficiency on MB compared to pure phase BFO synthesized using a solvothermal approach in our previous study. This enhanced photocatalytic activity may be attributed to the pure phase BFO's microstructures that pack the nano petals tightly in the micro flowers.

4.5. Conclusion

We have demonstrated the fastest and simplest method to synthesize multiferroic material (BFO) by combining solvothermal and microwave heating. In just 3 minutes, chemical reactants in an ethanol medium can be microwave-irradiated to reach the pure phase of BFO. The overall optimizations were done to study the optimised favourable condition for getting the required pure phase BFO, including microwave power variations (360W, 700W,

800W) and KOH concentration variations (6M, 8M, 10M, 12M) with fixed microwave power (800W). The characterisation findings have confirmed that the pure phase BFO was formed within the shortest time of 3 min at 800 W without impurities. At a high microwave power of 800W for 3 minutes of irradiation with 8M KOH, the morphology and structural studies have revealed remarkable pure phase BFO micro flowers with thin crystalline nano petals on the surface without agglomerations. Our alkaline optimizations lead us to the conclusion that KOH concentrations significantly affect the surface shape of micro flowers. Following XRD, FESEM, and TEM characterizations that confirmed the phase and structural details, the dielectric characteristics were qualitatively examined at room temperature using dielectric spectroscopy. A good frequency response of the dielectric constant with a moderate loss has been demonstrated by the pure phase BFO. The effect of microwave power and KOH concentration on magnetic characteristics were also examined with VSM analysis (magnetic hysteresis), and it was found that pure phase BFO (800W, 8M KOH, 3 min) with the highest value of magnetization of 1.25emu/g had a weak ferromagnetic order. The large leakage current in the pure phase BFO material was caused by the creation of oxygen vacancies and the presence of Fe²⁺ oxidation state, which were revealed by the XPS analysis of pure phase BFO. After that, we investigated the pure phase BFO from P-E hysteresis for its ferroelectric behaviour and verified its poor ferroelectric behaviour with the applied electric field. From UV-Vis absorption spectroscopy, it has been observed that the pure phase BFO has excellent light absorption in the visible range with the bandgap of 2.25eV, revealing its capabilities for photocatalysis application in the visible range. MWAST enabled us to make the potential multiferroic candidate (BFO) with intriguing microstructures and enhanced magnetic and ferroelectric properties in one minute. Compared to the photocatalytic performance (10% MB degradation) of pure phase BFO synthesized by the solvothermal method, pure phase BFO synthesized through MWAST exhibited improved photodegradation efficiency (33% MB degradation).

Supplementary Information

XRD of BFO synthesized by the commercial microwave oven, domestic microwave oven and microwave acid digestion vessel (Model:4782) used for the present work, XRD patterns of BFO synthesized at different Microwave powers and durations.

REFERENCES

- 1. Eerenstein, W., Mathur, N.D., Scott, J.F. 2006. Multiferroic and magnetoelectric materials. *Nature*. 442(7104), 759-765.
- 2. Catalan, G., Scott, J.F. Physics and applications of bismuth ferrite. 2009. *Mater*. 21(24), 2463-2485.
- 3. Irfan, S., Zhuanghao, Z., Li, F., Chen, Y.X., Liang, G.X., Luo, J.T., Ping, F. 2019. Critical review: bismuth ferrite as an emerging visible light active nanostructured photocatalyst. *J. Mater. Res. Technol.* 8(6), 6375-6389.
- 4. Wang, N., Luo, X., Han, L., Zhang, Z., Zhang, R., Olin, H., Yang, Y. 2020. Structure, performance, and application of BiFeO₃ nanomaterials. *Nano-Micro Lett.* 12(1), 1-23.
- 5. Pooladi, M., Sharifi, I, Behzadipour, M. A review of the structure, magnetic and electrical properties of bismuth ferrite (Bi₂Fe₄O₉). 2020. *Ceram. Int.* 46(11), 18453-18463.
- 6. Dhak, D., Hong, S., Das, S., Dhak, P. 2015. Synthesis, characterization, properties, and applications of nanosized ferroelectric, ferromagnetic, or multiferroic materials. *J. Nanomater.* 2015.
- 7. Wang, S.; Chen, D., Niu, F., Zhang, N., Qin, L., Huang, Y. 2016. Hydrogenation-induced surface oxygen vacancies in BiFeO₃ nanoparticles for enhanced visible light photocatalytic performance. *J. Alloys Compd.* 688, 399-406.
- 8. Bernardo, M.S., Jardiel, T., Peiteado, M., Caballero, A.C., Villegas, M. 2011. Reaction pathways in the solid-state synthesis of multiferroic BiFeO₃. *J. Eur. Ceram. Soc.* 31(16), 3047-3053.
- 9. Vinayakumar, K.B, Nagaraja, K.K. 2020. Magnetoelectric coupling in Bismuth Ferrite—challenges and perspectives. *Coatings*. *10*(12), 1221.
- 10. Wang, Y.P., Zhou, L., Zhang, M.F., Chen, X.Y., Liu, J.M., Liu, Z.G. 2004. Room-temperature saturated ferroelectric polarization in BiFeO₃ ceramics synthesized by rapid liquid phase sintering. *Appl. Phys. Lett.* 84(10), 1731-1733.
- 11. Pradhan, A.K.; Zhang, K., Hunter, D., Dadson, J.B., Loiutts, G.B., Bhattacharya, P., Katiyar, R., Zhang, J., Sellmyer, D.J., Roy, U.N et.al. 2005. Magnetic and electrical properties of single-phase multiferroic BiFeO₃. *J.Appl.phys.* 97(9), 093903.

- 12. Ghosh, S., Dasgupta, S., Sen, A., Sekhar Maiti, H. 2005. Low-temperature synthesis of nanosized bismuth ferrite by soft chemical route. *J. Am. Ceram. Soc.* 88(5), 1349-1352.
- 13. Chybczyńska, K., Ławniczak, P., Hilczer, B., Łęska, B., Pankiewicz, R., Pietraszko, A., Kępiński, L., Kałuski, T., Cieluch, P., Matelski, F et al. 2014. Synthesis and properties of bismuth ferrite multiferroic flowers. *J. Mater. Sci.* 49(6), 2596-2604.
- 14. Chybczyńska, K., Ławniczak, P., Hilczer, B., Łęska, B., Pankiewicz, R., Pietraszko, A., Kępiński, L., Kałuski, T., Cieluch, P., Matelski, F et al. 2014. Synthesis and properties of bismuth ferrite multiferroic flowers. *J. Mater. Sci.* 49(6), 2596-2604.
- 15. Cao, X., Lu, Q., Xu, X., Yan, J., Zeng, H. Single-crystal snowflake of Cu₇S₄: 2008. Low temperature, large scale synthesis and growth mechanism. *Mater. Lett.* 62(17-18), 2567-2570.
- 16. Dong, L., Chu, Y., Liu, Y., Li, M., Yang, F., Li, L. 2006. Surfactant-assisted fabrication PbS nanorods, nanobelts, nanovelvet-flowers and dendritic nanostructures at lower temperature in aqueous solution. *J. Colloid Interface Sci.* 301(2), 503-510.
- 17. Yao, W.T., Yu, S.H., Liu, S.J., Chen, J.P., Liu, X.M., Li, F.Q. 2006. Architectural control syntheses of CdS and CdSe nanoflowers, branched nanowires, and nanotrees via a solvothermal approach in a mixed solution and their photocatalytic property. *J. Phys. Chem. B.* 110(24), 11704-11710.
- 18. Yan, C., Xue, D., Zou, L., Yan, X, Wang, W. 2005. Preparation of magnesium hydroxide nanoflowers. J. Cryst. Growth. 282(3-4), 448-454.
- 19. Tong, Y., Liu, Y., Dong, L., Zhao, D., Zhang, J., Lu, Y., Shen, D., Fan, X. 2006. Growth of ZnO nanostructures with different morphologies by using hydrothermal technique. *J. Phys. Chem. B*, *110*(41), 20263-20267.
- 20. Lorkiewicz, J., Nietubyć, R., Barlak, M., Mirowski, R., Bartnik, A., Kostecki, J., Sekutowicz, J., Malinowska, A., Kneisel, P., Witkowski, J. 2014. Deposition and optimization of thin lead layers for superconducting accelerator photocathodes. *Phys.Scr.* 2014(T161), 014071.
- 21. Brooks, D.J., Douthwaite, R.E. 2004. Microwave-induced plasma reactor based on a domestic microwave oven for bulk solid-state chemistry. *Rev. Sci. Instrum.* 75(12), 5277-5279.
- 22. Guo, L., Luo, H., Gao, J., Guo, L., Yang, J. 2006. Microwave hydrothermal synthesis of barium titanate powders. *Mater. Lett.* 60(24), 3011-3014.

- 23. Pązik, R., Hreniak, D., Stręk, W. 2007. Microwave driven hydrothermal synthesis of Ba1-xSrxTiO₃ nanoparticles. *Mater. Res. Bull.* 42(7), 1188-1194.
- 24. Komarneni, S., Menon, V.C., Li, Q.H., Roy, R., Ainger, F. 1996. Microwave-hydrothermal processing of BiFeO₃ and CsAl₂PO₆. *J. Am. Ceram. Soc.* 79(5), ss1409-1412.
- 25. Komarneni, S., Li, Q.H., Roy, R. 1996. Microwave-hydrothermal processing of layered anion exchangers. *J. Mater. Res*, *11*(8), 1866-1869.
- 26. Komarneni, S., Menon, V.C., Li, Q.H., Roy, R., Ainger, F. 1996. Microwave-hydrothermal processing of BiFeO₃ and CsAl₂PO₆. *J. Am. Ceram. Soc.* 79(5), 1409-1412.
- 27. Li, S., Nechache, R., Davalos, I.A.V., Goupil, G., Nikolova, L., Nicklaus, M., Laverdiere, J., Ruediger, A., Rosei, F. 2013. Ultrafast microwave hydrothermal synthesis of BiFeO₃ nanoplates. *J. Am. Ceram. Soc.* 96(10), 3155-3162.
- 28. Zhu, Y.J., Chen, F. 2014. Microwave-assisted preparation of inorganic nanostructures in liquid phase. *Chem. Rev*, 114(12), 6462-6555.
- 29. Joshi, U.A., Jang, J.S., Borse, P.H., Lee, J.S. 2008. Microwave synthesis of single-crystalline perovskite Bi FeO₃ nanocubes for photoelectrode and photocatalytic applications. *Appl. Phys. Lett*, 92(24), 242106.
- 30. Biasotto, G., Simões, A.Z., Foschini, C.R., Antônio, S.G., Zaghete, M.A., Varela, J.A. 2011. A novel synthesis of perovskite bismuth ferrite nanoparticles. *Process. Appl. Ceram*, *5*(3), 171-179.
- 31. Chybczyńska, K., Ławniczak, P., Hilczer, B., Łęska, B., Pankiewicz, R., Pietraszko, A., Kępiński, L., Kałuski, T., Cieluch, P., Matelski, F., Andrzejewski, B. 2014. Synthesis and properties of bismuth ferrite multiferroic flowers. *J. Mater. Sci.* 49(6), 2596-2604.
- 32. . Cao, W., Chen, Z., Gao, T., Zhou, D., Leng, X., Niu, F., Zhu, Y., Qin, L., Wang, J., Huang, Y. 2016. Rapid synthesis of single-phase bismuth ferrite by microwave-assisted hydrothermal method. *Mater. Chem. Phys*, 175, 1-5.
- 33. Zhang, H.J., Liu, L.Z., Zhang, X.R., Zhang, S., Meng, F.N. 2019. Microwave-assisted solvothermal synthesis of shape-controlled CoFe₂O₄ nanoparticles for acetone sensor. J. Alloys Compd. 788, 1103-1112.
- 34. Zhu, Y.J., Chen, F. 2014. Microwave-assisted preparation of inorganic nanostructures in liquid phase. *Chem. Rev.* 114(12), 6462-6555.

- 35. Gedye, R.N., Smith, F.E., Westaway, K.C. 1988. The rapid synthesis of organic compounds in microwave ovens. *Can. J. Chem.* 66(1), 17-26.
- 36. Catalan, G, Scott, J.F. 2009. Physics and applications of bismuth ferrite. *Adv. Mater*, 21(24), 2463-2485.
- Ponzoni, C., Rosa, R., Cannio, M., Buscaglia, V., Finocchio, E., Nanni, P., Leonelli,
 C. 2013. Optimization of BFO microwave-hydrothermal synthesis: Influence of process parameters. *J. Alloys Compd.* 558,150-159.
- 38. Dhanalakshmi, B., Pratap, K., Rao, B.P., Rao, P.S. 2016. Effects of Mn doping on structural, dielectric and multiferroic properties of BiFeO₃ nanoceramics. J. Alloys Compd. 676, 193-201.
- 39. Dhanalakshmi, B., Pratap K., Parvatheeswara Rao B., SubbaRC Rao, P.S.V. 2016. Effects of Mn doping on structural, dielectric and multiferroic properties of BiFeO₃ nanoceramics. *J. Alloys. Compd.* 676, 193-201.
- 40. Gao, T., Chen, Z., Huang, Q., Niu, F., Huang, X., Qin, L., and Huang, Y. A. 2015. review: preparation of bismuth ferrite nanoparticles and its applications in visible-light induced photocatalyses. *Rev. adv. mater. Sci.* 40(2), 97-109.
- 41. Remya, K.P., Prabhu, D., Joseyphus, R.J., Bose, A.C., Viswanathan, C., Ponpandian, N. 2020. Tailoring the morphology and size of perovskite BiFeO₃ nanostructures for enhanced magnetic and electrical properties. *Mater. Des.* 192, 108694.
- 42. Chybczyńska, K., Ławniczak, P., Hilczer, B., Łęska, B., Pankiewicz, R., Pietraszko, A., Kępiński, L., Kałuski, T., Cieluch, P., Matelski, F et al. 2014. Synthesis and properties of bismuth ferrite multiferroic flowers. *J. Mater. Sci.* 49(6), 2596-2604.
- 43. Chybczyńska, K., Ławniczak, P., Hilczer, B., Łęska, B., Pankiewicz, R., Pietraszko, A., Kępiński, L., Kałuski, T., Cieluch, P., Matelski, F et al. 2014. Synthesis and properties of bismuth ferrite multiferroic flowers. *J. Mater. Sci.* 49(6), 2596-2604.
- 44. Dhanalakshmi, B., Pratap K., Parvatheeswara Rao B., Subba Rao, P.S.V. 2016. Effects of Mn doping on structural, dielectric and multiferroic properties of BiFeO₃ nanoceramics. *J. Alloys. Compd.* 676, 193-201.
- 45. Chybczyńska, K., Ławniczak, P., Hilczer, B., Łęska, B., Pankiewicz, R., Pietraszko, A., Kępiński, L., Kałuski, T., Cieluch, P., Matelski, F et al. 2014. Synthesis and properties of bismuth ferrite multiferroic flowers. *J. Mater. Sci.* 49(6), 2596-2604.

- 46. Rao, G.S., Rao, C.N.R., Ferraro, J.R. 1970. Infrared and electronic spectra of rare earth perovskites: ortho-chromites, -manganite's and-ferrites. *Appl. Spectrosc.* 24(4), 436-445.
- 47. Zhang, S.T., Lu, M.H., Wu, D., Chen, Y.F., Ming, N.B. 2005. Larger polarization and weak ferromagnetism in quenched BiFeO₃ ceramics with a distorted rhombohedral crystal structure. *Appl. Phys. Lett.* 87(26), 262907.
- 48. Cao, W., Chen, Z., Gao, T., Zhou, D., Leng, X., Niu, F., Zhu, Y., Qin, L.; Wang, J.; Huang, Y. 2016. Rapid synthesis of single-phase bismuth ferrite by microwave-assisted hydrothermal method. *Mater. Chem. Phys.* 175, 1-5.
- 49. Biasotto, G., Simões, A.Z., Foschini, C.R., Antônio, S.G., Zaghete, M.A., Varela, J.A. 2011. A novel synthesis of perovskite bismuth ferrite nanoparticles. *Process. Appl. Ceram.* 5(3), 171-179.
- 50. Hermet, P., Goffinet, M., Kreisel, J., Ghosez, P. 2007. Raman and infrared spectra of multiferroic bismuth ferrite from first principles. *Phys. Rev.* 75(22), 220102.
- 51. Verma, R., Chauhan, A., Batoo, K.M., Kumar, R., Hadhi, M., Raslan, E.H. 2021. Effect of calcination temperature on structural and morphological properties of bismuth ferrite nanoparticles. *Ceram. Int.* 47(3), 3680-3691.
- 52. Pillai, S., Bhuwal, D., Shripathi, T., Shelke, V. 2013. Synthesis of single-phase bismuth ferrite compound by reliable one-step method. *J. Mater. Sci.: Mater. Electron.* 24(8), 2950-2955.
- 53. Huang, F., Lu, X., Wang, Z., Lin, W., Kan, Y., Bo, H., Cai, W., Zhu, J. 2009. Impact of annealing atmosphere on the multiferroic and dielectric properties of BiFeO₃/Bi₃. ₂₅La0. 75Ti₃O₁₂ thin films. Appl. Phys. A. *97*(3), 699-704.
- 54. Wen, Z., You, L., Shen, X., Li, X., Wu, D., Wang, J., Li, A. 2011. Multiferroic properties of (Bi1– xPrx) (Fe0. 95Mn0. 05) O3 thin films. *Mater. Sci. Eng. B. 176*(13), 990-995.
- 55. Yamashita, T., Hayes, P. 2008. Analysis of XPS spectra of Fe²⁺ and Fe³⁺ ions in oxide materials. *Appl. Surf. Sci.* 254(8), 2441-2449.
- 56. Pradhan, S.K., Roul, B.K. 2011. Effect of Gd doping on structural, electrical and magnetic properties of BiFeO₃ electroceramic. *J. Phys. Chem. Solids*. 72(10), 1180-1187.

- 57. Wen, Z., You, L., Shen, X., Li, X., Wu, D., Wang, J., Li, A. 2011. Multiferroic properties of (Bi₁- x Pr_x) (Fe _{0.95} Mn_{0.05}) O₃ thin films. *Mater. Sci. Eng. B.* 176(13), 990-995.
- 58. Lin, F., Yu, Q., Deng, L., Zhang, Z., He, X., Liu, A., Shi, W. 2017. Effect of La/Cr codoping on structural transformation, leakage, dielectric and magnetic properties of BiFeO₃ ceramics. *J. Mater. Sci.* 52(12), 7118-7129.
- 59. Zhang, F., Jan, H., Saito, K., Tanaka, T., Nishio, M., Nagaoka, T., Arita, M., Guo, Q. 2015. Toward the understanding of annealing effects on (GaIn) ₂O₃ films. *Thin Solid Films*. *578*, 1-6.
- 60. Li, X., Wang, Y., Liu, W., Jiang, G., Zhu, C. 2012. Study of oxygen vacancies' influence on the lattice parameter in ZnO thin film. *Mater. Lette.* 85, 25-28.
- 61. Zhang, F., Jan, H., Saito, K., Tanaka, T., Nishio, M., Nagaoka, T., Arita, M., Guo, Q. 2015. Toward the understanding of annealing effects on (GaIn) ₂O₃ films. *Thin Solid Films*. *578*, 1-6.
- 62. Singh, N., Agarwal, A., Sanghi, S. 2011. Dielectric relaxation, conductivity behavior and magnetic properties of Mg substituted Zn–Li ferrites. *Curr. Appl. Phys.* 11(3), 783-789.
- 63. Mazen, S.A., Dawoud, H.A. 2003. Temperature and composition dependence of dielectric properties in Li–Cu ferrite. *Mater. Chem. Phys.* 82(3), 557-566.
- 64. Das, P.S., Singh, G.P. 2016. Structural, magnetic and dielectric study of Cu substituted NiZn ferrite nanorod. *J. Magn. Magn. Mater.* 401, 918-924.
- 65. Dhanalakshmi, B., Pratap K., Parvatheeswara Rao B., Subba Rao, P.S.V. 2016. Effects of Mn doping on structural, dielectric and multiferroic properties of BiFeO₃ nanoceramics. *J. Alloys. Compd.* 676, 193-201.
- 66. Kadam, A. A., Shinde, S. S., Yadav, S. P., Patil, P. S., Rajpure, K. Y. 2013. Structural, morphological, electrical and magnetic properties of Dy doped Ni-Co substitutional spinel ferrite. *J. Magn. Magn. Mater.* 329, 59-64.
- 67. Hussain, T., Siddiqi, S.A., Atiq, S., Awan, M.S. 2013. Induced modifications in the properties of Sr doped BiFeO₃ multiferroics. *Prog. Nat. Sci.: Mater. Int.* 23(5), 487-492.
- 68. Rahaman, M.D., Saha, S.K., Ahmed, T.N., Saha, D.K, Hossain, A.A. 2014. Magnetoelectric effect of (1– x) Ba_{0. 5} Sr_{0. 5} Zr_{0. 5} Ti_{0. 5} O₃+ (x) Ni_{0. 12} Mg_{0. 18} Cu_{0. 2}Zn_{0. 5}Fe₂O₄ composites. *J. Magn. Magn. Mater. 371*, 112-120.

- 69. Rao, B.P, Rao, K.H. 1997. Effect of sintering conditions on resistivity and dielectric properties of Ni-Zn ferrites. *J. Mater. Sci.* 32(22), 6049-6054.
- 70. Zhang, X., Sui, Y., Wang, X., Wang, Y., Wang, Z. 2010. Effect of Eu substitution on the crystal structure and multiferroic properties of BiFeO₃. *Appl. Phys. Lett.* 507(1), 157-161.
- 71. Park, T.J., Papaefthymiou, G.C., Viescas, A.J., Moodenbaugh, A.R., Wong, S.S. 2007. Size-dependent magnetic properties of single-crystalline multiferroic BiFeO3 nanoparticles. *Nano Lett.* 7(3), 766-772.
- 72. Zhang, S.T., Lu, M.H., Wu, D., Chen, Y.F., Ming, N.B. 2005. Larger polarization and weak ferromagnetism in quenched Bi Fe O ₃ ceramics with a distorted rhombohedral crystal structure. *Appl. Phys. Lett.* 87(26), 262907.
- 73. Chybczyńska, K., Ławniczak, P., Hilczer, B., Łęska, B., Pankiewicz, R., Pietraszko, A., Kępiński, L., Kałuski, T., Cieluch, P., Matelski, F et al. 2014. Synthesis and properties of bismuth ferrite multiferroic flowers. *J. Mater. Sci.* 49(6), 2596-2604.
- 74. Li, S., Nechache, R., Davalos, I.A.V., Goupil, G., Nikolova, L., Nicklaus, M., Laverdiere, J., Ruediger, A. Rosei, F. 2013. Ultrafast microwave hydrothermal synthesis of BiFeO₃ nanoplates. *J. Am. Ceram. Soc.* 96(10), 3155-3162.
- 75. Park, T.J., Papaefthymiou, G.C., Viescas, A.J., Moodenbaugh, A.R., Wong, S.S. 2007. Size-dependent magnetic properties of single-crystalline multiferroic BiFeO₃ nanoparticles. *Nano Lett.* 7(3), 766-772.
- 76. Szafraniak-Wiza, I., Andrzejewski, B., and Hilczer, B. 2014. Magnetic properties of bismuth ferrite nanopowder obtained by mechanochemical synthesis. *arXiv* preprint arXiv. 1407, 465
- 77. Rhaman, M. M., Matin, M. A., Hakim, M. A., Islam M. F. 2019. Dielectric, ferroelectric and ferromagnetic properties of samarium doped multiferroic bismuth ferrite. *Mater.Res. Express.* 6(12), 125080.
- 78. Cai, W., Fu, C., Hu, W., Chen, G., Deng, X. 2013. Effects of microwave sintering power on microstructure, dielectric, ferroelectric and magnetic properties of bismuth ferrite ceramics. J. *Alloys Compd.* 554, 64-71.
- 79. Kazhugasalamoorthy, S., Jegatheesan, P., Mohandoss, R., Giridharan, N.V., Karthikeyan, B. Joseyphus, R.J., Dhanuskodi, S. 2010. Investigations on the properties of pure and rare earth modified bismuth ferrite ceramics. *J. Alloys Compd.* 493(1-2), 569-572.

- 80. Lan, C., Jiang, Y., Yang, S. 2011. Magnetic properties of La and (La, Zr) doped BiFeO₃ ceramics. *J. Mater. Sci.* 46(3), pp.734-738.
- 81. Rhaman, M. M., Matin, M. A., Hakim, M. A., Islam M. F. 2019. Dielectric, ferroelectric and ferromagnetic properties of samarium doped multiferroic bismuth ferrite. *Mater.Res. Express.* 6(12), 125080.

Chapter-5

Structural, magnetic and optical properties of BFO-based (1-x) BiFeO₃+xFe₂O₃ heterostructure photocatalysts for photodegradation of organic dye pollutant

Objectives

- ❖ The main objective is synthesizing a BFO + Fe₂O₃ heterostructure to enhance the visible range photocatalytic activity of pure phase BiFeO₃ (produced by microwave-assisted-solvothermal).
- ❖ Ferromagnetic hematite Fe₂O₃ is an excellent visible active photocatalyst with a band gap of 1.9 eV, while our synthesised pure phase BiFeO₃ has a band gap of 2.25 eV, which makes it a poor visible photocatalyst. By doping with Fe₂O₃, we can separate the photogenerated electron-hole pairs, which is an essential factor in increasing the photocatalytic activity of the BFO.
- The novel aspect of the current work is investigating MB (Methylene Blue) photodegradation in the presence of BFO+ Fe₂O₃ photocatalysts in sunlight.

5.1. Introduction

Heterogeneous photocatalysis is challenging because it is difficult to recover and reuse the photocatalysts. Several studies have shown that nano and microparticles with a large surface area are more photo catalytically active [1-2], thus allowing them to spread more easily in an aqueous environment. They efficiently pass the light needed for the caspitalysts to be photoactivated. However, recovering those small particles through filtration or centrifugation typically results in higher operating costs for photocatalyst reuse in subsequent cycles.

Researchers have used an external magnetic field in the past decade to separate magnetized photocatalytic materials from an aqueous phase. A variety of pure and composite materials are widely known, such as single-phase ferromagnetic BiFeO₃, Fe₃O₄/TiO₂, Fe₂O₃/ZnO,

BiFeO₃/SrTiO₃, Fe₂O₃/TiO₂, BiFeO₃/Fe₂O₃ [3-9]. Most of the magnetized materials mentioned above have demonstrated an excellent photocatalytic activity and photocatalytic performance for the degradation of organic pollutants and other dyes, providing a practical means for the rapid recovery of powder (catalyst) from the suspension. Among the oxide semiconductors, BiFeO₃ and Fe₂O₃ have attracted special attention due to their potential application in advanced magnetoelectric devices as well as their role as photocatalysts due to their chemical stability and narrow bandgaps, which could make a significant difference in the absorption of visible light by solar energy over other unstable semiconductors such as GaS, CdS and ZnS [10,11]. Although numerous studies have demonstrated significant photocatalytic activity of BFO and Fe₂O₃, still the photocatalytic performance of the pure phase BFO and Fe₂O₃ is less than other oxide semiconductors visible light-active photocatalysts, such as $BiVO_4[12-13]$, BiOX (X= Cl, I, Br) [14-16], Bi_2O_3 [17-19] due to their narrow energy bandgap, improper optical band positions and high rates of electron and hole recombination [20-22]. Among the beneficial methods for promoting photogenerated electron-hole pairs separation is combining more than one photocatalyst with building a heterostructure photocatalyst system [23-25].

Researchers have developed several composites visible photocatalysts such as CuO/BFO [26], BFO/polymer g-C₃N₄, g-C₃N₄/BFO [27], BaTiO₃/ α -Fe₂O₃[28], core-shell structures Fe₂O₃@CeO₂ [29] over the past decade, and impressive advances have been made in improving the photocatalytic activity. From a fundamental physics perspective, it is essential to embed α -Fe₂O₃ into BiFeO₃. Like the BiFeO₃ system [30], α -Fe₂O₃ possesses a canting antiferromagnetic magnetic state and a rhombohedral crystal shape [31]. Both crystal systems exhibit small optical band gaps (E_{g (BiFeO3)} =2.2–2.8eV [32-33] and E_{g (α -Fe₂O₃) =2.2eV), making them suitable for photocatalysis and photoelectrochemical applications [34]. In addition, a particle's size, strain, and defect impact its magnetic and optical properties [35]. According to literature, γ -Fe₂O₃ and α -Fe₂O₃ in BiFeO₃ increased strain and other physical features like magnetization, while -Fe₂O₃ can be easily incorporated into the matrix of BiFeO₃ [36]. Therefore, BiFeO₃/ α -Fe₂O₃ heterostructures are interesting to study in terms of their structural and physical properties [37].}

In the present work, we aimed to synthesize BFO-based heterostructures [(1-x) BiFeO₃+xFe₂O₃ (x=0.10, 0.20, 0.30)] by loading different ratios of hollow micro spherical Fe₂O₃ onto the BFO micro flowers. Few works are done on the BiFeO₃/Fe₂O₃ heterostructures [38-41]. In contrast to these earlier studies, the novelty of the current work

lies in 1) the use of various Fe₂O₃ loading ratios onto the BFO to identify the best heterostructure with improved photocatalytic activity and recyclability in comparison to the pure phase BFO, and 2) the improved magnetic properties, recyclability, and photocatalytic activity of the prepared heterostructures.

5.2. Experimental Section

5.2.1. Materials

For this procedure, ethanol, double-distilled water (DDW), pure potassium hydroxide (KOH, 98%), pure ferric chloride (FeCl₃.6H₂O, 98%), ferric nitrate nine-hydrate [Fe (NO₃). 9H₂O], mono hydrated citric acid (C₆H₈O₇.H₂O) and pure bismuth chloride (BiCl₃, 98%) are all used.

5.2.2. Preparation of BiFeO₃ micro flowers

The pure phase BFO micro flowers are synthesized in 3min at 800 W by microwave-assisted-solvothermal (MWAST) method in a domestic solo-microwave oven. The complete experimental procedure can be found in our previous work [42] [figure 4. 1].

5.2.3. Preparation of hollow Fe₂O₃ microspheres

Hollow hematite Fe₂O₃ microspheres were synthesized using a modified gas-bubble template method after air annealing. A precursor of iron oxide is produced by the sol-gel method. A colloidal solution of 0.5M Fe (NO₃)₃. 9H₂O and 0.4 M C₆H₈O₇.H₂O were dissolved in 200ml of DDW (double distilled water) and stirred for 72hrs at 80°C. A citric acid solution (0.1M) was added to the above solution to promote hydrolysis and balance any ion imbalances. The formation of a gel occurs through hydrolysis of ferric nitrate into iron oxo hydrate FeOOH. The final gel was then dried at 80°C for 24hrs to evaporate any possible impurities and water residuals formed during the synthesis. Finally, the gel was annealed at 550°C for 24hrs and cooled down to room temperature. As L. de Los Santos Valladares et al. [43] reported, this step has two purposes. The first step is to oxidize the gel to produce pure Fe₂O₃ thermally; the second step is to boil the air to form bubble structures, from which hollow spheres of Fe₂O₃ are produced after quenching.

5.2.4. Synthesis of (1-x) BFO+xFe₂O₃ (x = 0.10, 0.20, 0.30)

(1-x) BFO+xFe₂O₃ heterostructures are prepared by a simple co-precipitation method following the microwave heating at 360 W for 3 min. We dissolved a stoichiometric ratio

of BFO and Fe₂O₃ powders in 40ml of ethanol and sonicated it for six hours at 80°C to evaporate the solvent and obtain the gel. Finally, the gel was heated at 360 W for 3 min in a domestic microwave oven. Following the above procedure, we have synthesized three different series of heterostructures by loading different ratios of Fe₂O₃ onto the BFO. The prepared heterostructures (1-x) BFO+xFe₂O₃, where x = 0.10, 0.20, 0.30 are named as BFOF10, BFOF20, BFOF30, respectively.

5.3. Characterizations

The optical properties of synthesized BFO, Fe₂O₃ and BFO+Fe₂O₃ heterostructures were characterized using UV-Visible spectroscopy (Jasco V-670 UV-Visible double beam spectrophotometer). The absorption spectra were recorded between 200-800nm wavelength ranges. By analysing XRD data (PANalytical, X'Pert Powder Diffractometer), we have confirmed the formation of the pure phases of BFO, Fe₂O₃ and the formation of heterostructures. In this diffractogram, the scanning range was between 20⁰ - 80⁰ (2θ value) at a scan rate of 4°/min, and the step size was 0.02°. Field emission scanning electron microscopy (FESEM: Carl Zeiss Smart Sem) and transmission electron microscopy were used to study the morphology of synthesized samples. A vibrating sample magnetometer measured the magnetic properties of synthesized heterostructures samples at room temperature (VSM, Model: LakeShore).

5.4. Photocatalysis

Using a model pollutant dye Methylene Blue, each prepared sample was assessed for its photocatalytic activity for degrading dye pollutant. Photodegradation was conducted in heavy sunlight. 40mg of each photocatalyst powder was initially added to 100ml of MB solution at a concentration of 0.9g/L and neutral pH. Following the continuous magnetic stirring, the slurry was irradiated with heavy sunlight. We monitored the decolourization of the dye solution using UV-Visible spectroscopy.

5.5. Result and Discussions

5.5.1. X-ray diffraction (XRD) analysis of the heterostructures

Using the chemical coprecipitation method, we created BFO+Fe₂O₃ heterostructures with 10%, 20%, and 30% (mass%) Fe₂O₃ content (BFOF10), BFOF20, and BFOF30, respectively. The XRD patterns of BFO, Fe₂O₃, and BFO+Fe₂O₃ heterostructures are displayed in **figure 5. 1**. According to XRD analysis, the BFO exhibited Rhombohedral

crystal structures with the R_{3c} space group, which is in perfect agreement with the previous crystallographic data (ICSD 98-019-1940), exhibiting no secondary phases.

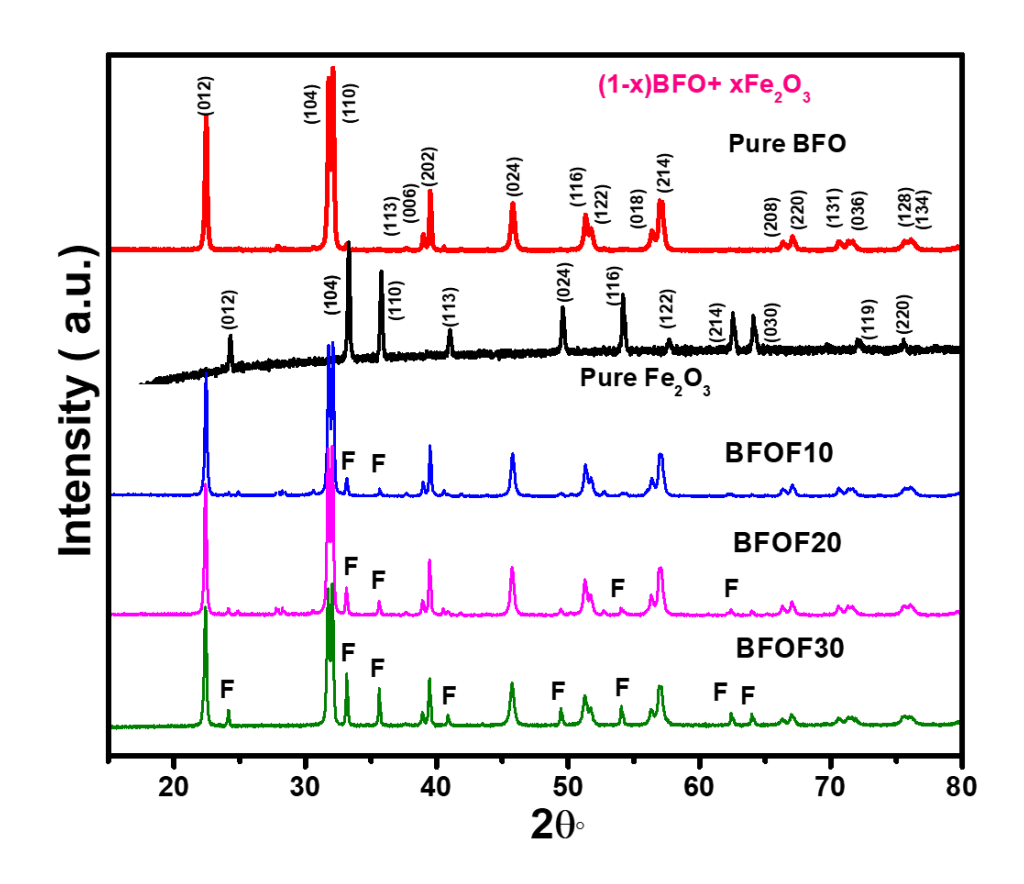


Figure 5.1. XRD patterns of a) pure BFO, b) pure Fe₂O₃, c) BFOF10, d) BFOF20, and d) BFOF30.

It was determined that the Fe₂O₃ XRD pattern showed Rhombohedral symmetry (R_{3c} space group, ICSD: 98-005-6372). After adding 10% of Fe₂O₃ (BFOF10), the XRD patterns showed all peaks corresponding to pure phase BFO with a slight trace of the two prominent peaks (104,110) of Fe₂O₃. As the Fe₂O₃ loading ratio increased to 20% (BFOF20), more Fe₂O₃ peaks appeared. In particular, the increased intensity of the two most intense Fe₂O₃ peaks found at about 33.38 and 35.83°, corresponding to (104) and (110) crystal orientations, confirms the higher Fe₂O₃ content. Finally, after loading 30% Fe₂O₃, the heterostructure sample BFOF30 presents all the Fe₂O₃ peaks besides the diffraction pattern corresponding to pure BFO. Therefore, from the XRD analysis, it has been confirmed the formation of BFO+Fe₂O₃ heterostructures without forming any secondary phases.

5.5.2. FE-SEM images of heterostructures

As shown in the **figure. 5.2**, FE-SEM was used to analyze the microstructures of the BFO+Fe₂O₃ heterostructures. **Figure 5.2(a)** shows that pure phase BFO powder was composed of a large number of BFO micro flowers where hundreds of BFO nano petals were closely packed on the BFO micro flowers [44]. Microstructures of pure phase Fe₂O₃ are shown in figure **5.2(b)**, confirming the formation of hollow Fe₂O₃ microspheres. As illustrated in **figures 5.2(c)**, **(d)**, and**(e)**, the microstructure of the BFO+Fe₂O₃ heterostructure is drastically altered after BFO is loaded by different molar ratios of Fe₂O₃ hollow microspheres.

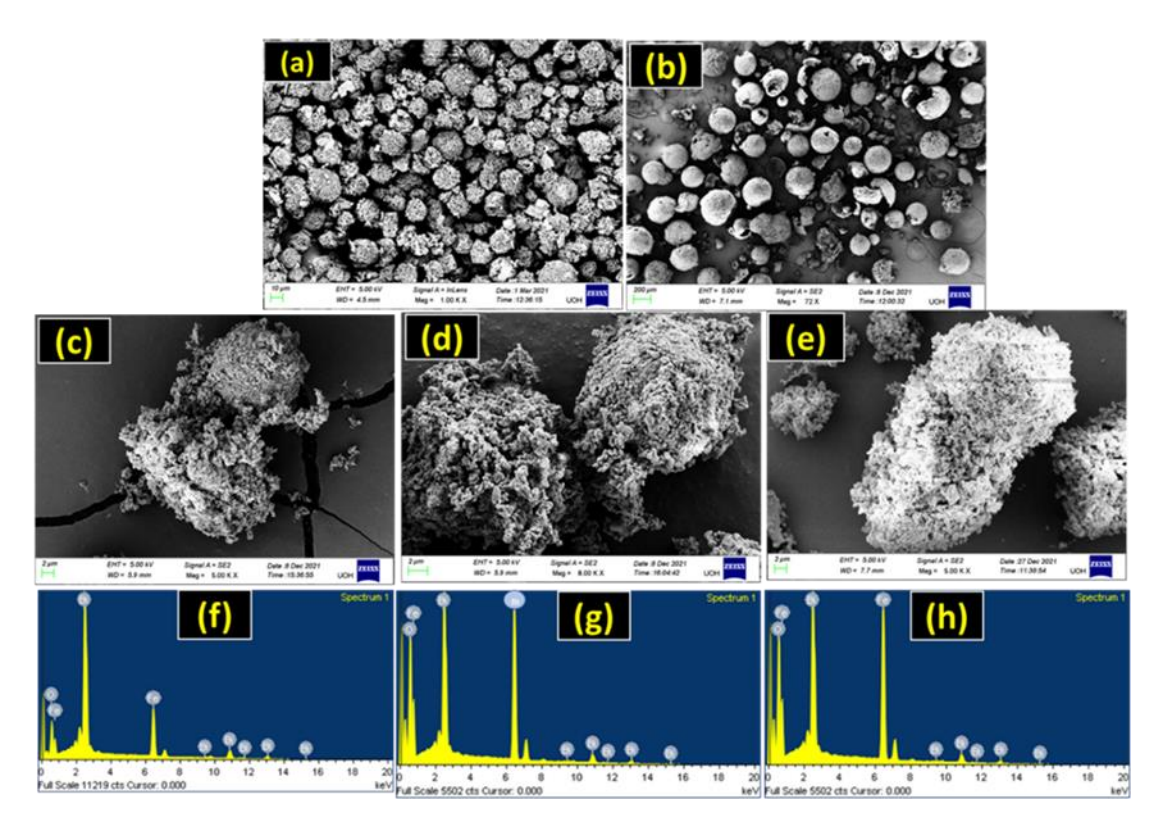


Figure 5.2. FE-SEM of a) pure BFO, b) pure Fe₂O₃, c) BFOF10, d) BFOF20, and e) BFOF30 and EDAX spectrum of f) BFOF10, g) BFOF20, and h) BFOF30.

It is worth mentioning that after heating the BFO+Fe₂O₃ heterostructures with high microwave energies (350 W, 3min), both BFO micro flowers and hollow Fe₂O₃ microspheres were destroyed. From **figure 5.2(c)**, it can be seen that there is partial contact between the BFO and Fe₂O₃ phases. It is believed that the destroyed nano petals from BFO micro flowers are entered into the hollow Fe₂O₃ microspheres and made coupling between the BFO and Fe₂O₃ phases, which is a crucial factor for enhancing the photocatalytic

activity. As the amount of Fe₂O₃ increases, the contact between both phases increases, as shown in **figure 5.2(d, e)**. The EDAX spectra of BFOF10, BFOF20, and BFOF30 has shown in **figure 5.2(f, g, and h)**. It is proven that the Bi, Fe, and O components are the source of the signal peaks, indicating that Fe₂O₃ was successfully loaded onto the BFO.

5.5.3. Optical properties of BFO+Fe₂O₃ heterostructures

The UV-Vis absorption spectrum of all the prepared samples is shown in **figure 5.3**. Each sample demonstrated an excellent visible light absorption that matches extremely well with the majority of the UV-Vis spectra of single phase Fe₂O₃ and their heterostructures that have been published [45-46]. All three heterostructures (BFOF10, BFOF20, and BFOF30) have displayed excellent optical absorption in the visible range, demonstrating their suitability for the visible photodegradation of organic dyes.

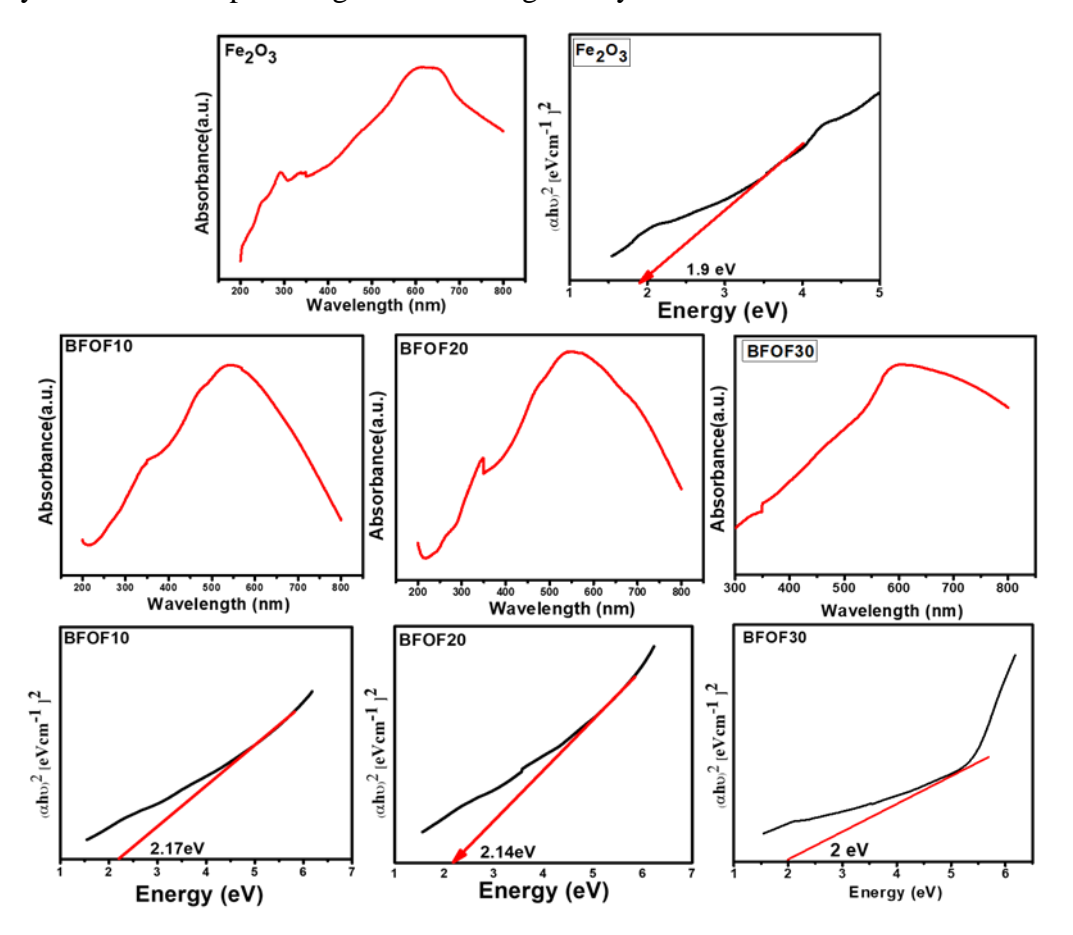


Figure 5.3. UV-Vis's absorption spectroscopy and energy band gap of Fe_2O_3 , BFOF10, BFOF20, and BFOF30.

The absorption of light at the visible spectral range from 500-800nm increased as the amount of Fe₂O₃ increased, revealing the visible light absorbance of these heterostructures

improved more than the pure phase BFO. The obtained band energies of these heterostructures BFOF10 (570 nm), BFOF20 (579 nm), and BFOF30 (620 nm) were 2.17, 2.14, and 2.0 eV. According to the results of the bandgap studies, the energy band gap of these heterostructures is smaller than that of the pure phase BFO (**figure. 4.15**), which might be because two semiconductors' interfaces combine two different energy band gaps. From this study, it has been observed that BFOF30 has a higher absorption of light in the visible range with a lower bandgap compared to the other two (BFOF10 and BFOF20) and is expected to produce a higher number of photogenerated electron holes. The optical band edges were calculated from Tauc's plot, which is given below:

$$(\alpha h\vartheta) = A(h\vartheta - E_g)n$$

 α is the absorption coefficient, E_g represents the energy band gap, A is constant, and depending on transition, we have to consider n values

direct permitted transitions, n = 1/2

direct forbidden transitions, n = 3/2.

permitted indirect transitions, n = 2.

indirect prohibited transitions, n = 3.

Table 5.1. Band energies obtained from optical property studies

S. No	Sample	The band gap (eV)
1	BFO (figure 4. 15)	2.25
2	Fe ₂ O ₃	1.9
3	BFOF10	2.17
4	BFOF20	2.14
5	BFOF30	2.0

5.5.4. Photocatalytic activity of BFO+Fe₂O₃ heterostructures

Figure 5.4 displays the photocatalytic capabilities of BFO, Fe₂O₃, and BFO+Fe₂O₃ heterostructures under heavy sunlight. The full degradation of MB for the BFO, Fe₂O₃(65%), and BFO+Fe₂O₃ heterostructure took 70 minutes to complete. After adding 10% Fe₂O₃ [BFOF10], we observed less degradation (72%) in the MB solution when compared to the other two heterostructures [BFOF20, BFOF30]. The efficiency was

increased for the BFOF20 and BFOF30 samples, and after only 70 minutes, 86 and 94% of the deterioration had occurred, respectively. The increased photocatalytic performance of the samples BFOF20 and BFOF30 demonstrate how efficiency increased for higher concentrations of Fe₂O₃. The heterostructure's microstructural characteristics may cause this improvement in photodegradation efficiency.

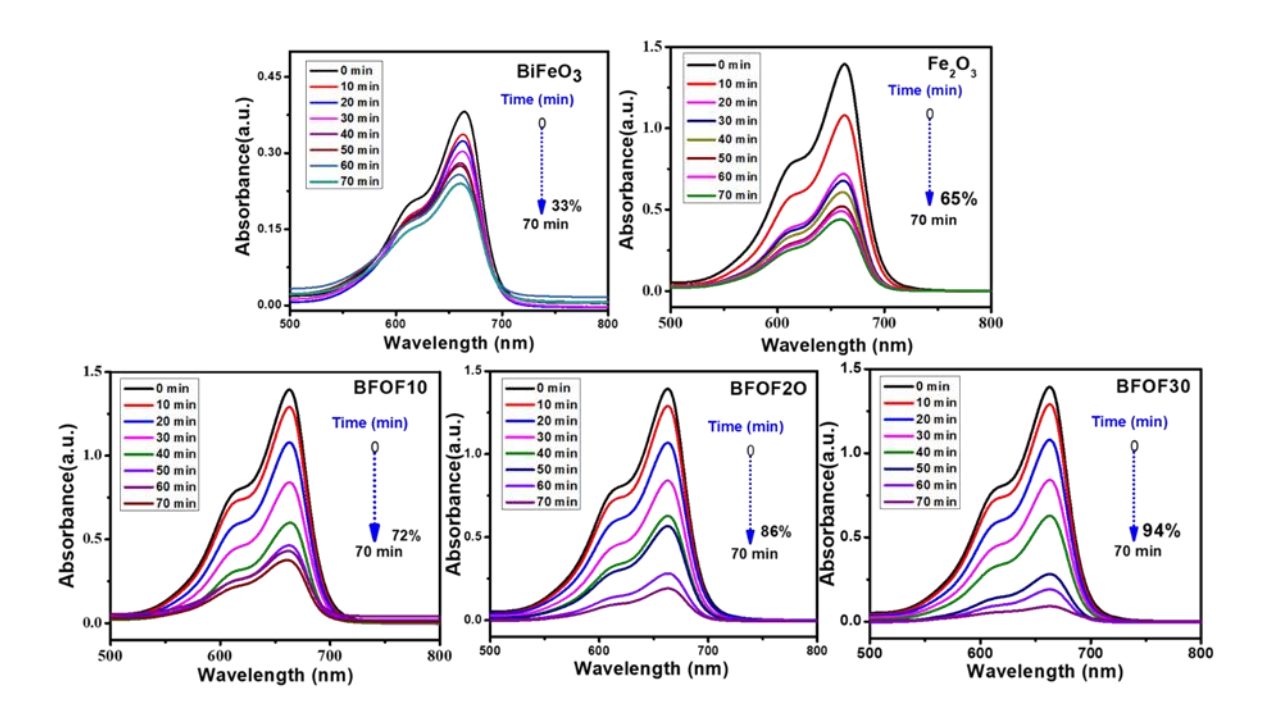


Figure 5.4. Time dependant UV-Vis spectral changes of Methylene Blue in the presence of BFO, Fe₂O₃, BFOF10, BFOF20, BFOF30, and MB colour after the complete degradation.

The BFO surface is entirely coupled with Fe₂O₃ in this situation (BFOF20 and BFOF30), making it easier for the light to form electron-hole pairs at the BFO+Fe₂O₃ surface, even though the band gaps of BFOF20 and BFOF30 are narrower than of the pure BFO sample. As a result, their efficiency is improved. This photodegradation test demonstrates excellent results for the rapid photodegradation efficiency of heterostructures compared to pure phase BFO, demonstrating these heterostructures' abilities to degrade MB in sunlight. The equation for calculating the performance of the photocatalyst is given below. C₀ is an initial concentration of MB, and C_t is the concentration at time t.

$$Efficiency = \frac{C_0 - C_t}{C_0} x \ 100$$

5.5.5. Effect of Photocatalyst concentration on efficiency

The degradation of MB dye was carried out at a constant dosage of 10 mg/500 ml using different heterostructures BFOF10, BFOF20, and BFOF30 catalyst dosages (10, 20, 30 and 40 mg). The catalyst dosage, the initial dosage of dye, type of dye, pH value of dye, and most microstructures of the catalysts were all factors that affected the dye degradation. **Figure 5.5** shows that MB's photodegradation efficiency decreases as the catalyst concentration decreases [all the obtained values are depicted in **table 5.2**], indicating that the photodegradation efficiency strongly depends on the catalyst concentration. It is well known from the literature that photodegradation efficiency strongly depends on the microstructures, pH values, initial concentration of dye, etc.

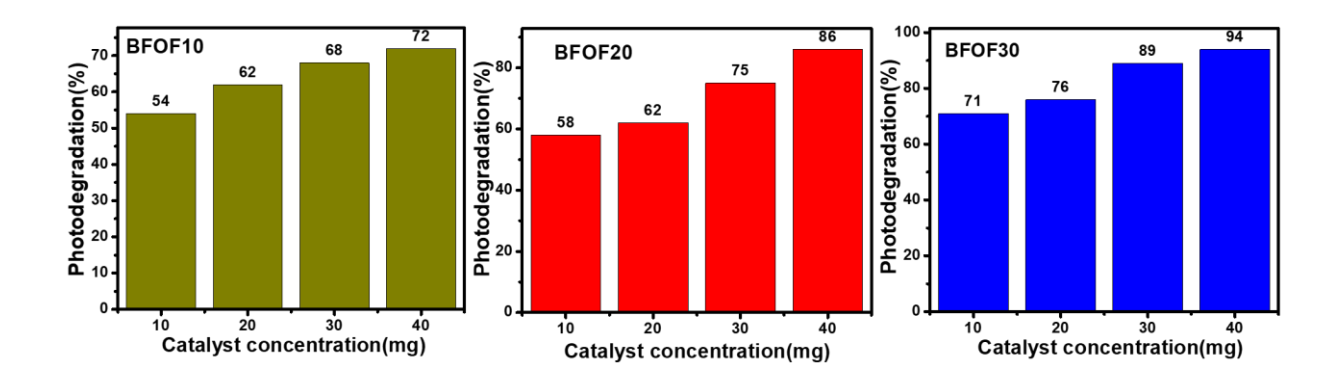


Figure 5.5. Effect of photocatalyst dosage on photodegradation efficiency of heterostructures BFOF10, BFOF20, and BFOF30.

Table 5.2. Influence of catalyst dosage (mg) on Photodegradation (%)

Dye Name	Catalyst name	Catalyst dosage (mg)	Time (min)	Degradation (%)
MB	BFOF10	10	70	54
		20	70	62
		30	70	68
		40	70	72

MB	BFOF20	10	70	58
		20	70	62
		30	70	75
		40	70	86
MB	BFOF30	10	70	71
		20	70	76
		30	70	89
		40	70	94

5.5.6. Stability and Magnetic recovery of Photocatalysts

The catalyst stability of the most active powders, BFOF20 and BFOF30, was investigated by recycling them for four cycles.

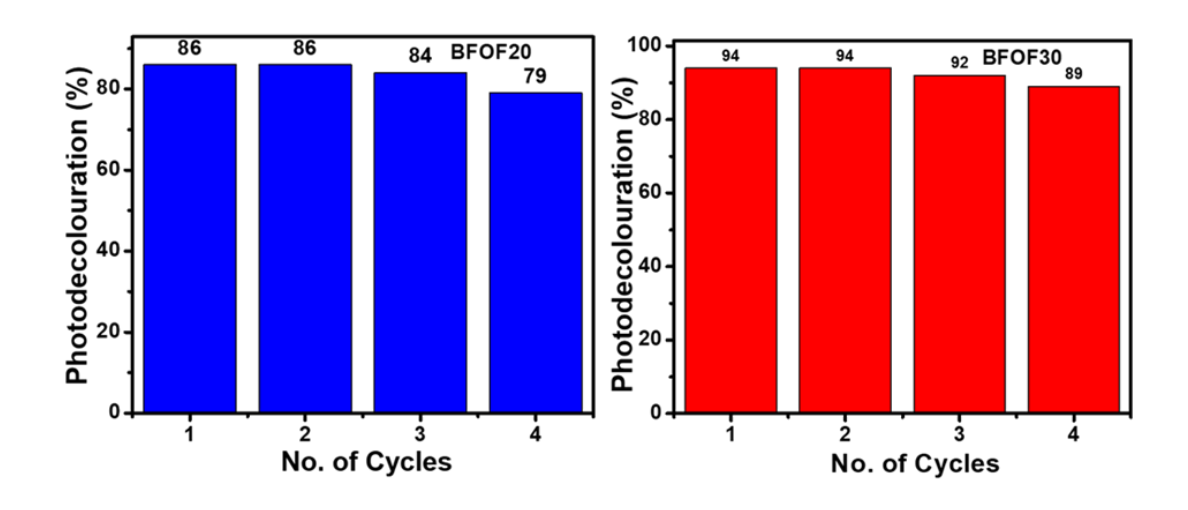


Figure 5.6. Photodegradation efficiency of heterostructures BFOF20 and BFOF30 after four cycles.

According to **figure 5.6**, there is no difference in the photodegradation efficiencies of the BFOF20 and BFOF30 catalysts for the first two cycles, and only a 6% and a 4% decline in the efficiency of BFOF20 and BFOF30, respectively, are visible after four cycles, demonstrating the stability of the suggested catalysts. It is essential to highlight that pure phase BFO magnetic responses are inadequate for recovering particles by applying magnetic fields, necessitating further filtering or centrifugation methods. We have tested the magnetic recovery property for BFOF30 since it is the most efficient catalyst among the three BFO+Fe₂O₃ heterostructures. As shown in **figure 5.7** (**b**), using a magnetic field enables us to recover the BFOF30 catalyst easily since it has an excellent magnetic response to the applied magnetic field.

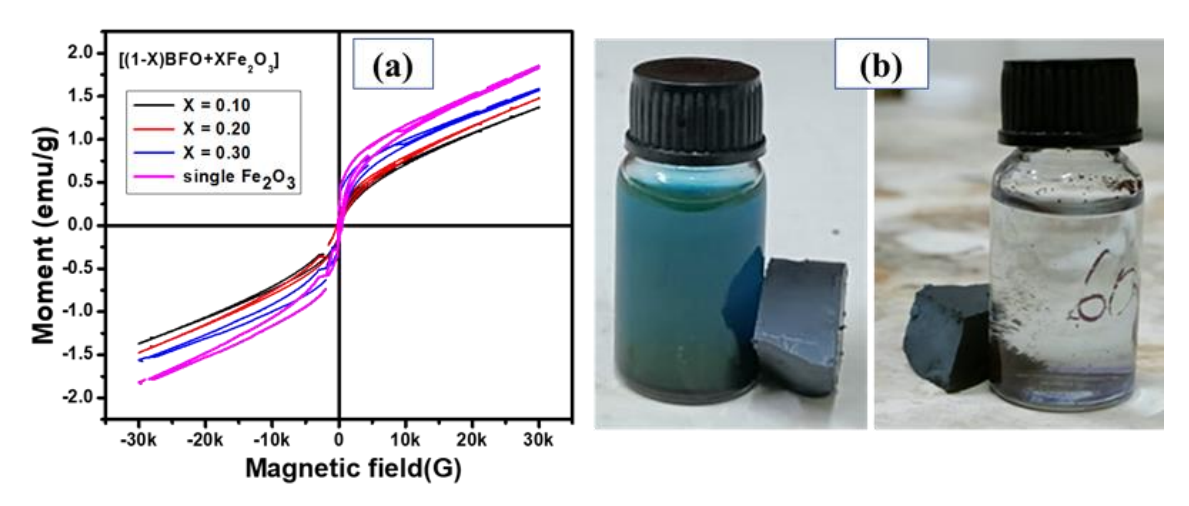


Figure 5.7. Magnetic properties of a) Fe_2O_3 and $BFO+Fe_2O_3$ heterostructure, b) Methylene Blue solution post-photocatalytic test for BFOF30 and its magnetic recovery

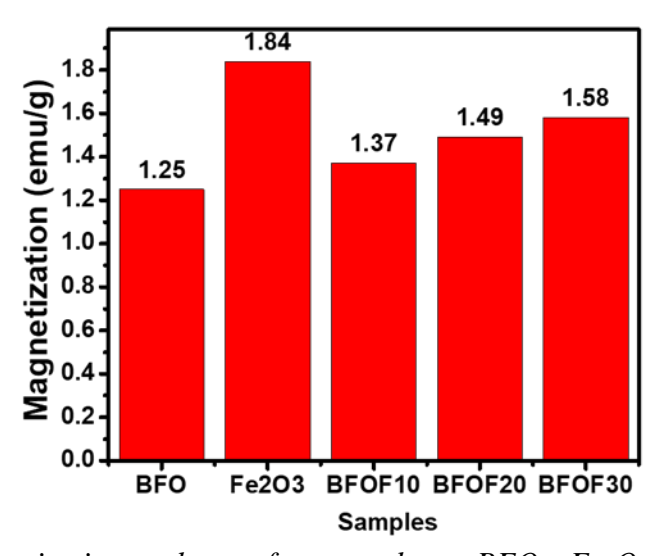


Figure 5.8. Magnetization values of pure phase BFO, Fe_2O_3 , and $BFO+Fe_2O_3$ heterostructure

The magnetization curves for the heterostructures and the pure phase Fe₂O₃ are shown in **figure 5.7(a)**. The magnetization increases with the increasing amount of Fe₂O₃ (1.84 emu/g) compared to BFO (1.25 emu/g, **figure 4.12**). The most efficient sample, BFOF30, had a maximum magnetism of 1.58 emu/g, which is adequate for magnetic recovery. The MB solution is shown in **figure 5.7(b)** before and after deterioration, and the catalyst BFOF30 is evenly distributed in the solution without using a magnetic field. A permanent magnet was used to show that the catalyst could restore itself from the MB solution by applying a 1.5 T magnetic field for 6 minutes. At the beginning and end of the Photocatalytic process, XRD was used on the BFOF30 powder to determine if it could be recovered. The XRD patterns for the BFOF30 pre- and post-degradation of MB patterns are shown in **figure 5.9**. For the BFOF30 catalyst used in the photocatalysis experiment, we found no variations in the XRD patterns or traces from MB. As a result, magnetically recovered BFOF30 catalyst maintains its original structural features, enhancing the likelihood that it will be reused.

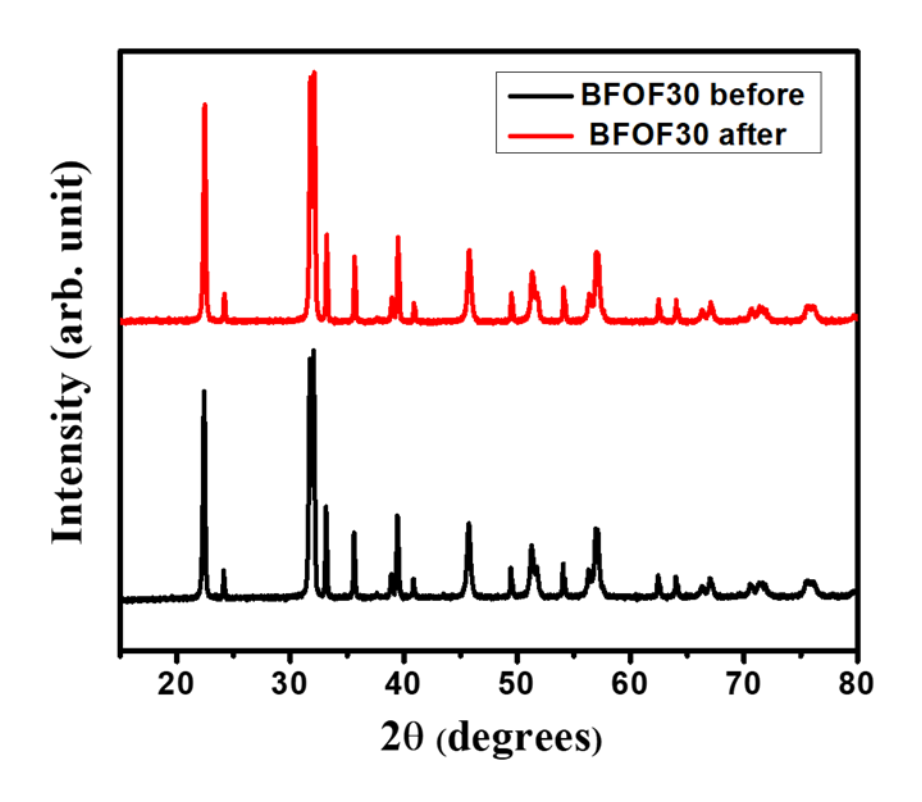


Figure 5.9. XRD patterns BFOF30 heterostructure pre and posts photocatalytic test for BFOF30.

5.6. Conclusion

In summary, the BFO+Fe₂O₃ heterostructure was successfully synthesized by coprecipitation with the microwave assistance method for MB degradation. Microstructure analysis and UV-Vis absorption spectroscopy show that the formation of micro interfaces between BFO and Fe₂O₃ microspheres can change the band gap and lead to changes in the work function at the surface of the heterostructures. Due to this, it is simpler to form electron-hole pairs and more difficult for them to recombine. The best results were obtained using BFOF30, which showed complete degradation (94%) in MB after 70 minutes of exposure to sunlight. According to the magnetic study, BFOF30 has the highest magnetization value compared to pure phase BFO, BFOF10, and BFO20. The recycling test shows that the photocatalyst BFOF30 can be recovered with a magnetic field and used at least four more times with a 4% reduction in efficiency. Finally, we proposed that the coexistence of a direct Fenton-like mechanism and a simultaneous electron drain process enhanced the photocatalytic efficiency of the BFO+Fe₂O₃ heterostructure.

REFERENCES

- 1. Minero, C. and Vione, D., 2006. A quantitative evalution of the photocatalytic performance of TiO₂ slurries. *Applied Catalysis B: Environmental*, 67(3-4), pp.257-269.
- 2. Liu, H., Ren, X. and Chen, L., 2016. Synthesis and characterization of magnetic metal—organic framework for the adsorptive removal of Rhodamine B from aqueous solution. *Journal of industrial and engineering chemistry*, 34, pp.278-285.
- 3. Fu, Y. and Wang, X., 2011. Magnetically separable ZnFe₂O₄–graphene catalyst and its high photocatalytic performance under visible light irradiation. *Industrial & Engineering Chemistry Research*, 50(12), pp.7210-7218.
- 4. Gad-Allah, T.A., Kato, S., Satokawa, S. and Kojima, T., 2009. Treatment of synthetic dyes wastewater utilizing a magnetically separable photocatalyst (TiO₂/SiO₂/Fe₃O₄): parametric and kinetic studies. *Desalination*, 244(1-3), pp.1-11.
- 5. Xuan, S., Jiang, W., Gong, X., Hu, Y. and Chen, Z., 2009. Magnetically separable Fe₃O₄/TiO₂ hollow spheres: fabrication and photocatalytic activity. *The Journal of Physical Chemistry C*, 113(2), pp.553-558.
- 6. Zheng, F., Shen, M., Guo, R., Fang, L. and Dong, W., 2011. Magnetically separable BiFeO₃ nanoparticles with a g-Fe₂O₃ parasitic phase: controlled fabrication and enhanced visible-light photocatalytic activity. *J Mater Chem*, 21, pp.18645-18652.
- 7. Liu, Y., Yu, L., Hu, Y., Guo, C., Zhang, F. and Lou, X.W.D., 2012. A magnetically separable photocatalyst based on nest-like γ-Fe₂O₃/ZnO double-shelled hollow structures with enhanced photocatalytic activity. *Nanoscale*, *4*(1), pp.183-187.
- 8. He, M., Li, D., Jiang, D. and Chen, M., 2012. Magnetically separable γ-Fe₂O₃@ SiO₂@ Ce-doped TiO₂ core–shell nanocomposites: Fabrication and visible-light-driven photocatalytic activity. *Journal of Solid-State Chemistry*, 192, pp.139-143.
- 9. Lou, Z., Li, F., Deng, J., Wang, L. and Zhang, T., 2013. Branch-like hierarchical heterostructure (α-Fe₂O₃/TiO₂): a novel sensing material for trimethylamine gas sensor. *ACS applied materials & interfaces*, 5(23), pp.12310-12316.
- 10. Chen, Q., Li, J., Li, X., Huang, K., Zhou, B., Cai, W. and Shangguan, W., 2012. Visible-light responsive photocatalytic fuel cell based on WO₃/W photoanode and Cu₂O/Cu photocathode for simultaneous wastewater treatment and electricity generation. *Environmental science & technology*, 46(20), pp.11451-11458.

- 11. Mishra, M. and Chun, D.M., 2015. α-Fe₂O₃ as a photocatalytic material: A review. *Applied Catalysis A: General*, 498, pp.126-141.
- 12. Suarez, C.M., Hernández, S. and Russo, N., 2015. BiVO4 as photocatalyst for solar fuels production through water splitting: a short review. *Applied Catalysis A: General*, 504, pp.158-170.
- 13. Tolod, K.R., Hernández, S. and Russo, N., 2017. Recent advances in the BiVO₄ photocatalyst for sun-driven water oxidation: top-performing photoanodes and scale-up challenges. *Catalysts*, 7(1), p.13.
- 14. Chen, L., Huang, R., Xiong, M., Yuan, Q., He, J., Jia, J., Yao, M.Y., Luo, S.L., Au, C.T. and Yin, S.F., 2013. Room-Temperature Synthesis of Flower-Like BiOX (X□ Cl, Br, I) Hierarchical Structures and Their Visible-Light Photocatalytic Activity. *Inorganic chemistry*, 52(19), pp.11118-11125.
- 15. Natarajan, K., Bajaj, H.C. and Tayade, R.J., 2016. Photocatalytic efficiency of bismuth oxyhalide (Br, Cl and I) nanoplates for RhB dye degradation under LED irradiation. *Journal of industrial and engineering chemistry*, *34*, pp.146-156.
- 16. Lee, S., Park, Y., Pradhan, D. and Sohn, Y., 2016. AgX (X= Cl, Br, I)/BiOX nanoplates and microspheres for pure and mixed (methyl orange, rhodamine B and methylene blue) dyes. *Journal of industrial and engineering chemistry*, *35*, pp.231-252.
- 17. Yan, Y., Zhou, Z., Cheng, Y., Qiu, L., Gao, C. and Zhou, J., 2014. Template-free fabrication of α-and β-Bi2O3 hollow spheres and their visible light photocatalytic activity for water purification. *Journal of alloys and compounds*, 605, pp.102-108.
- 18. Xiao, X., Hu, R., Liu, C., Xing, C., Qian, C., Zuo, X., Nan, J. and Wang, L., 2013. Facile large-scale synthesis of β-Bi₂O₃ nanospheres as a highly efficient photocatalyst for the degradation of acetaminophen under visible light irradiation. *Applied Catalysis B: Environmental*, 140, pp.433-443.
- 19. Mehring, M., Metastable b-Bi₂O₃ Nanoparticles with Potential for Photo-catalytic Water Purification Using Visible Light Irradiation.
- 20. Zheng, F., Shen, M., Guo, R., Fang, L. and Dong, W., 2011. Magnetically separable BiFeO₃ nanoparticles with a g-Fe₂O₃ parasitic phase: controlled fabrication and enhanced visible-light photocatalytic activity. *J Mater Chem*, 21, pp.18645-18652.
- 21. Selbach, S.M., Tybell, T., Einarsrud, M.A. and Grande, T., 2007. Size-dependent properties of multiferroic BiFeO₃ nanoparticles. *Chemistry of materials*, 19(26), pp.6478-6484.

- 22. Chen, D., Wang, Z., Ren, T., Ding, H., Yao, W., Zong, R. and Zhu, Y., 2014. Influence of defects on the photocatalytic activity of ZnO. *The Journal of Physical Chemistry C*, 118(28), pp.15300-15307.
- 23. Mishra, M. and Chun, D.M., 2015. α-Fe₂O₃ as a photocatalytic material: A review. *Applied Catalysis A: General*, 498, pp.126-141.
- 24. Wang, H., Zhang, L., Chen, Z., Hu, J., Li, S., Wang, Z., Liu, J. and Wang, X., 2014. Semiconductor heterojunction photocatalysts: design, construction, and photocatalytic performances. *Chemical Society Reviews*, 43(15), pp.5234-5244.
- 25. Li, S., Lin, Y.H., Zhang, B.P., Li, J.F. and Nan, C.W., 2009. BiFeO₃/TiO₂ coreshell structured nanocomposites as visible-active photocatalysts and their optical response mechanism. *Journal of Applied Physics*, 105(5), p.054310.
- 26. Niu, F., Chen, D., Qin, L., Zhang, N., Wang, J., Chen, Z. and Huang, Y., 2015. Facile synthesis of highly efficient p—n heterojunction CuO/BiFeO₃ composite photocatalysts with enhanced visible-light photocatalytic activity. *ChemCatChem*, 7(20), pp.3279-3289.
- 27. Fan, T., Chen, C., Tang, Z., Ni, Y. and Lu, C., 2015. Synthesis and characterization of g-C₃N₄/BiFeO₃ composites with an enhanced visible light photocatalytic activity. *Materials Science in Semiconductor Processing*, 40, pp.439-445.
- 28. Cui, Y., Briscoe, J., Wang, Y., Tarakina, N.V. and Dunn, S., 2017. Enhanced photocatalytic activity of heterostructured ferroelectric BaTiO₃/α-Fe₂O₃ and the significance of interface morphology control. *ACS applied materials & interfaces*, 9(29), pp.24518-24526.
- 29. Zheng, X., Huang, M., You, Y., Peng, H. and Wen, J., 2018. Core-shell structured α-Fe₂O₃@CeO₂ heterojunction for the enhanced visible-light photocatalytic activity. *Materials Research Bulletin*, 101, pp.20-28.
- 30. Can, M.M., Fırat, T. and Özcan, Ş., 2011. Interparticle interaction effects on magnetic behaviors of hematite (α-Fe₂O₃) nanoparticles. *Physica B: Condensed Matter*, 406(13), pp.2483-2487.
- 31. Yang, C.H., Kan, D., Takeuchi, I., Nagarajan, V. and Seidel, J., 2012. Doping BiFeO₃: approaches and enhanced functionality. *Physical Chemistry Chemical Physics*, *14*(46), pp.15953-15962.
- 32. Yang, S.Y., Martin, L.W., Byrnes, S.J., Conry, T.E., Basu, S.R., Paran, D., Reichertz, L., Ihlefeld, J., Adamo, C., Melville, A. and Chu, Y.H., 2009. Photovoltaic effects in BiFeO₃. *Applied Physics Letters*, *95*(6), p.062909.

- 33. Mishra, D.K. and Qi, X., 2010. Energy levels and photoluminescence properties of nickel-doped bismuth ferrite. *Journal of Alloys and Compounds*, 504(1), pp.27-31.
- 34. Zhu, A., Zhao, Q., Li, X. and Shi, Y., 2014. BiFeO₃/TiO₂ nanotube arrays composite electrode: construction, characterization, and enhanced photoelectrochemical properties. *ACS applied materials & interfaces*, 6(1), pp.671-679.
- 35. Wu, J., Fan, Z., Xiao, D., Zhu, J. and Wang, J., 2016. Multiferroic bismuth ferrite-based materials for multifunctional applications: ceramic bulks, thin films and nanostructures. *Progress in Materials Science*, 84, pp.335-402.
- 36. Lim, S.H., Murakami, M., Yang, J.H., Young, S.Y., Hattrick-Simpers, J., Wuttig, M., Salamanca-Riba, L.G. and Takeuchi, I., 2008. Enhanced dielectric properties in single crystal-like BiFeO₃ thin films grown by flux-mediated epitaxy. *Applied Physics Letters*, 92(1), p.012918.
- 37. Lim, S.H., Murakami, M., Yang, J.H., Young, S.Y., Hattrick-Simpers, J., Wuttig, M., Salamanca-Riba, L.G. and Takeuchi, I., 2008. Enhanced dielectric properties in single crystal-like BiFeO₃ thin films grown by flux-mediated epitaxy. *Applied Physics Letters*, 92(1), p.012918.
- 38. Gadhi, T.A., Hernández, S., Castellino, M., Chiodoni, A., Husak, T., Barrera, G., Allia, P., Russo, N. and Tagliaferro, A., 2018. Single BiFeO₃ and mixed BiFeO₃/Fe₂O₃/Bi₂Fe₄O₉ ferromagnetic photocatalysts for solar light driven water oxidation and dye pollutants degradation. *Journal of industrial and engineering chemistry*, 63, pp.437-448.
- 39. Zheng, F., Shen, M., Guo, R., Fang, L. and Dong, W., 2011. Magnetically separable BiFeO₃ nanoparticles with a g-Fe₂O₃ parasitic phase: controlled fabrication and enhanced visible-light photocatalytic activity. *J Mater Chem*, 21, pp.18645-18652.
- 40. Gadhi, T.A., Hernández, S., Castellino, M., Chiodoni, A., Husak, T., Barrera, G., Allia, P., Russo, N. and Tagliaferro, A., 2018. Single BiFeO₃ and mixed BiFeO₃/Fe₂O₃/Bi₂Fe₄O₉ ferromagnetic photocatalysts for solar light driven water oxidation and dye pollutants degradation. *Journal of industrial and engineering chemistry*, 63, pp.437-448.
- 41. Zhang, R., Liu, S., Kong, F., Tong, J., Ruan, L., Duan, Q., Zhou, J. and Zhang, X., 2020. α-Fe₂O₃/BiFeO₃ composites as visible-active photocatalysts and their optical response mechanism. *Journal of Physics and Chemistry of Solids*, *141*, p.109329.
- 42. Banoth, P., Sohan, A., Kandula, C., Kanaka, R.K. and Kollu, P., 2022. Microwave-Assisted Solvothermal Route for One-Step Synthesis of Pure Phase Bismuth Ferrite

- Microflowers with Improved Magnetic and Dielectric Properties. ACS omega, 7(15), pp.12910-12921.
- 43. De Los Santos Valladares, L., Félix, L.L., Suarez, S.E., Dominguez, A.B., Mitrelias, T., Holmes, S., Moreno, N.O., Aguiar, J.A. and Barnes, C.H.W., 2016. Preparation and crystallization of hollow α-Fe₂O₃ microspheres following the gasbubble template method. *Materials Chemistry and Physics*, *169*, pp.21-27.
- 44. Banoth, P., Sohan, A., Kandula, C., Kanaka, R.K. and Kollu, P., 2022. Microwave-Assisted Solvothermal Route for One-Step Synthesis of Pure Phase Bismuth Ferrite Microflowers with Improved Magnetic and Dielectric Properties. ACS omega, 7(15), pp.12910-12921
- 45. Sun, B., Han, P., Zhao, W., Liu, Y. and Chen, P., 2014. White-light-controlled magnetic and ferroelectric properties in multiferroic BiFeO₃ square nanosheets. *The Journal of Physical Chemistry C*, 118(32), pp.18814-18819.
- 46. Haislmaier, R.C., Podraza, N.J., Denev, S., Melville, A., Schlom, D.G. and Gopalan, V., 2013. Large nonlinear optical coefficients in pseudo-tetragonal BiFeO₃ thin films. *Applied Physics Letters*, 103(3), p.031906.

Chapter-6

A visible light active (1-x) BiFeO₃+xBTO (black TiO₂) photocatalyst for photocatalytic degradation of Methylene Blue

Objective

- ♦ The first and foremost aim is to fabricate BFO + BTO (black TiO₂) heterostructure by loading 10, 20, and 30% black TiO₂ (BTO) onto the BFO.
- So, for the first time, we aimed to load different ratios (x = 0.10, 0.20, 0.30) of black TiO_2 (bandgap of 1.68 eV) onto the BFO.
- ❖ Making a BFO+BTO heterostructure is expected to decrease the charge carrier recombination rate in pristine BFO because there will be overlapping of the bandgaps of these two semiconducting materials. As a result, electron-hole pairs will move from BFO semiconductor to BTO semiconductor, reducing the charge carrier recombination rate and thus increasing the lifetime of pairs.
- ❖ The current work's novelty is the study of photodegradation of MB dye in the presence of BFO+ BTO catalysts under sunlight.

6.1. Introduction

A promising strategy to address environmental problems and the energy shortage is the use of catalysts for the remediation of organic pollutants [1-6]. Photocatalysts are widely employed to break down contaminants in the ultraviolet or visible light spectrum. Perovskite-based photocatalysts are a significant class of semiconductors that both UV and visible light can activate. Combining the photocatalysts is one way to improve their photoactivity since pure photocatalysts are often not very effective when used by themselves.

A stable, non-toxic, and multiferroic visible light active photocatalyst has recently been explored to exist in the form of BFO. BFO has a band-gap from 2.2- 2.7 eV, which indicates

that it strongly absorbs light in the visible range from 200-800 nm [7-8]. Excellent characteristics of BFO have been seen in the degradation of pollutants. However, the main issue is that using BFO for photocatalysis is still challenging due to the high recombination rate of photogenerated electron-hole pairs. To address this problem, doping the BFO has attracted a lot of attention because, combined with other visible active semiconductors, which reduces the high recombination of photogenerated electron-hole pairs and increases photocatalytic activity [9–13].

The black TiO₂ functioned better as a photocatalyst than pure white TiO₂ because it could better separate photogenerated electron-hole pairs. The increased solar light absorption of black TiO₂ was brought on by the presence of Ti³⁺ and the oxygen vacancies [14-16]. Black TiO₂ (BTO) photocatalysts have recently received a lot of interest due to their exceptional light-absorbing properties, which even make the NIR region of the solar spectrum practical. The low band gap (1.54eV) value of BTO showed light absorption even in the near-infrared range [17]. Since then, BTO has received much research attention due to its numerous successful photocatalysis applications and other photoelectrochemical applications [6]. These enhanced light absorption properties of BTO contribute to the increased photocatalytic efficiency and reduced recombination of photogenerated charge carriers. As a result, synthesizing BFO-based heterostructures with BTO nanoparticles is expected to be a better photocatalyst than pure phase BFO [18-21]. In addition, the heterostructure's lower bandgap may result in more electrons and holes and higher photocatalytic efficiency. BFO heterostructures have shown improved photocatalytic activity in the degradation of organic dyes when exposed to visible light in recent studies [22–23]. Therefore, it seems possible to develop a strong heterostructure photocatalyst based on black TiO₂. The literature shows that no work reported black TiO₂ combining with BFO for organic dye degradation under visible-light exposure.

So far as we know, this is the first time that BFO+BTO (Black TiO_2) heterostructures have been made by the co-precipitation method. BFO and black TiO_2 powders were mixed in different molar ratios to prepare this heterostructure and heated in a microwave oven. In the present work, we have synthesized (1-x) BiFeO₃+xBTO (x=0.10, 0.20, 0.30)] by loading different ratios of BTO onto the BFO micro flowers. We have investigated how well these heterostructures degrade MB through photocatalysis when exposed to sunlight.

6.2. Experimental Section

6.2.1. Materials used for BFO+BTO heterostructures

For this procedure, ethanol, double-distilled water (DDW), pure potassium hydroxide (KOH, 98%), pure ferric chloride (FeCl₃.6H₂O, 98%), pure bismuth chloride (BiCl₃, 98%), and commercial white TiO₂ are all used.

6.2.2. Preparation of BiFeO₃ micro flowers

The pure phase BFO microwave flowers are synthesized in 3min at 800 W by microwave-assisted-solvothermal (MWAST) method in a domestic solo-microwave oven. The complete experimental procedure can be found in our previous work [7] [figure 4.12].

6.2.3. Preparation of black TiO₂ (BTO)

Making white TiO₂ pellets required only a few easy steps and careful focus on each step. The white TiO₂ powder was mixed with Ethylene Glycol (EG) and crushed in a mortar and pestle for 60 minutes. Using EG as a binder, a powder mixture was pressed in a hydraulic press at a pressure of 15 tonnes for 2 minutes, yielding a pellet in the shape of a circular disc. The pellet is sintered for two to six hours at temperatures between 800 and 1000° C. As a result of being exposed to an electron beam for 40-60 minutes, the white TiO₂ pellets turned into a black powder known as black TiO₂ (BTO).

6.2.4. Synthesis of (1-x) BFO+xBTO (x = 0.10, 0.20, 0.30)

BFO+BTO heterostructures are prepared by a simple coprecipitation method following the microwave heating at 360 W for 3 min. We dissolved a stoichiometric ratio of BFO and BTO powders in 100 ml of ethanol and sonicated it for 2 hours at 80° C to evaporate the solvent and obtain the gel. Finally, the obtained gel was washed with water and dried at 360 W for 5 min in a domestic microwave oven. Following the above procedure, we have synthesized three different heterostructures by loading different ratios of BTO onto the BFO. The prepared heterostructures (1-x) BFO+xBTO, where x = 0.10, 0.20, 0.30 are named as BFOT10, BFOT20 and BFOT30, respectively.

6.3. Characterizations

Analyzing the XRD data (PANalytical X'Pert Powder Diffractometer) at a scan rate of 4° /min and a step size of 0.02° , the scanning range in this diffractogram was 20^{θ} - 80^{θ} [20 value]. This analysis showed that pure phases of BFO, BTO, and BFO+BTO

heterostructures were formed. The optical characteristics of BFO, BTO, and BFO+BTO are investigated using UV-Visible spectroscopy (Jasco V-670 UV-Visible double beam spectrophotometer). The absorption spectra were recorded at wavelengths between 200nm and 800nm. Field emission scanning electron microscopy (FESEM: Carl Zeiss Smart Sem) and transmission electron microscopy were used to study the morphology of synthesized samples. A vibrating sample magnetometer measured the magnetic properties of synthesized heterostructures samples at room temperature (VSM, Model: LakeShore).

6.4. Photocatalysis

Using a model pollutant dye Methylene Blue, each prepared sample was assessed for its photocatalytic activity for degrading dye pollutant. Photodegradation was conducted in heavy sunlight. 40mg of each photocatalyst powder was initially added to 100ml of MB solution at a concentration of 0.9g/L and neutral pH. Following the continuous magnetic stirring, the slurry was irradiated with heavy sunlight. We monitored the decolourization of the dye solution using UV-Visible spectroscopy.

6.5. Result and Discussions

6.5.1. X-ray diffraction (XRD) analysis of BFO+BTO heterostructures

We synthesized BFO+BTO heterostructure powders using microwave-assisted chemical coprecipitation method at 10% (BFOT10), 20% (BFOT20), and 30% (BFOT30) BTO contents. **Figure 6.1** displays the XRD patterns of BFO, BTO, and BFO+BTO heterostructures. XRD analysis of the BFO revealed a Rhombohedral perovskite phase with an R_{3c} space group, consistent with crystallographic data (ICSD 98-019-1940), there was no evidence of impurity phases in the BFO structure. The XRD patterns of BTO displayed tetragonal symmetry, showing anatase and rutile phases. The XRD patterns revealed all peaks belonging to pure phase BFO with a low intense trace of the significant BTO peaks after adding 10% BTO (BFOT10). More intense BTO peaks began to form as the loading ratio of BTO reached 20% (BFOT20). After loading 30% BTO, the heterostructure sample BFOT30 finally displays all the high-intensity peaks from BTO besides the diffraction pattern of BFO. This higher BTO concentration is supported by the enhanced intensity of all the most significant BTO peaks besides the BFO peaks in the BFOT30.

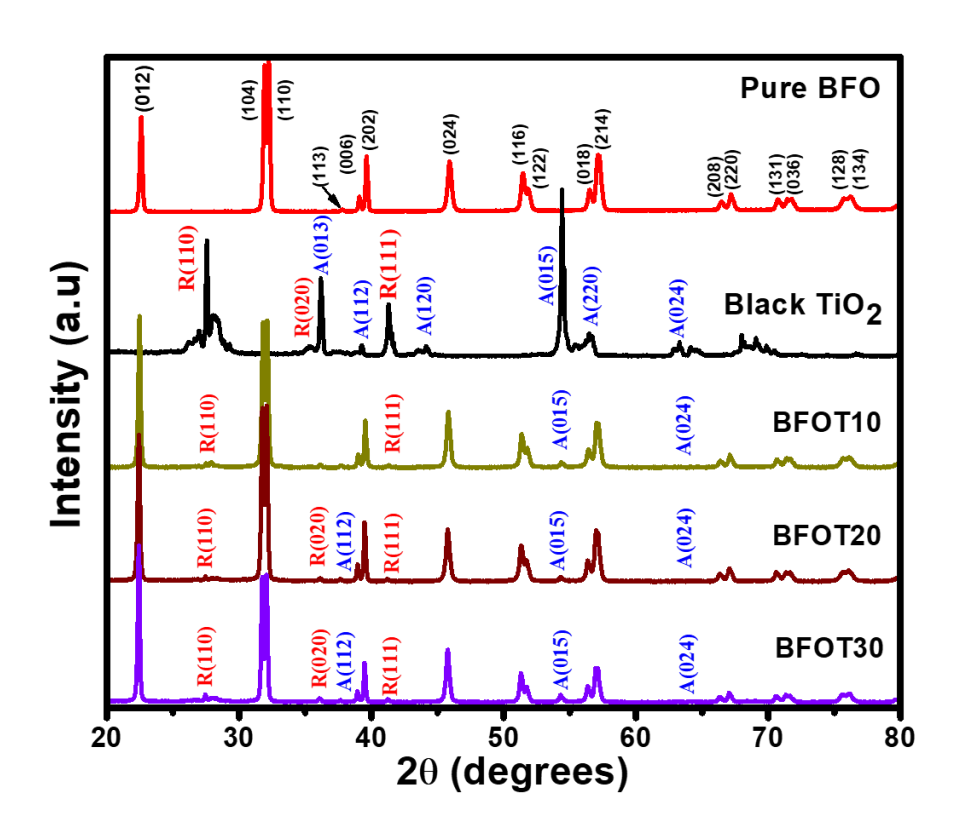


Figure 6.1. XRD patterns of pure phase BFO, BTO, BFOT10, BFOT20, and BFOT30.

6.5.2. FE-SEM analysis of BFO+BTO heterostructures

As shown in **figure 6.2**, FE-SEM was used to examine the microstructures of the various BFO+BTO samples. Figure 6.2(a) shows that pure phase BFO powder comprised many BFO micro flowers with hundreds of BFO nano petals packed tightly onto them [44]. A considerable number of BTO nanoparticles with different sizes and shapes were formed, as demonstrated by the microstructures of pure phase BTO in figure 6.2(b). Different molar ratios of BTO particles in BFO result in significant alteration of the microstructure of the BFO+BTO heterostructure [figure 6.2(c), (d), and (e)]. As shown in figure 6.2(c), the BFOT10 heterostructure is composed of several grains of different sizes with fewer grain boundaries, supporting the hypothesis that the BFO and BTO phases are not tightly coupled. According to figure 6.2 (d), the size of the grains is uniform, and the contact between the two phases increases with increasing BTO amounts. According to figure 6.2 (e), the microstructure of BFOT30 consists of a large number of grains distributed uniformly with many grain boundaries, and we can see excellent contact between the two phases. A stronger and more consistent coupling is observed in BFOT30 heterostructures compared to BFOT10 and BFOT30. According to figure 6.2(f, g, and h), the EDAX spectrum of BFOT10, BFOT20, and BFOT30 indicates that the signal peaks are attributed to the Bi, Fe, O, and Ti components, demonstrating that BTO was properly loaded on the BFO.

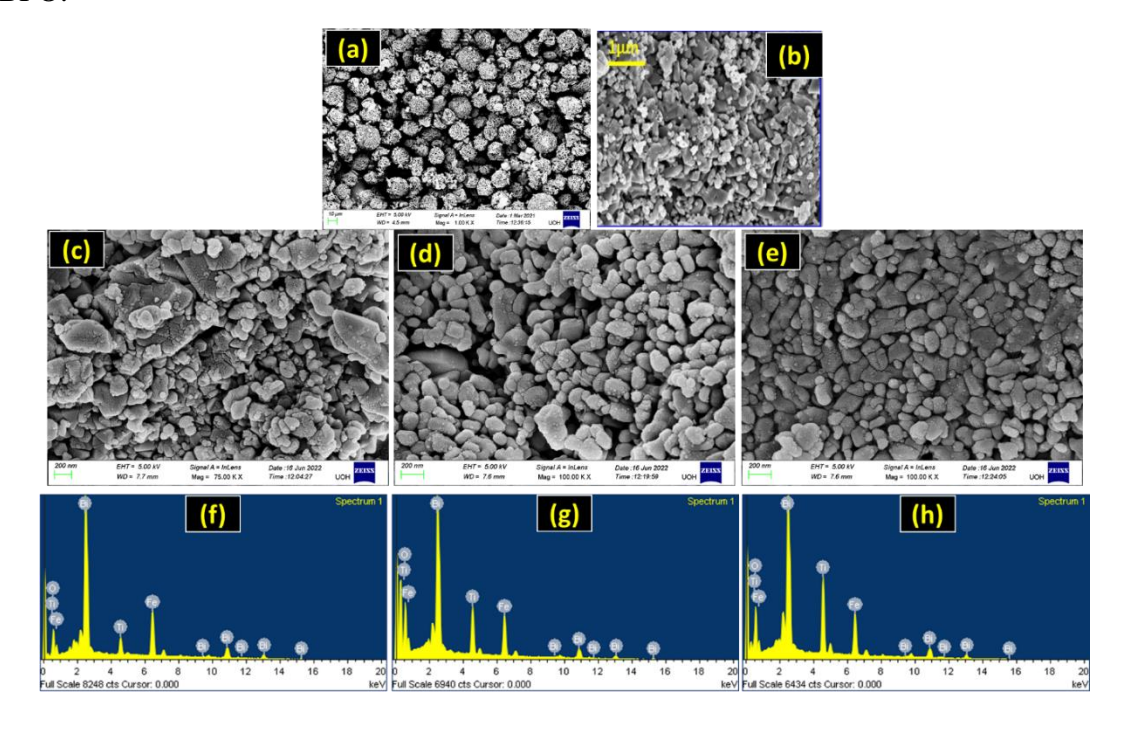


Figure 6.2. FE-SEM images of a) pure BFO, b) BTO, c) BFOT10, d) BFOT20, e) BFOT30 and EDAX spectra of f) BFOT10, g) BFOT20, h) BFOT30.

6.5.3. Optical properties of BFO+BTO heterostructures

The UV-Vis absorption spectrum of all the prepared samples is shown in **figure 6.3**. Each sample demonstrated excellent visible light absorption. All three heterostructures (BFOT10, BFOT20, and BFOT30) have displayed excellent optical absorption in the visible range, demonstrating their suitability for the visible photodegradation of organic dyes. The absorption of light at the visible spectral range from 500-800nm increased as the amount of BTO increased, revealing that the visible light absorbance of these heterostructures improved more than the pure phase BFO. The following formula determines the band gap of the heterostructures.

$$(\alpha h\vartheta) = A(h\vartheta - E_g)n$$

 α is the absorption coefficient, E_g represents the energy band gap, A is constant, and depending on transition, we have to consider n values

direct permitted transitions, n = 1/2

direct forbidden transitions, n = 3/2.

permitted indirect transitions, n = 2. indirect prohibited transitions, n = 3.

The obtained band energies of these heterostructures BFOT10 (552 nm), BFOT20 (560nm), and BFOT30 (650nm) were 2.24, 2.21, and 1.91 eV. According to the bandgap studies, these heterostructures have a lower energy band gap than the pure phase BFO (**figure 4.14**). The combination of two different energy band gaps at the semiconductor interface may lead to a reduced energy band gap. As a result, BFOT30 was the most efficient photocatalyst when absorbing visible-light photons among the coupled photocatalysts. From this study, it has been observed that BFOT30 has a higher absorption of light in the visible range with a lower bandgap compared to the other two (BFOT10 and BFOT20) and is expected to produce a higher number of photogenerated electron holes.

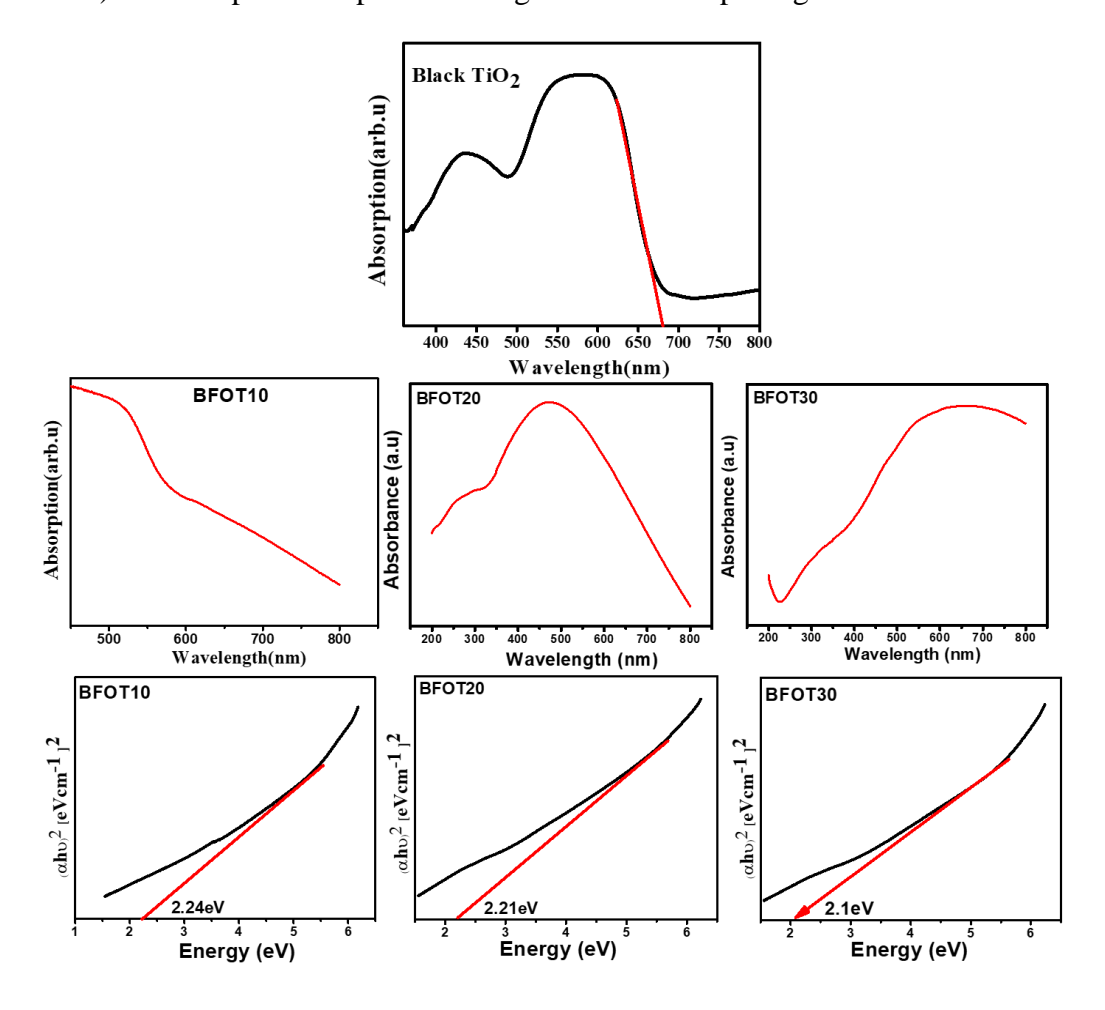


Figure 6.3. UV-Vis absorption spectroscopy and energy band gap of BTO, BFOT10, BFOT20, and BFOT30.

Table 6.1. Optical energy band gaps obtained from UV-Vis absorption studies

S. No	Sample	The band gap (eV)
1	BFO (figure 4. 15)	2.25
2	ВТО	1.68
3	BFOT10	2.24
4	BFOT20	2.21
5	BFOT30	2.1

6.5.4. Photocatalytic activity of BFO+BTO heterostructures

The full degradation of MB for the BFO (33%), BTO (78%) and BFO+BTO heterostructure took 70 minutes to complete (figure 6.4). After adding 10% BTO to the BFO [BFOT10], we observed less degradation (65%) in the MB solution when compared to the other two heterostructures [BFOT20, BFOT30]. The efficiency was increased for the BFOT20 and BFOT30 samples, and after only 70 minutes, 86 and 97% of the deterioration had occurred, respectively. The increased photocatalytic performance of the samples BFOT20 and BFOT30 demonstrate how efficiency increased for higher concentrations of BTO. Since the BFOT30 heterostructure is composed of large numbers of grains with uniform distribution and many grain boundaries, it has high degradation efficiency (97%) compared to the BFOT10 and BFOT20 heterostructures. Even though BFOT30 has a narrower band gap than the other two samples, it is easier for light to form electron-hole pairs at the surface of BFO+BTO. As a result, its efficiency is improved. This photodegradation test demonstrates excellent results for the rapid photodegradation efficiency of heterostructures compared to pure phase BFO, demonstrating these heterostructures' abilities to degrade MB in sunlight. Photocatalyst performance is determined by the equation below. Both Co and Ct represent MB's initial and timecorresponding concentrations, respectively.

$$Efficiency = \frac{C_0 - C_t}{C_0} x \ 100$$

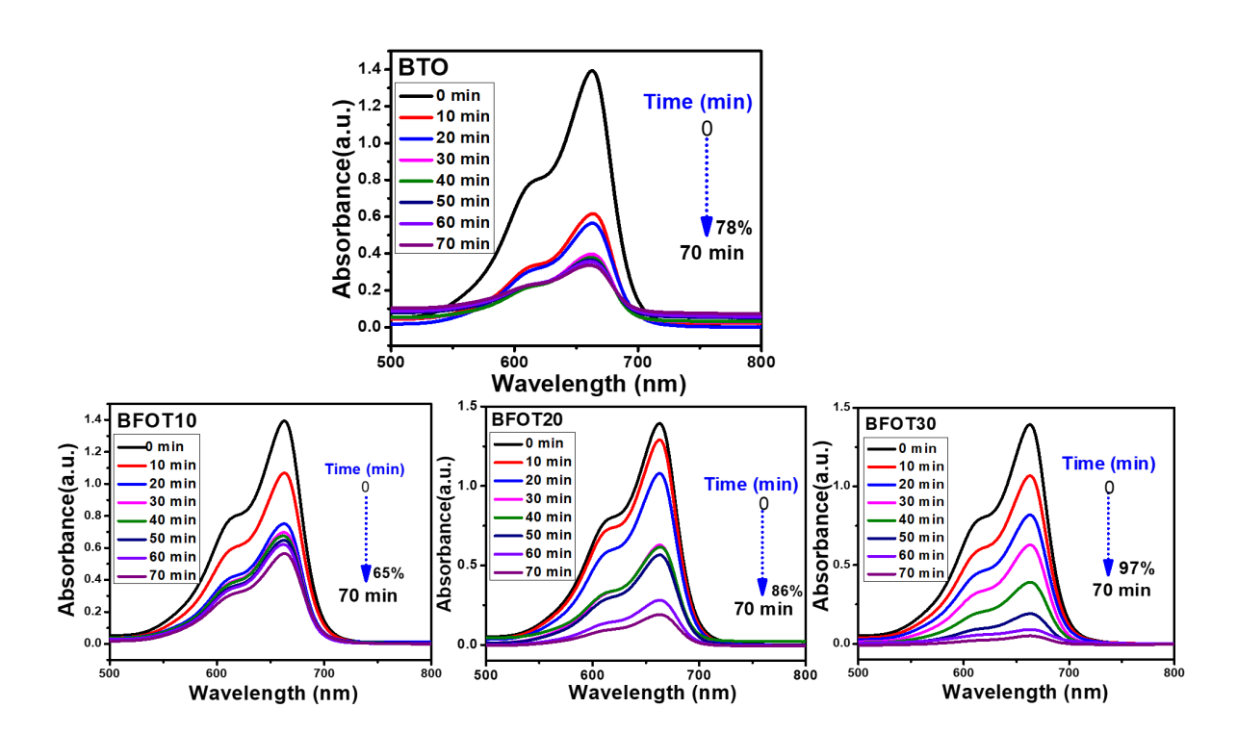


Figure 6.4. Time dependant UV-Vis spectral changes of Methylene Blue in the presence of BTO, BFOT10, BFOT20, and BFOT30.

6.5.5. Effect of Photocatalyst concentration on photocatalytic efficiency

The degradation of MB dye was carried out at a constant dosage of 10 mg/500 ml using different heterostructures BFOT10, BFOT20, and BFOT30 catalyst dosages (10, 20, 30 and 40 mg). The catalyst dosage, the initial dosage of dye, type of dye, pH value of dye, and most microstructures of the catalysts were all factors that affected the dye degradation. **Figure 6.5** shows that MB's photodegradation efficiency increases as the catalyst concentration increases [all the obtained values are depicted in **table 6.2**], indicating that the photodegradation efficiency strongly depends on the catalyst concentration. It is well known from the literature that photodegradation efficiency strongly depends on the microstructures, pH values, initial concentration of dye etc.

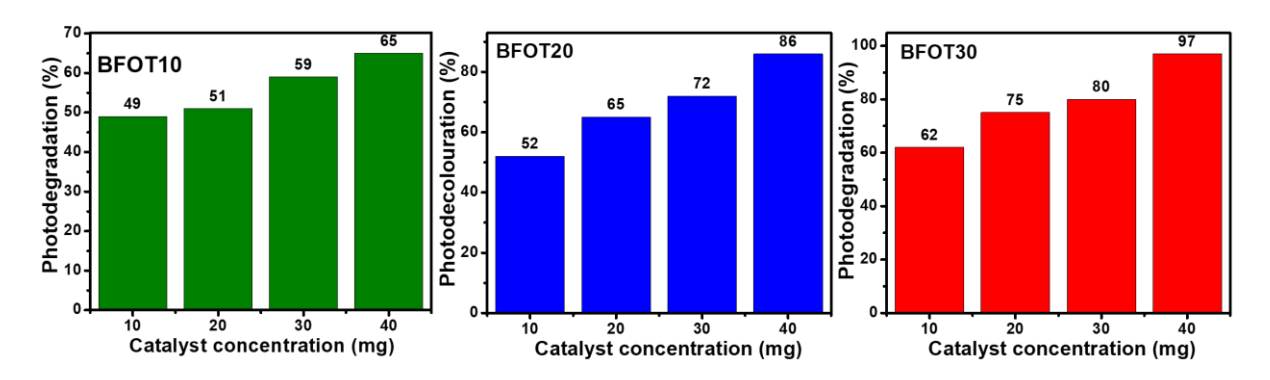


Figure 6.5. Effect of photocatalyst dosage on photodegradation efficiency of heterostructures BFOT10, BFOT20, and BFOT30.

Table 6.2 Influence of catalyst dosage (mg) on Photodegradation (%)

Dye Name	Catalyst name	Catalyst dosage (mg)	Time (min)	Degradation (%)
MB	BFOT10	10	70	49
		20	70	51
		30	70	59
		40	70	65
MB	BFOT20	10	70	52
		20	70	65
		30	70	72
		40	70	86

MB	BFOT30	10	70	62
		20	70	75
		30	70	80
		40	70	97

6.5.6. Reusability and magnetic recovery test for BFO+BTO Photocatalysts

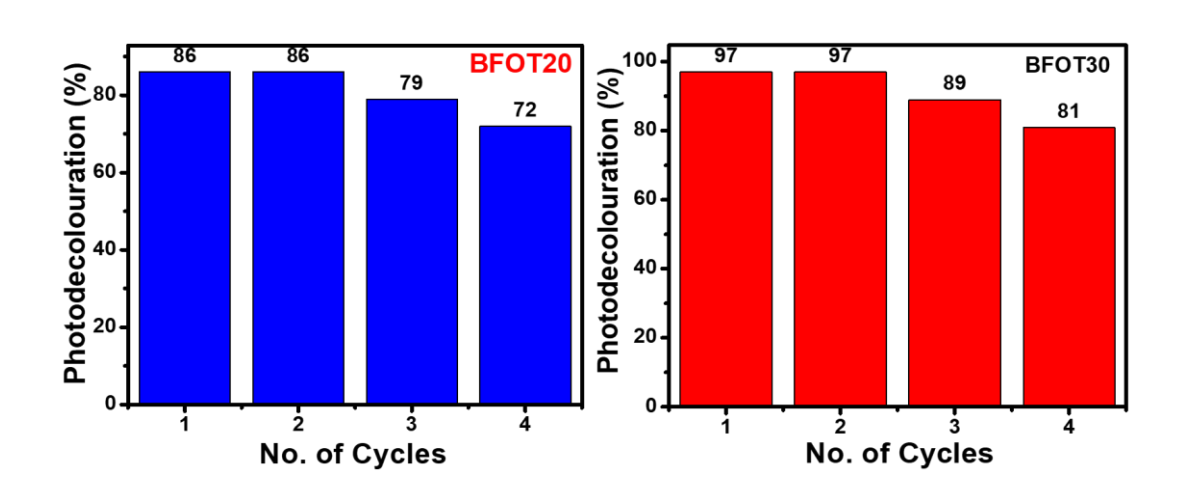


Figure 6.6. Photodegradation efficiency of heterostructures BFOT20 and BFOT30 after four cycles.

The stability was investigated by recycling the most productive powders BFOT20 and BFOT30 catalysts four times. According to **figure 6.6**, there is no difference in the photodegradation efficiencies of the BFOT20 and BFOT30 catalysts for the first two cycles, but the catalysts' poor stability is demonstrated by a 13% decline in BFOT20's photodegradation efficiency and a 16% decline in BFOT30's photodegradation efficiency after two cycles. The room temperature magnetic properties of BTO and BFO+BTO heterostructures are shown in **figure 6.7**. **Figure 6.7** (**a–b**) shows that single-phase BFO has a high magnetization value of 1.25 emu/g, while black TiO₂ is diamagnetic when a magnetic field is applied. The magnetic properties of BFO+BTO have decreased with an increase in diamagnetic phase BTO loaded on weak ferromagnetic phase BFO [**figure 6.7(b)**]. When 10% diamagnetic BTO is added to BFO, the magnetization value is reduced

to 0.32 emu/g (**BFOT10**). After increasing the BTO molar ratio to 20% and 30%, the heterostructures BFOT20 and BFOT30 show linear M-H curves, indicating they are diamagnetic [**figure. 6.7** (**c**)] shows the close-ups of the M-H loops for BTO, BFOT20, and BFOT30).

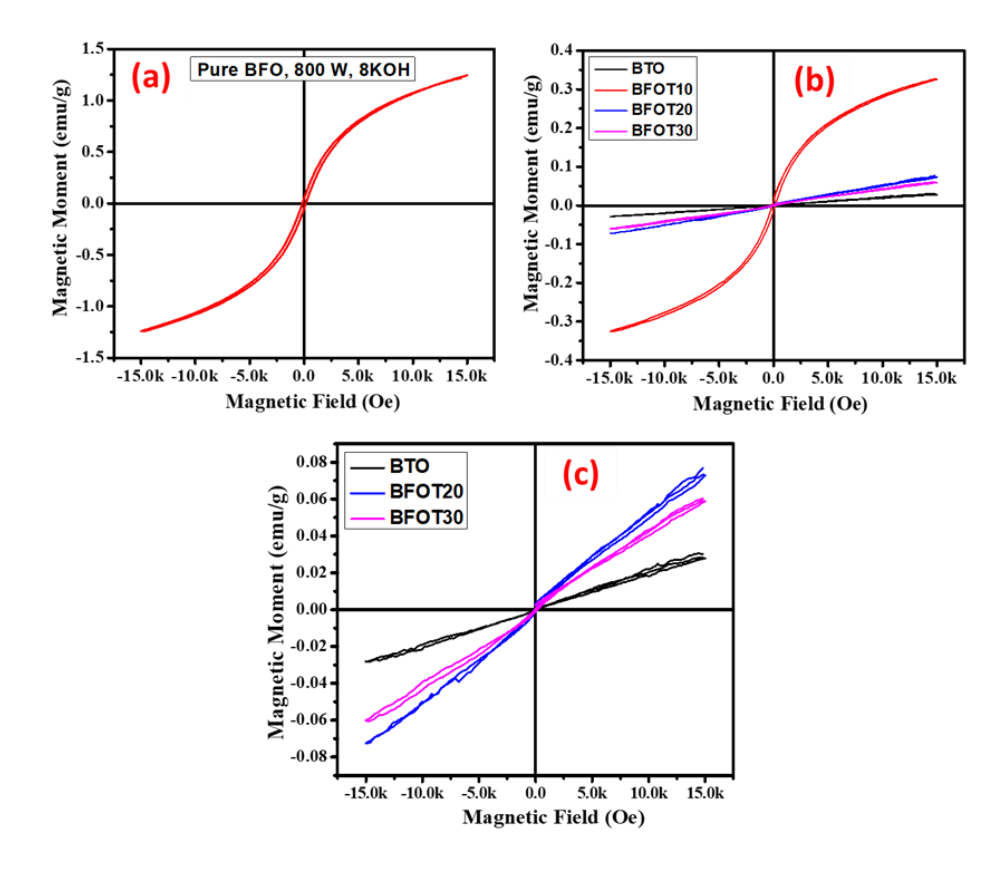


Figure 6.7. *Magnetic properties of a) BFO, b) BFO+BTO heterostructure, c) Zoomed M-H loops for BTO, BFOT20 and BFOF30.*

Figure 6.8 (a) highlights how pure phase BFO magnetic responses fail to recover particles when applied to magnetic fields after the photodegradation experiment. Therefore, additional filtering or centrifugation is required to separate the catalyst from the MB solution. To study the magnetic recovery of the most effective photocatalyst, BFOT30, we applied the magnetic field shown in **figure 6.8** (b). As shown in **figure 6.8** (b), BFOT30 cannot be recovered when a magnetic field is applied due to its diamagnetic, confirming its weak magnetic recovery. The results of these stability and recovery studies indicate that the stability and magnetic recovery properties of BFO did not improve, even when black TiO₂ was added. When a magnetic field was applied to BFO+BTO, the magnetic response may have been reduced and exhibited diamagnetic properties due to the non-magnetic TiO₂ loaded on weak magnetic phase BFO.



Figure 6.8. Magnetic recovery test for a) BFO and b) BFOT30.

6.6. Conclusion

The BFO+BTO heterostructure was successfully processed by co-precipitation with microwave help for MB degradation. Microstructure analysis and UV-Vis absorption spectroscopy in visible light have shown that the formation of nano-interfaces between the BFO and Black TiO₂ phases can change the band gap and encourage changes in the work function at the surface of the heterostructures, improving the creation of electron-hole pairs and impeding its recombination. After 70 minutes in the sun, BFO+BTO produces the best (97%) results with the highest deterioration in MB. The photocatalyst can only be utilized for two cycles with a 16% reduction in efficiency, according to the recycling test for the most effective BFOT30. It also cannot be retrieved using a magnetic field. A photocatalytic test showed that black TiO₂ increased the activity of pure phase BFO when added to it. According to our findings, a simultaneous electron drain process between BFO and BTO, as well as a direct Fenton-like mechanism, contributed to the BFO+BTO heterostructure's enhanced photocatalytic efficiency.

REFERENCES

- 1. Xing, Z., Zhou, W., Du, F., Qu, Y., Tian, G., Pan, K., Tian, C. and Fu, H., 2014. A floating macro/mesoporous crystalline anatase TiO₂ ceramic with enhanced photocatalytic performance for recalcitrant wastewater degradation. *Dalton Transactions*, 43(2), pp.790-798.
- 2. Jiang, Z., Zhu, C., Wan, W., Qian, K. and Xie, J., 2016. Constructing graphite-like carbon nitride modified hierarchical yolk–shell TiO₂ spheres for water pollution treatment and hydrogen production. *Journal of Materials Chemistry A*, 4(5), pp.1806-1818.
- 3. Xing, Z., Zhou, W., Du, F., Zhang, L., Li, Z., Zhang, H. and Li, W., 2014. Facile synthesis of hierarchical porous TiO₂ ceramics with enhanced photocatalytic performance for micro polluted pesticide degradation. *ACS applied materials & interfaces*, 6(19), pp.16653-16660.
- 4. Liu, X., Xing, Z., Zhang, H., Wang, W., Zhang, Y., Li, Z., Wu, X., Yu, X. and Zhou, W., 2016. Fabrication of 3 D Mesoporous Black TiO₂/MoS₂/TiO₂ Nanosheets for Visible-Light-Driven Photocatalysis. *ChemSusChem*, 9(10), pp.1118-1124.
- 5. Chen, X., Liu, L., Yu, P.Y. and Mao, S.S., 2011. Increasing solar absorption for photocatalysis with black hydrogenated titanium dioxide nanocrystals. *Science*, *331*(6018), pp.746-750.
- 6. Ullattil, S.G., Narendranath, S.B., Pillai, S.C. and Periyat, P., 2018. Black TiO₂ nanomaterials: a review of recent advances. *Chemical Engineering Journal*, *343*, pp.708-736.
- 7. Sando, D., Yang, Y., Bousquet, E., Carrétéro, C., Garcia, V., Fusil, S., Dolfi, D., Barthélémy, A., Ghosez, P., Bellaiche, L. and Bibes, M., 2016. Large elasto-optic effect and reversible electrochromism in multiferroic BiFeO₃. *Nature Communications*, 7(1), pp.1-7.
- 8. Prado-Gonjal, J., Villafuerte-Castrejón, M.E., Fuentes, L. and Moran, E., 2009. Microwave–hydrothermal synthesis of the multiferroic BiFeO₃. *Materials Research Bulletin*, 44(8), pp.1734-1737.
- 9. Morozov, M.I., Lomanova, N.A. and Gusarov, V.V., 2003. Specific features of BiFeO₃ formation in a mixture of bismuth (III) and iron (III) oxides. *Russian journal of general chemistry*, 73(11), pp.1676-1680.

- 10. Valant, M., Axelsson, A.K. and Alford, N., 2007. Peculiarities of a solid-state synthesis of multiferroic polycrystalline BiFeO3. *Chemistry of Materials*, 19(22), pp.5431-5436.
- 11. Liu, G., Wang, T., Zhou, W., Meng, X., Zhang, H., Liu, H., Kako, T. and Ye, J., 2015. Crystal-facet-dependent hot-electron transfer in plasmonic-Au/semiconductor heterostructures for efficient solar photocatalysis. *Journal of materials chemistry C*, 3(29), pp.7538-7542.
- 12. Liu, G., Wang, T., Zhou, W., Meng, X., Zhang, H., Liu, H., Kako, T. and Ye, J., 2015. Crystal-facet-dependent hot-electron transfer in plasmonic-Au/semiconductor heterostructures for efficient solar photocatalysis. *Journal of materials chemistry C*, *3*(29), pp.7538-7542.
- 13. Wang, X., Mao, W., Zhang, J., Han, Y., Quan, C., Zhang, Q., Yang, T., Yang, J., Li, X.A. and Huang, W., 2015. Facile fabrication of highly efficient g-C₃N₄/BiFeO₃ nanocomposites with enhanced visible light photocatalytic activities. *Journal of colloid and interface science*, 448, pp.17-23.
- 14. Tian, L., Xu, J., Just, M., Green, M., Liu, L. and Chen, X., 2017. Broad range energy absorption enabled by hydrogenated TiO₂ nanosheets: from optical to infrared and microwave. *Journal of Materials Chemistry C*, *5*(19), pp.4645-4653.
- 15. Li, K., Xu, J., Yan, X., Liu, L., Chen, X., Luo, Y., He, J. and Shen, D.Z., 2016. The origin of the strong microwave absorption in black TiO2. *Applied Physics Letters*, 108(18), p.183102.
- 16. Xia, T., Zhang, C., Oyler, N.A. and Chen, X., 2013. Hydrogenated TiO₂ nanocrystals: a novel microwave absorbing material. *Advanced Materials*, 25(47), pp.6905-6910.
- 17. Jiang, X., Zhang, Y., Jiang, J., Rong, Y., Wang, Y., Wu, Y. and Pan, C., 2012. Characterization of oxygen vacancy associates within hydrogenated TiO₂: a positron annihilation study. *The Journal of Physical Chemistry C*, 116(42), pp.22619-22624.
- 18. Hu, Z., Li, Q., Li, M., Wang, Q., Zhu, Y., Liu, X., Zhao, X., Liu, Y. and Dong, S., 2013. Ferroelectric memristor based on Pt/BiFeO₃/Nb-doped SrTiO₃ heterostructure. *Applied Physics Letters*, 102(10), p.102901.
- 19. Qu, T.L., Zhao, Y.G., Yu, P., Zhao, H.C., Zhang, S. and Yang, L.F., 2012. Exchange bias effects in epitaxial Fe₃O₄/BiFeO₃ heterostructures. *Applied Physics Letters*, 100(24), p.242410.

- 20. Ren, Y., Nan, F., You, L., Zhou, Y., Wang, Y., Wang, J., Su, X., Shen, M. and Fang, L., 2017. Enhanced photoelectrochemical performance in reduced graphene oxide/BiFeO₃ heterostructures. *Small*, *13*(16), p.1603457.
- 21. Lee, H., Joo, H.Y., Yoon, C., Lee, J., Lee, H., Choi, J., Park, B. and Choi, T., 2017. Ferroelectric BiFeO₃/TiO₂ nanotube heterostructures for enhanced photoelectrochemical performance. *Current Applied Physics*, *17*(5), pp.679-683.
- 22. Alferov, Z.I., 1998. The history and future of semiconductor heterostructures. *Semiconductors*, 32(1), pp.1-14.
- 23. Bagvand, N., Sharifnia, S. and Karamian, E., 2018. A visible-light-active BiFeO₃/ZnS nanocomposite for photocatalytic conversion of greenhouse gases. *Korean Journal of Chemical Engineering*, *35*(8), pp.1735-1740.

Chapter-7

Overall Summary and Future Work

7.1. Overall Summary

Materials with multiple ferroic characteristics combine them in a way that influences one another. These materials are highly recommended for spintronic devices, sensors, and future computer memory concepts. BiFeO₃ has sparked many scientists' curiosity since its discovery in 1960. It has multiferroic properties at room temperature, which makes it one of the most promising lead-free piezoelectric materials. In recent years, BFO has been studied the most because of its high ferroelectric curie temperature (T_c) of 850°C and Neel temperature (T_N) of 370°C. The high chemical fluctuations of BFO are one of its disadvantages. Another is its strong coercive field and irregular magnetic spin structure. Leakage current happens due to the single-phase BFO candidate's lack of stoichiometry. The oxide impurities Bi₂₅FeO₃₉ and Bi₂Fe₄O₉, which have different bismuth-to-iron ratios, are routinely produced during the production of BFO. Due to the charge imbalance brought on by the impurity phases, which also results in substantial current leakage, it will be challenging to observe the electrical polarization. In the range of 2.2–2.8 eV, BFO possesses a small optical band gap at ambient temperature. This small band gap increases the absorbance to a maximum of 750 nm. Because the BFO is ferroelectric, the depolarization of the electric field produces the photocurrent. This photocurrent makes separating the photogenerated charged carriers easier and restrains the charge carrier recombination loss as in commonly recognised semiconductors. BFO is a better candidate for photocatalysis because of these distinctive qualities. BFO that has a narrow band gap and an appropriate band position satisfy the solar light-induced photocatalytic activity prerequisites.

Many research teams have investigated various synthesis methods, including physical and wet chemical ones, to create a pure phase BFO. At low temperatures, wet chemical techniques are more advantageous for obtaining a pure phase BFO. Microwave-assisted solvothermal technology provides the most benefits compared to other wet chemical procedures. While microwaves have been widely used in organic synthesis, they have not yet reached their full potential. Its advantages include quick heating rate, time savings of

several orders of magnitude, suppression of side reactions, and excellent repeatability of a given synthesis procedure. Additionally, it has been used to synthesize inorganic nanomaterials. BFO has limited applications in practical devices due to its limitations, such as low photocatalytic activity, low ferroelectricity, and weak magnetic properties.

Due to the BFO's poor photocatalytic efficacy compared to other commercially available materials, the technology has not yet been commercialized for photocatalysis. When the band gap is excited, electron-hole pairs become spatially relatively close. It is important to note that the distance between the e- and h+ pairs of a promising photocatalyst and its optical absorption characteristics such as electron band structure, morphology, particle size, porosity, and the surface area directly affect its efficiency and photocatalytic activity. According to literature reviews, the heterojunction-equipped photocatalyst has demonstrated increased photocatalytic activity. This results from the heterojunction's development of a Schottky barrier, which prevents electron-hole pairs from moving between semiconductors, lowers the rate of charge carrier recombination and prolongs electron-hole pairs' lifetime. So, heterojunction production can significantly enhance the photocatalytic activity of virgin BFO.

Our study focuses on the synthesis of BFOs without mineralizers, the synthesis of BFOs using solvothermal and microwave-assisted solvothermal methods, and the synthesis of BFO-based heterostructures because such materials could be used in a wide range of applications. Several optimisations were made to the ideal experimental setup for synthesizing highly crystalline BFO. BFO synthesized with both methods has been examined for its structural, magnetic, electrical, and optical properties, and the results have been compared. We attempted to enhance the photocatalytic activity of pure phase BFO by loading two different visible active semiconductors.

The multiferroic BFO and heterostructures based on BFO have been characterised using various analytical techniques. These include the powder XRD technique to examine phase formation and structural parameters, FE-SEM and TEM with electron dispersion spectroscopy to examine the morphology and texture of microstructures, elemental compositions, XPS to examine the oxidation states of constituent elements, FTIR and Raman to examine absorption spectra, followed by the stretching vibrations of the

materials, VSM to investigate magnetic properties, and a dielectric analyzer to test electrical properties.

To synthesise the desired components, high-purity metal chlorides, Hexamethylenetetramine, potassium hydroxide, commercial TiO₂, ethanol, and distilled water were employed. Simple solvothermal, microwave-assisted-solvothermal and coprecipitation techniques were used to synthesize BFO and BFO-based heterostructures. The materials were examined in powder form for their structural, morphological, and magnetic properties, while pelletized samples were used to determine their electrical properties, such as dielectric and ferroelectric properties.

Solvothermal was used to prepare a total of 4 BFO samples at various HMTA concentrations, while microwave-assisted solvothermal was used to prepare a total of 7 BFO samples at various microwave powers, microwave heating periods, and KOH concentrations. We have synthesized three series each of BFO+Fe₂O₃ and BFO+black TiO₂ heterostructures. Further, a literature review and key ideas about multiferroic materials are discussed in chapter one of this thesis. In the second chapter, we discuss the methods used in this thesis for synthesis and characterization. Chapters one through six have been summarized in the following sections.

7.1.1. Synthesis of BFO through the solvothermal method

This study synthesised BFO multiferroic material using HMTA as a precipitating agent and metal chloride precursors at 180°C for four hours. A powder XRD technique and Rietveld refinement were used to analyze structural formation and parameters. The outcomes so achieved are very similar to the works that have been previously published. The FE-SEM pictures revealed a uniform distribution of grains of various sizes and shapes. FT-IR and Raman spectroscopies were used to examine the vibrational stretching bonds between the constituent's metal-oxygen bonds. The highly crystallized BFO sample was found to have a rhombic perovskite structure, confirming its pure phase with 6M HMTA concentration. A pure phase BFO (6M, HMTA) demonstrates an excellent dielectric constant with negligible dielectric loss, according to research on dielectric spectroscopy at ambient temperature. At room temperature, the BFO samples produced with different concentrations of HMTA showed weak magnetic properties. Compared to BFO samples made with low molar HMTA concentrations (0.5, 2, and 4M HMTA), a pure phase BFO

(6M HMTA) exhibited the highest magnetization value. All of the BFO samples showed weak and lossy ferroelectric unsaturated P-E loops, according to the ferroelectric experiments conducted at room temperature. Pure phase BFO has been shown to exhibit outstanding visible light absorption with a band gap of 2.32 eV and photocatalytic activity of 10% when exposed to strong sunlight, according to UV-Vis absorption spectroscopy. Based on the results of the characterizations, it was found that a pure phase BFO could be synthesized by 6M HMTA at 180°C for 4 hours through the solvothermal method.

7.1.2. Synthesis of BFO through microwave solvothermal method

The multiferroic and optical properties of BFO, which were produced using a single-step microwave-assisted solvothermal process with a quick response time of just three minutes, were examined in this chapter. As part of the overall optimizations, different microwave powers (360W, 700W, 800W), KOH concentrations (6M, 8M, 10M, 12M) and microwave heating duration were investigated to determine the ideal favourable conditions for obtaining the required pure phase BFO. The XRD analysis showed that the pure phase BFO could be produced in 3 minutes of microwave heating at 800 W. The XRD analysis revealed that BFO synthesized at a high microwave power of 800W for 3 minutes with 8M KOH showed outstanding pure phase BFO micro flowers with closely packed petals on the surface and without aggregation. We conclude from our alkaline optimizations that KOH concentrations significantly influence the surface form of micro flowers. The dielectric properties were qualitatively investigated at room temperature using dielectric spectroscopy revealed that the pure phase BFO has shown an excellent dielectric constant frequency response with a minimal dielectric loss. The magnetic studies show that all the BFO samples exhibit weak ferromagnetic behaviour, which is different from the antiferromagnetic behaviour reported in the previous works. The development of oxygen vacancies and the presence of Fe²⁺ oxidation state, both identified by the XPS analysis of pure phase BFO, were the two factors that contributed to the significant leakage current in the pure phase BFO. Following that, we studied the ferroelectric properties of the pure phase BFO, and this study confirmed its poor ferroelectric behaviour at room temperature. Based on the UV-Vis spectra of pure phase BFO, which showed an excellent absorption of light in the visible range from 200 to 800 nm, revealing its capabilities for photocatalysis and other multiferroic semiconductor applications. As a result, we investigated how well it degraded methylene blue when exposed to sunlight. This investigation revealed that pure

phase BFO could be degrading methylene blue by 33%. It is worth mentioning that the pure phase BFO produced by the microwave-assisted solvothermal method has a superior photocatalytic performance (33% degradation in MB) to BFO produced by the solvothermal method (10% degradation in MB).

7.1.3. Photocatalytic activity of BFO+Fe₂O₃ heterostructures

In this chapter, we developed a BFO-based heterostructure to improve pure phase BFO's photocatalytic activity, which currently displays a 33% efficiency and is extremely low compared to other semiconductors. As a result, we used different molar ratios of the most efficient visible active semiconductor Fe₂O₃ to build the BFO-based heterostructure. We used parent BFO and hollow Fe₂O₃ microspheres made using microwave-assisted solvothermal and sol-gel techniques, respectively. Three different series of BFO+Fe₂O₃ heterostructures denoted as BFOF10, BFOF20, and BFOF30 were produced by adding Fe₂O₃ at different molar ratios (10, 20 and 30%) to the BFO. The XRD results for these heterostructures showed that BFO+Fe₂O₃ heterostructures were produced without any secondary phases. FE-SEM images and EDAX spectra of these heterostructures demonstrated the formation of BFO+Fe₂O₃ heterostructures with a coupling between the two BFO and Fe₂O₃ phases. Unlike the BFOF10 and BFOF20 heterostructures, BFOF30 exhibits excellent coupling between the BFO and Fe₂O₃ phases. UV-Vis absorption spectroscopy studies show that these heterostructures exhibit more visible light absorption than pure phase BFO. It has also been noted that the visible light absorption of these heterostructures increases as the amount of Fe₂O₃ increases, demonstrating that they are more capable of light absorption than the pure phase BFO after adding Fe₂O₃. According to the results of the photocatalytic performance test, the heterostructures BFOF10 (72%), BFOF20 (86), and BFOF30 (94) displayed excellent degradation in the MB solution under direct sunlight in just 70 minutes. The stability and magnetic recovery tests showed that the heterostructure BFOF30 (94%) was more stable for four cycles, had better magnetic recovery properties, and degraded the MB faster than the other two heterostructures. This was because the interface between BFO and Fe₂O₃ had a lower rate of electron-hole pair recombination. This comprehensive analysis showed that the heterostructure BFOF30 is the most effective photocatalyst for decomposing MB dye in a relatively short time (70 minutes) when exposed to sunlight.

7.1.4. The photocatalytic performance of BFO+BTO heterostructures

In this chapter, we developed one more BFO-based heterostructure to improve pure phase BFO's photocatalytic activity, which currently displays a 33% efficiency and is extremely low compared to other semiconductors. As a result, we used different molar ratios of the most efficient visible active semiconductor BTO (black TiO2) to build the BFO-based heterostructure. We used parent BFO powder, and BTO nanoparticles made using microwave-assisted solvothermal and e-beam techniques. Three different series of BFO+BTO heterostructures denoted as BFOT10, BFOT20, and BFOT30 were produced by adding BTO at different molar ratios (10, 20 and 30%) to the BFO. The XRD results for these heterostructures showed that BFO+BTO heterostructures were produced without any secondary phases. FE-SEM pictures and EDAX spectra of these heterostructures demonstrated the generation of uniformly distributed BFO+BTO grains with many grain boundaries connecting the BFO and BTO phases. Unlike the BFOT10 and BFOT20 heterostructures, the BFO and BTO phases are strongly coupled in the BFOT30 heterostructure. UV-Vis absorption spectroscopy studies have revealed that these heterostructures display outstanding visible light absorption. In addition, it has been observed that the visible light absorption of these heterostructures increases with the amount of BTO, indicating that they are more capable of light absorption than the pure phase BFO following the addition of BTO. In only 70 minutes, Methylene Blue was destroyed by the photocatalytic performance of BFOT10, BFOT20, and BFOT30 in sunlight. BFOT10 (65%), BFOT20 (86%), and BFOT30 (97%) exhibit improved photocatalytic performance than pure phase BFO (33%). Since BFO and BTO exhibit strong coupling between the electron-hole pairs, the heterostructure BFOT30 (97%) displayed a higher degradation efficiency than the other two heterostructures. The magnetic properties of these heterostructures revealed that BFOT10 displayed weak ferromagnetic behaviour, while BFOT20 and BFOT30 showed diamagnetic behaviour. Due to these factors, BFOT30 had poor magnetic recovery of photocatalysts under magnetic field conditions. The stability, magnetic recovery, and photocatalysis tests showed that the heterostructure BFOT30 (94%) was stable for only two cycles, had poor magnetic recovery properties and degraded the MB faster than the other two heterostructures (BFOT10, BFOT20).

7.2. Future Work Plan

In the present work, a multiferroic BFO powder is synthesized through a microwaveassisted solvothermal process in a reaction time of 3 min, resulting in increased magnetic and dielectric properties. The ferroelectric and photocatalytic characteristics, however, are extremely poor. To enhance the photocatalytic properties of pure phase BFO, we synthesized two different BFO-based heterostructures by adding black TiO₂ and Fe₂O₃. Heterostructures of BFO+Fe₂O₃ and BFO+BTO have demonstrated higher photocatalytic efficiency than pure phase BFO. However, the pure BFO's ferroelectric characteristics and the time it takes for deterioration to complete are disadvantages. This has led to the proposal in the upcoming proceedings to synthesize transition and rare earth metal ion doping into BFO materials as well as fabricating thin films of BFO using the same synthesis method, i.e., microwave-assisted-solvothermal, as a means of improving the ferroelectric and photocatalytic efficiency of single phase BFOs; in addition, different characterization techniques will be used to assess the efficiency of single phase BFO. These characterisation methods include thermogravimetric (TG-DTA), photoluminescence (PL), Mossbauer spectroscopy, DC and AC conductivity studies, etc. Additionally, their photovoltaic properties will be investigated since they have been described as potential photocatalysts.

According to the findings, it has also been planned to synthesize BFO-based nanocomposites utilising 2D materials like MXene and reduced graphene oxides to investigate their electrochemical capabilities. As part of this project, it is not only photocatalysis being considered but also its application to photovoltaics and batteries. In conclusion, the main areas of research for the future will be the synthesis of doped and codoped BFO, BFO thin films, and BFO-based nanocomposite materials with a focus on solar and battery applications.

SUPPLEMENTARY DATA

A). XRD data of BFO synthesized by a commercial microwave oven.

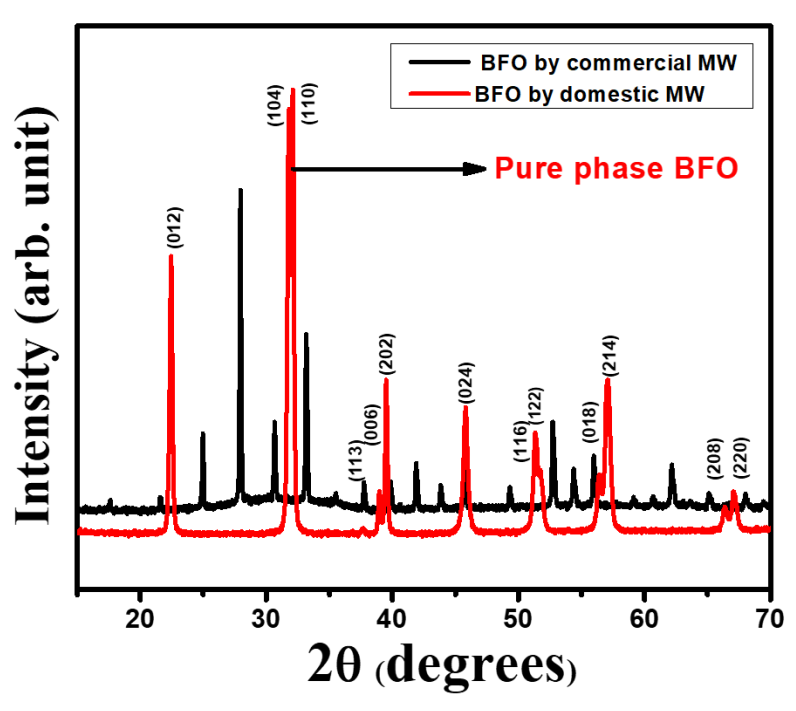


Figure S1. XRD pattern of BFO synthesized by commercial (650 W, 15min) and domestic microwave oven (800 W, 3min).



Figure S2. Commercial microwave oven

B. XRD pattern of BFO synthesized by commercial and domestic microwave oven at different MW duration at different MW power

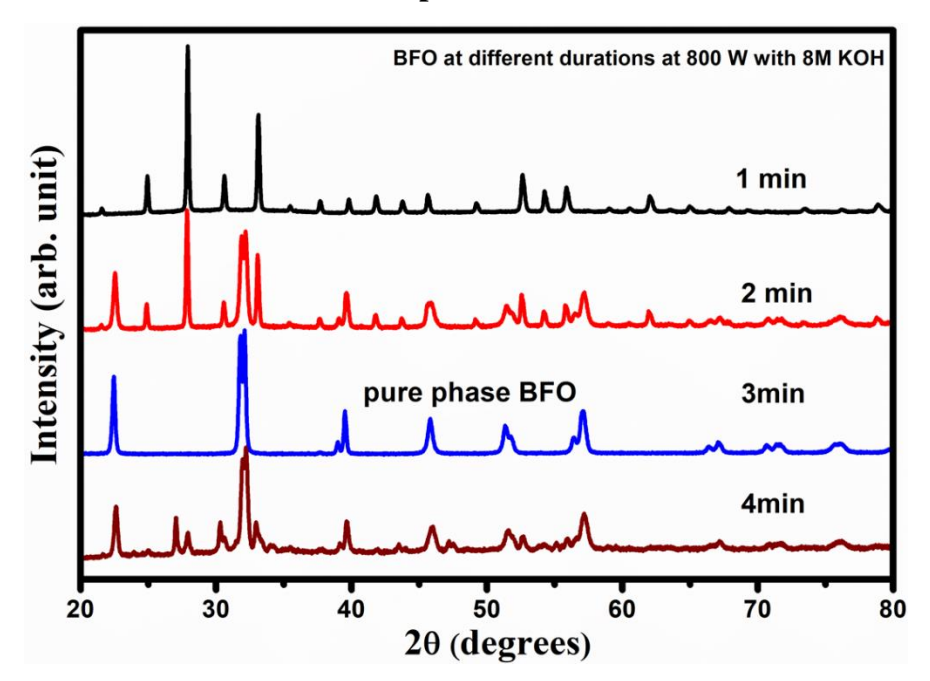


Figure S3. XRD pattern of BFO synthesized by domestic microwave oven at 360 W at different MW duration.

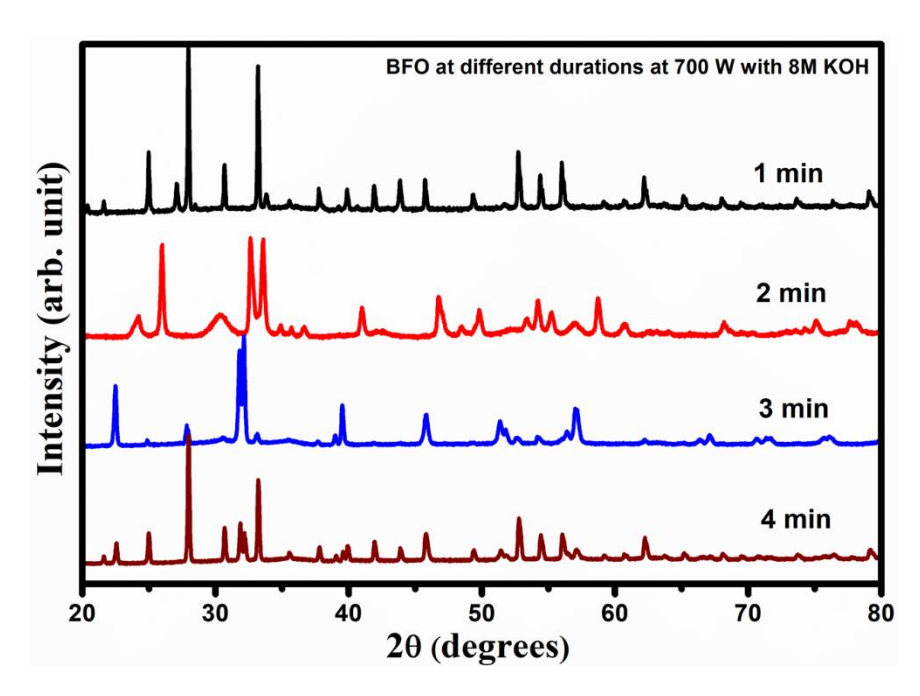


Figure S4. XRD pattern of BFO synthesized by domestic microwave oven at 700 W at different MW duration.

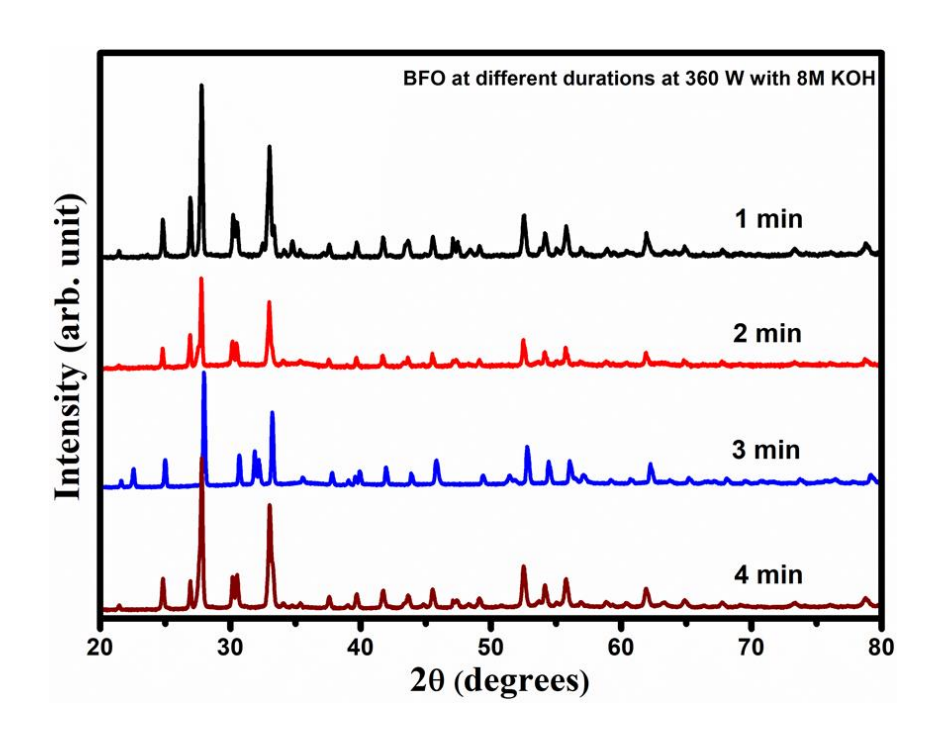


Figure S5. XRD pattern of BFO synthesized by domestic microwave oven at 800 W at different MW duration.

Synthesis and characterization of multiferroics BiFeO3(BFO) and BFO based heterostructures for photocatalysis application

by Pravallika Banoth

Submission date: 24-Aug-2022 12:01PM (UTC+0530)

Submission ID: 1886295641

File name: THESIS 18PHPH17.pdf (5.84M)

Word count: 32985 Character count: 180541

Synthesis and characterization of multiferroics BiFeO3(BFO) and BFO based heterostructures for photocatalysis application

ORIGINALITY REPORT

20%

10%

19%

1%

SIMILARITY INDEX

INTERNET SOURCES

PUBLICATIONS

STUDENT PAPERS

PRIMARY SOURCES

Pravallika Banoth, Arya Sohan, Chinna Kandula, Pratap Kollu. "Structural, dielectric, magnetic, and ferroelectric properties of bismuth ferrite (BiFeO3) synthesized by solvothermal process using hexamethylenetetramine (HMTA) as precipitating agent", Ceramics International, 2022

Publication

www.ncbi.nlm.nih.gov

Internet Source

14 lip 24/08/22

Dr. PRATAP KOLLU
Assistant Professor
CASEST, School of Physical Management of Hyderabad, Hyderabad, 100 046, India.

Dr. PRATAP KOLLU Assistant Professor

CASEST, School of Physics, University of Hyderabad, Hyderabad-500 046, India.

Pravallika Banoth, Arya Sohan, Chinna
Kandula, Ravi Kumar Kanaka, Pratap Kollu.

"Microwave-Assisted Solvothermal Route for
One-Step Synthesis of Pure Phase Bismuth
Ferrite Microflowers with Improved Magnetic Sistant Professor
ASEST, School of Physics, and Dielectric Properties", ACS Omega, 2022 Hyderabad-500 046, India.

Publication

4

A.J.C. Buurma, G.R. Blake, T.T.M. Palstra, U. Adem. "Multiferroic Materials: Physics and

<1%



5	Submitted to Alexandru Ioan Cuza University of Iasi Student Paper	<1%
6	Submitted to VIT University Student Paper	<1%
7	www.science.gov Internet Source	<1%
8	onlinelibrary.wiley.com Internet Source	<1%
9	Ying-Jie Zhu, Feng Chen. "Microwave-Assisted Preparation of Inorganic Nanostructures in Liquid Phase", Chemical Reviews, 2014	<1%
10	Valladares, L. de los Santos, L. León Félix, S.M. Espinoza Suarez, A.G. Bustamante Dominguez, T. Mitrelias, S. Holmes, N.O. Moreno, J. Albino Aguiar, and C.H.W. Barnes. "Preparation and crystallization of hollow α-Fe2O3 microspheres following the gas-bubble template method", Materials Chemistry and Physics, 2016. Publication	<1%

Nanostructure Science and Technology, 2016.

Publication

<1%

Student Paper

- 13
- D. Ravi Kumar, Syed Ismail Ahmad, Ch. Abraham Lincoln, D. Ravinder. "Structural, optical, room-temperature and low-temperature magnetic properties of Mg–Zn nanoferrite ceramics", Journal of Asian Ceramic Societies, 2019

<1%

Publication

14

answersdrive.com

Internet Source

<1%

15

Asif Hussain, Jianhua Hou, Muhammad Tahir, S.S Ali, Zia Ur Rehman, Muhammad Bilal, Tingting Zhang, Qian Dou, Xiaozhi Wang. "Recent advances in BiOX-based photocatalysts to enhanced efficiency for energy and environment applications", Catalysis Reviews, 2022

<1%

Publication

16

Zhi Wang, Junyu Zhu, Wenfei Xu, Jin Sui, Hui Peng, Xiaodong Tang. "Microwave hydrothermal synthesis of perovskite BiFeO3 nanoparticles: An insight into the phase purity during the microwave heating process", Materials Chemistry and Physics, 2012

<1%

Publication

17	Raimondo Germani, Marzia Bini, Simona Fantacci, Federica Simonetti, Matteo Tiecco, Eleonora Vaioli, Tiziana Del Giacco. "Influence of surfactants in improving degradation of polluting dyes photocatalyzed by TiO2 in aqueous dispersion", Journal of Photochemistry and Photobiology A: Chemistry, 2021 Publication	<1%
18	www.researchgate.net Internet Source	<1%
19	etheses.whiterose.ac.uk Internet Source	<1%
20	Li Yin, Wenbo Mi. " Progress in BiFeO -based heterostructures: materials, properties and applications ", Nanoscale, 2020 Publication	<1%
21	Jennifer B. Coulter, Dunbar P. Birnie. "Assessing Tauc Plot Slope Quantification: ZnO Thin Films as a Model System", physica status solidi (b), 2018 Publication	<1%
22	allie.dbcls.jp Internet Source	<1%
23	mdpi-res.com Internet Source	<1%

24	www.mdpi.com Internet Source	<1%
25	www.tandfonline.com Internet Source	<1%
26	opac.elte.hu Internet Source	<1%
27	Jonathan Gustavo Acosta Ramón. "Geometrically frustrated magnetism in the pyrochlore Er>sub<2>/subsub<2- x>/subsub/subsub<7>/sub< and in the disordered fluorites R>sub<2>/subsub<2>/subsub<7>/subsub<7>/sub< (>i/i<= Dy, Ho, Tb)", Universidade de Sao Paulo, Agencia USP de Gestao da Informacao Academica (AGUIA), 2020 Publication	<1%
28	S. SHANTHY. "MULTIFERROIC BiFeO3 FILMS: CANDIDATE FOR ROOM TEMPERATURE MICRO BIOSENSOR", Integrated Ferroelectrics, 2008 Publication	<1%
29	Xiangwen Liu, Huaqiang Cao, Jiefu Yin. "Generation and photocatalytic activities of Bi@Bi2O3 microspheres", Nano Research, 2011 Publication	<1%
	kb.psu.ac.th	

Elemental Sulfur for Dye Degradation in

Alkaline Solution", Photochemistry and Photobiology, 2020

Publication

coek.info
Internet Source

<1 %

www.arkat-usa.org
Internet Source

<1 %

Exclude quotes On

Exclude bibliography On

Exclude matches

< 14 words



ಪ್ರಾದರಾಬಾದ್ ವಿಸ್ಪವಿದ್ಯಾಲಯಂ

UNIVERSITY OF HYDERABAD

(A Central University Established in 1974 by an Act of Parliament)

సెల్ / Cell : +91 7981468978 ఫోన్ / Phone : +91-40 - 23134327

పోష్టు : కేంట్రీయ విశ్వవిద్యాలయ ప్రాంతం P.O. : Central University Campus హైదరాబాద్ - 500 046., తెలంగాణ, ఇండియు. Hyderabad - 500046., Telangana (India).

Email: pksp@uohyd.ernet.in, pratapk@uohyd.ac.in

Dr. PRATAP KOLLU Asst. Professor School of Physics

TO WHOM IT MAY CONCERN

This is to certify that the thesis "Synthesis and characterization of multiferroic BiFeO₃ (BFO) and BFO-based heterostructures for photocatalysis application" submitted by Ms. Banoth Pravallika (Reg. No.: 18PHPH17), has been screened by the Turnitin software at the Indira Gandhi memorial library (IGML), University of Hyderabad. This software shows 20% similarity index out of which 18% came from the candidate's own research article (where she is the first author) directly related to this thesis.

From the detailed similarity index report, it is obvious that the remaining 2% of the similarity index, is due to the resemblance caused by the frequent use of the well-known standard terms. Standard terminology such as multiferroics, ferroelectricity, ferromagnetism, antiferromagnetic, Field emission scanning electron microscopy, UV-Visible spectroscopy, microstructure, properties, magnetic moment, dielectric constant, etc. to name a few. The use of such term is rampant in the literature, and hence it is not surprising that the similarity index is artificially inflated. It should be noted that the use of such standard terms cannot be avoided.

Thanks and regards

Dr Pratap Kollu

Thesis Supervisor

24/08/2022

